

1 **Anatomy of the magmatic plumbing system of Los Humeros Caldera (Mexico): implications for**
2 **geothermal systems**

3

4 Federico Lucci¹ *, Gerardo Carrasco-Núñez², Federico Rossetti¹, Thomas Theye³, John C. White⁴, Stefano
5 Urbani¹, Hossein Azizi⁵, Yoshihiro Asahara⁶, and Guido Giordano^{1,7}

6

7 ¹Dipartimento di Scienze, Sez. Scienze Geologiche, Università Roma Tre, Largo S. L. Murialdo 1, 00146
8 Roma, Italy

9 ²Centro de Geociencias, Universidad Nacional Autónoma de México, Campus UNAM Juriquilla, 76100,
10 Queretaro, Mexico

11 ³Institut für Anorganische Chemie, Universität Stuttgart, Stuttgart, Germany

12 ⁴Department of Geosciences, Eastern Kentucky University, Richmond, KY 40475, USA

13 ⁵Mining Department, Faculty of Engineering, University of Kurdistan, Sanandaj, Iran

14 ⁶Department of Earth and Environmental Sciences, Graduate School of Environmental Studies, Nagoya
15 University, Nagoya 464-8601, Japan

16 ⁷CNR - IDPA, Via Luigi Mangiagalli 34, 20133 Milano

17 *Corresponding Author e-mail: federico.lucci@uniroma3.it

18

19 **ABSTRACT**

20 Understanding the anatomy of magma plumbing systems of active volcanoes is essential not only for
21 unraveling magma dynamics and eruptive behaviors, but also to define the geometry, depth and
22 temperature of the heat sources for geothermal exploration. The Pleistocene-Holocene Los Humeros
23 volcanic complex is part of the Eastern Trans-Mexican Volcanic Belt (Central Mexico) and it **constitutes** one
24 of the most important exploited geothermal fields in Mexico with *ca.* 90 MW of produced electricity. **With**
25 **the aim to decipher the anatomy (geometry and structure) of the magmatic plumbing system feeding the**
26 **geothermal field at Los Humeros, we carried out a** field-based petrological and thermobarometric study of
27 **the exposed Holocene lavas. Textural analysis,** whole rock major element data and mineral chemistry **are**
28 integrated with a suite of mineral-liquid thermobarometric models. **Our** results support a scenario
29 characterized by a heterogeneous multilayered system, comprising a deep (**depth of ca. 30 km**) basaltic
30 reservoir feeding progressively shallower and smaller discrete **magma stagnation layers and batches, up**
31 **to shallow-crust conditions (depth of ca. 3km).** Evolution of melts in the feeding system is mainly controlled by
32 differentiation processes through fractional crystallization (plagioclase + clinopyroxene + olivine + spinel).
33 We demonstrate the inadequacy of **the existing** conceptual models, **where a single voluminous, melt-**
34 **controlled, magma chamber (or “Standard Model”) at shallow depths was proposed for the magmatic**
35 **plumbing system at Los Humeros.** We instead propose a magmatic plumbing system made of multiple,
36 more or less interconnected magma transport and storage layers within the crust, feeding small
37 (ephemeral) magma chambers at shallow-crustal conditions. This revised scenario provides a new
38 configuration of the heat source feeding the geothermal **reservoir at Los Humeros, and it should** be taken
39 into account to drive future exploration and exploitation strategies.

40

41 **Keywords**

42 Magmatic plumbing system, Thermobarometry, Heat source, Geothermal exploration, Trans Mexican
43 Volcanic Belt, Los Humeros, Mexico

44

45 1.INTRODUCTION

46 Recent views on the structure of volcanic plumbing systems have moved from the “Standard Model” (*sensu*
47 Gualda and Ghiorso, 2013) of a single, bowl-shaped magma chamber **where** all petrological processes of
48 differentiation and assimilation occur (e.g. Hildreth, 1979, 1981; Hildreth and Wilson, 2007) to more
49 complex arrays of stratified and variably **interconnected transient** magma accumulation zones, set in largely
50 crystallized and vertically extensive mush zones (e.g., Bachman and Bergantz, 2004; 2008; Cashman and
51 Giordano, 2014; Cashman et al., 2017). Furthermore, the time required for the assembly of large magma
52 chambers is now believed to be very short, within the span of decades to a few thousands of years for tens
53 to hundreds of km³ of eruptible magma (e.g. Glazner, 2004; Charlier et al., 2007), which are then rapidly
54 evacuated during eruptions of caldera-forming ignimbrites (e.g., Begué et al., 2014; Rivera et al., 2014;
55 Wotzlaw et al, 2014; Matthews et al., 2015; Carrasco-Núñez et al., 2018). Key **factor** in determining the
56 internal architecture of the magmatic systems is the magma **intrusion rate**. **It controls** whether successive
57 pulses of magma will coalesce to form progressively larger chambers, as well as the formation of ductile
58 shells surrounding the magma chamber that prevent country rock failure, favoring the inflation of the
59 reservoir (Jellinek and de Paolo, 1981; Annen, 2009). Numerical simulations suggest that caldera systems
60 smaller than 100 km² are fed by plumbing systems encapsulated by country rock that remains sufficiently
61 brittle, while larger systems are more ductile, which favors an increase in size (Gregg et al., 2012).

62 The implications of such innovative conceptual models on the modeling of the heat source in magmatic-
63 bearing geothermal systems are significant. Nonetheless, common numerical **modeling** of conductive-
64 convective heat transfer in caldera-related geothermal systems have commonly envisaged the classic
65 magma chamber as a single body, chemically stratified, entirely at magmatic temperatures, whose
66 dimensions and depths have been usually constrained by volcanological and petrological data (e.g. Verma,
67 1985; Wohletz et al., 1999). More complex modeling requires the “unpacking” of the stratigraphy of a
68 volcano by the identification of the various “magma chambers” or magma storage layers that fed the
69 different eruptions in space and time (e.g., Solano et al., 2014; Di Renzo et al., 2016; Cashman et al., 2017;
70 Jackson et al., 2018).

71 A key to decipher where magmas are stored and, therefore, the anatomy of a magmatic plumbing system,
72 is the understanding of pre-eruptive processes such as mineral crystallization and the migration and
73 stagnation of melts prior to their eruption (Feng and Zhu, 2018, Putirka, 2008; Keiding and Sigmarsson,
74 2012; Scott et al., 2012, Barker et al., 2015; Jeffery et al., 2013; Cashman and Giordano, 2014; Pamukcu et
75 al., 2015; Lucci et al., 2018). Early segregated minerals reflect the magmatic environment (i.e., pressure-
76 temperature, magma/fluid composition, oxidation state) and thus their growth, texture and chemistry
77 provide an important archive of information (Ginibre et al., 2002; Feng and Zhu, 2018; Ginibre et al., 2007;
78 Streck, 2008; Giuffrida and Viccaro, 2017; Viccaro et al., 2016; Putirka et al., 2008; Lucci et al., 2018).
79 Accordingly, petrographic observations and mineral chemistry of primary minerals, integrated with

80 opportunely selected thermobarometry models (e.g., Putirka, 2008; Masotta et al., 2013) could lead to the
81 comprehension and reconstruction of the magmatic storage/feeding systems of the erupted products (Feng
82 and Zhu, 2018; Giuffrida and Viccaro, 2017; Elardo and Shearer, 2014; Petrone et al., 2016; Zheng et al.,
83 2016; Eskandari et al., 2018; Shane and Coote, 2018; Scott et al., 2012; Stroncik et al., 2009; Barker et al.,
84 2015; Jeffery et al., 2013; Keiding and Sigmarsson, 2012).

85 In this paper we present a geothermobarometric study of the post-caldera Pleistocene-Holocene products
86 of the Los Humeros volcanic complex (LHVC), located at the eastern **termination** of the Neogene-
87 Quaternary Trans-Mexican Volcanic Belt (TMVB) (Fig. 1), with the goal of **reconstructing** the present-day
88 geometry and structure of the magmatic plumbing system. These data are used to develop a conceptual
89 model for the magmatic heat source of the active and currently exploited geothermal system. **Since now,**
90 **the** magmatic heat source for LHVC has been constrained by the geometry of the caldera, the volume and
91 mass balance calculations of the associated ignimbrites (Ferriz and Mahood, 1984, 1987; Verma, 1984,
92 1985a, 1985b, Verma et al., 1990; Verma and Andaverde, 1995; Verma et al., 2011; Verma et al. 2013), all
93 related to a single magma body. We propose a new and more realistic vision of the magmatic plumbing
94 **system**, made of multiple interconnected magma stagnation layers within the crust. These new findings
95 must be considered into the new developing conceptual geothermal models to improve strategies for
96 exploration and exploitation of the geothermal system within the LHVC. The results and approach
97 presented in this work have also a general value and could represent an efficient strategy to explore and
98 **reconstruct the** pre-eruptive geometry and the anatomy of active magmatic feeding systems.

99

100 **2.GEOLOGICAL SETTING**

101 **2.1 Regional Geology**

102 LHVC is the largest and easternmost Quaternary caldera (Fig. 1) of the 1200 km-long **and active** Trans-
103 Mexican Volcanic Belt (TMVB), generated since *ca.* 20 Ma by the subduction of **the** Cocos plate beneath
104 central Mexico (e.g. Demant, 1978, Ferrari et al. 1999, 2012; Gomez-Tuena et al., 2003, 2007a, 2007b,
105 2018; Norini et al., 2015). **The eastern sector of the TMVB, where LHVC is located, is** characterized by
106 monogenetic volcanism, scattered basaltic cinder and scoria cones, maar volcanoes of basaltic and rhyolitic
107 composition, large rhyolitic domes and major stratovolcanoes such as Pico de Orizaba (or Citlaltépetl) and
108 Cofre de Perote (e.g., Yáñez and García, 1982; Negendank et al., 1987; Carrasco-Núñez et al., 2010, 2012a).
109 The Paleozoic to Mesozoic crystalline basement of eastern TMVB is exposed along the Teziutlán Massif
110 (Viniegra, 1965; **Yáñez and García, 1982**; Ferriz and Mahood, 1984). **The** crystalline basement is partially
111 covered by a thick, highly deformed Mesozoic sedimentary succession, **part of the Sierra Madre Oriental**
112 **fold and thrust, structured during the** Late Cretaceous-Paleocene Laramide orogeny (e.g. Campos-Enriquez
113 and Garduño-Monroy, 1987; Suter, 1987; Fitz-Díaz et al., 2018). Oligocene to Miocene granodiorite and
114 syenite intrusions (**whole-rock K-Ar ages spanning 15-31 Ma, Yáñez and García, 1982**) are randomly

115 exposed in the region. Miocene volcanism consists of andesites of the Cerro Grande volcanic complex
116 (Gómez-Tuena and Carrasco-Núñez, 2000), with an age of ca. 9-11 Ma (K-Ar method, whole-rock, Carrasco-
117 Núñez et al. 1997), and the Cuyoaco Andesite dated at ca. 11 Ma (K-Ar method, whole-rock, Yáñez and
118 García, 1982) to the west of LHVC, which can be correlated with the Alseseca Andesite (Yáñez and García,
119 1982) exposed to the north. Pliocene andesitic volcanism (Ferriz and Mahood, 1984; Yáñez and García,
120 1982) is represented by the Teziutlán Andesite, which, recently dated by the $^{40}\text{Ar}/^{39}\text{Ar}$ method at 2.61 ± 0.43
121 - 1.46 ± 0.31 Ma (Carrasco-Núñez et al., 2017a), correlates with most of the thick andesitic successions of the
122 subsurface geology of LHVC.

123

124 2.2 Los Humeros Volcanic Complex

125 The volcanic evolution of the LHVC consists of three main stages (Carrasco-Núñez et al., 2018): (i) pre-
126 caldera stage; (ii) caldera stage; and (iii) post-caldera stage. The pre-caldera stage is represented by
127 relatively abundant rhyolitic domes, which erupted mainly on the western side of Los Humeros caldera,
128 with an isolated spot to the south, and in some buried lavas identified in the geothermal well-logs
129 (Carrasco-Núñez et al., 2017a). This volcanism has been recently dated by coupled U-Th and $^{40}\text{Ar}/^{39}\text{Ar}$
130 methods (Carrasco-Núñez et al., 2018), providing ages spanning from 693.0 ± 1.9 ka ($^{40}\text{Ar}/^{39}\text{Ar}$, plagioclase)
131 to 270 ± 17 ka (U-Th, zircon), which overlap with the age range obtained from other domes of the western
132 sector outside the caldera, where K-Ar ages (sanidine) of 360 ± 100 ka and 220 ± 40 ka were obtained (Ferriz
133 and Mahood, 1984). The caldera stage consists of two major caldera-forming events, separated by a large
134 Plinian eruptive episode. The first and largest caldera-forming eruption produced Los Humeros caldera (18
135 km in diameter) during the emplacement of the Xaltipan ignimbrite, a rhyolitic, welded to non-welded, ash-
136 rich deposit, radially distributed around the caldera. The dense rock equivalent (DRE) volume of this event
137 was estimated at 115 km^3 by Ferriz and Mahood (1984). The age of the Xaltipan ignimbrite was established
138 by whole-rock K-Ar dating at 460 ± 20 ka (plagioclase) and 460 ± 130 ka (biotite) (Ferriz and Mahood, 1984),
139 however Carrasco-Núñez et al. (2018) based on coupled zircon U-Th dating and $^{40}\text{Ar}/^{39}\text{Ar}$ method
140 (plagioclase) geochronology provided a younger age of 164.0 ± 4.2 ka.

141 Following this catastrophic event an eruptive pause occurred, resuming with a sequence of intermittent
142 Plinian episodes at 70 ± 23 ka ($^{40}\text{Ar}/^{39}\text{Ar}$ method on plagioclase; Carrasco-Núñez et al., 2018), separated by
143 short gaps marked by thin paleosoils. The deposits consist of thick (1-6 m) coarse pumice-rich, well-sorted,
144 massive and diffuse-stratified layers, rhyodacitic in composition, which are grouped as the Faby Tuff (Ferriz
145 and Mahood 1984; Willcox, 2011). The second caldera-forming episode produced the 9-10 km large Los
146 Potreros caldera, which is associated with the emplacement of the compositionally zoned andesitic-
147 rhyodacitic-rhyolitic Zaragoza ignimbrite (Carrasco-Núñez et al., 2012b). This is an intraplinian pyroclastic
148 flow deposit, with an estimated volume of ca. 15 km^3 DRE (Carrasco-Núñez and Branney, 2005). Previous
149 ages of this unit were reported at 100 ka (K-Ar dating, plagioclase; Ferriz and Mahood, 1984) and at 140 ± 24

150 ka ($^{40}\text{Ar}/^{39}\text{Ar}$ method, plagioclase; Willcox, 2011). However, a new younger $^{40}\text{Ar}/^{39}\text{Ar}$ plagioclase age of
151 69 ± 16 ka for the Zaragoza ignimbrite was recently obtained, supported by the field evidence that the
152 Zaragoza ignimbrite overlies a rhyodacitic lava flow dated at 74.2 ± 4.5 ka (zircon U-Th dating) (Carrasco-
153 Núñez et al., 2018).

154 According to Carrasco-Núñez et al. (2018) during the post-caldera stage, two different eruptive phases
155 occurred (Fig. 1). The first one was a late Pleistocene resurgent phase characterized by the emplacement of
156 felsic domes in the central area at about 44.8 ± 1.7 ka (zircon U-Th ages; Carrasco-Núñez et al., 2018), which
157 is slightly younger than the previously reported whole-rock K-Ar date (60 ± 20 ka, glass; Ferriz and Mahood,
158 1984). Outside of the caldera, to the north, a rhyolitic dome erupted at 50.7 ± 4.4 ka ($^{40}\text{Ar}/^{39}\text{Ar}$, plagioclase;
159 Carrasco-Núñez et al., 2018). This was followed by a sequence of explosive eruptions, producing dacitic
160 pumice fall units (Xoxoctic Tuff, 0.6 km^3) and interbedded breccia and pyroclastic flows deposits of the
161 Llano Tuff (Ferriz and Mahood 1984; Willcox, 2011), with a maximum age of 28.3 ± 1.1 ka (C-14 method;
162 Rojas-Ortega, 2016). The second eruptive phase of the post-caldera stage is a Holocene ring-fracture and
163 bimodal activity that occurred towards the south, north and central part of Los Humeros caldera (Carrasco-
164 Núñez et al., 2017). It is characterized by alternating episodes of effusive and explosive volcanism with a
165 wide range of compositions. The volcanic products span from basaltic-andesitic, basaltic trachytic,
166 trachyandesitic lava flows and dacitic, trachydacitic, andesitic and basaltic pumice and scoria fall deposits
167 erupted by tens of monogenetic eruptive centers located in the LHVC (Ferriz and Mahood, 1984; Dávila-
168 Harris and Carrasco-Núñez, 2014; Norini et al., 2015; Carrasco-Núñez et al., 2017b). Most of the effusive
169 activity was initially referred to 40-20 ka (K-Ar method, whole-rock; Ferriz and Mahood, 1984), but recent
170 dating reveals that most of this activity is Holocene (Carrasco et al., 2017b). Trachyandesitic and andesitic
171 basalt lavas erupted to the north of the LHVC at about 8.9 ± 0.03 ka (C-14 method; Carrasco-Núñez et al,
172 2017b). A rhythmic alternation of contemporaneous bimodal explosive activity produced trachyandesitic
173 and basaltic fall layers grouped as the Cuicuiltic Member erupted at 7.3 ± 0.1 ka (C-14 method; Dávila-Harris
174 and Carrasco-Núñez, 2014). This activity migrated towards the southern caldera rim to form a well-defined
175 lava field. This ring-fracture episode erupted trachyandesite and olivine-bearing basaltic lava flows, at
176 3.9 ± 0.13 ka (C-14 method; Carrasco-Núñez et al, 2017b). The most recent activity erupted trachytic lava
177 flows near the SW caldera rim, at 2.8 ± 0.03 ka (C-14 method; Carrasco-Núñez et al, 2017b).

178

179 2.3 Los Humeros geothermal system

180 The LHVC hosts one of the three most important geothermal fields in Mexico, with an installed 93 MW of
181 electric power produced from 20 geothermal wells (Romo-Jones et al., 2017). The existing conceptual
182 models for the Los Humeros geothermal field (LHGF) (see Norini et al., 2015 for a review) stem from the
183 hypothesis of a unique, large and voluminous cooling magma chamber of $1000\text{-}1500\text{ km}^3$ in volume,
184 residing at a depth of 5 to 10 km from the surface (Verma, 1984, 1985a, 1985b, 2000; Verma et al., 1990;

185 Verma and Andaverde, 1995; Verma et al., 2011; Verma et al. 2013; Carrasco-Núñez et al. 2018) and
186 providing the heat source for the geothermal system (Martínez et al., 1983; Verma, 1983, 2000; Campos-
187 Enríquez and Garduño-Monroy, 1987). However, the LHGF is characterized by a low number of productive
188 geothermal wells (ca. 20 out of 50; Norini et al., 2015; Carrasco-Núñez et al., 2017a). The confined
189 distribution of these productive wells along the NNW-SSE trending “Maxtaloya-Los Humeros-Loma Blanca”
190 fault system (MHBfs in Fig. 1) cutting across Los Potreros caldera (e.g., Norini et al., 2015; Carrasco-Núñez
191 et al., 2017a) also corresponds to the almost unique, narrow and sharp surface thermal anomaly
192 recognized within the caldera (Norini et al., 2015). These observations raise doubts on the existence of a
193 voluminous superficial heat source feeding the LHGF. A revised assessment of the structure of the
194 magmatic plumbing system beneath LHVC is therefore required for a better understanding and exploitation
195 of the geothermal resource.

196

197 3. MATERIALS AND METHODS

198 In this work we focus on petrographic investigations including a textural and chemical (mineral chemistry
199 and major-elements bulk-rock) characterization, of the Los Humeros post-caldera stage (LHPCS) Holocene
200 lavas (Carrasco-Núñez et al. 2017b). These data are used to define the thermobarometric conditions of the
201 magma plumbing system and to test the eventual co-genetic nature of the LHPC melts. Following the
202 recently published geological map (Carrasco-Núñez et al. 2017b) and geochronology (Carrasco-Núñez et al.
203 2018) of the LHVC, more than fifty samples of the LHPCS lavas were collected in the field with the goal to
204 describe all the compositional variability of erupted products during the LHPCS activity (Figs. 1, 2a-d). In the
205 following description of the volcanic units, abbreviations follow Carrasco et al. (2017b). The most preserved
206 and representative samples of each LHPCS volcanic unit were then selected (see Fig. 1 for sample location)
207 for bulk and mineral chemistry investigations. With respect to the intra-caldera domain (Fig. 2a), we
208 selected lava samples belonging to: (i) LH27-1 from the mafic lavas inside the Xalapasco Crater (Qb1), (ii)
209 LH27-2 from the Maxtaloya trachyandesites (Qta4) constituting the rim-walls of Xalapasco craters, (iii) LH4
210 from San Antonio-Las Chapas lavas (Qta3) outcropping in the Los Humeros town, (iv) LH5-2 from mafic
211 lavas (Qb1) outcropping west to Los Humeros town, (v) LH5-1 from Chicomiapa-Los Parajes felsic lavas
212 (Qt2) outcropping in the north-western part of Los Potreros caldera, (vi) LH6-1 from El Pajaro unit (Qt1)
213 outcropping in the north-western part of Los Potreros caldera. In addition to these units, we also selected
214 three more samples (LH13, LH26-1 and LH26-2) from lavas and domes of intermediate compositions,
215 outcropping (Fig. 2b-c) in the center of Los Potreros caldera between Xalapasco crater and Los Humeros
216 town, and not reported on the published geological map.

217 Concerning the extra-caldera products (Fig. 2d), we selected one sample for each of the four major lava
218 flows: (i) LH15 from El Limón lava flow (Qab), (ii) LH21-2 from Sarabia lava flow (Qta1), (iii) LH17 from
219 Tepeyahualco lava flow (Qtab), and (iv) LH18 from Texcal lava flow (Qb1).

220 The samples were investigated first by optical microscopy and then through back scattered electron (BSE)
221 imaging for the definition of magmatic fabrics, textures and constituent mineral assemblages. Mineral
222 chemistry was then defined through electron microprobe analyses (EMPA). Whole rock (major elements)
223 composition of selected samples was obtained through ion coupled plasma – optical emission (ICP-OE) and
224 X-ray fluorescence (XRF) analyses. Analytical protocols are described in the Appendix A. In the following,
225 mineral abbreviations follow Whitney and Evans (2010), whereas types of mineral zoning and textures are
226 after Ginibre et al. (2002), Streck (2008) and Renjith (2014).

227

228 4. MAJOR ELEMENT BULK COMPOSITION

229 Studied samples show a continuous series from mafic to felsic compositions, with SiO₂ ranging 46.5-67.6
230 wt%, and Na₂O + K₂O ranging 3.4-9.2 wt% (with K₂O/Na₂O < 1) (Fig. 3a; Table 1). LHPCS mafic rocks (SiO₂<
231 50 wt%; 3 samples) show composition with SiO₂ 46.5-49.4 wt%, Al₂O₃ 16.2-17.1 wt%, CaO 9.8-10.7 wt%,
232 MgO 8.0-8.4 wt% with Mg# (molar MgO/[MgO+FeO_{tot}]) = 60-61 and Na₂O+K₂O ranging 3.4-3.5 wt%. LHPCS
233 intermediate rocks (50<SiO₂<63 wt%; 8 samples) contain 54.4-62.1 wt% SiO₂, with Al₂O₃ 15.7-20.7 wt%,
234 Na₂O+K₂O 5.3-7.1 wt%, MgO 2.2-3.6 wt% (Mg# 43-51), and low CaO 4.6-8.5 wt%. LHPCS felsic rocks
235 (SiO₂>63 wt%; 2 samples) show SiO₂ ranging 64.9-67.6 wt%, associated with Al₂O₃ 15.5-15.8 wt%, MgO 0.7-
236 1.2 wt% (Mg#: 26-34), CaO 2.1-2.8 wt%, and Na₂O+K₂O 8.2-9.2 wt%.

237 On the total alkali versus silica (TAS) diagram (Le Maitre et al., 2002) LHPCS lavas span from basalt to
238 trachyte (Fig. 3b). Los Humeros mafic rocks fall in the “Basalt” field and, following the existing literature
239 (e.g., Barberi et al., 1975, Bellieni et al., 1983; Le Maitre et al., 2002; White et al., 2009; Giordano et al.,
240 2012), can be classified as mildly-alkaline (or transitional) basalts and alkali-basalts. The high TiO₂ contents
241 (1.34-1.5 wt%), together with MgO <12 wt% and low Al₂O₃/TiO₂ values (average value 11.5) exclude the LH
242 mafic rocks as high-Mg melts (picrites) or komatiites (e.g., Redman and Keays, 1985; Arndt and Jenner,
243 1986; Le Maitre et al., 2002; Gao and Zhou, 2013; Azizi et al., 2018a, 2018b).

244 Intermediate products fall in the “Basaltic trachyandesites” and “Trachyandesites” fields; these rocks will
245 be referred hereafter as “trachyandesites”. The Los Humeros felsic (i.e., SiO₂ >63 wt%) lava samples fall in
246 the “Trachyte” field. Selected Harker diagrams for major elements are presented in Figure 3, using SiO₂ wt%
247 as differentiation index. Negative correlations are observed for CaO (Fig. 3c) and Mg# (Fig. 3d), whereas a
248 positive correlation is observed for Na₂O (Fig. 3c).

249

250 5. PETROGRAPHY

251 5.1 Basalts

252 LHPCS basalts show vesicle-rich (up to 35 vol%) highly porphyritic (phenocrysts up to 50 vol%) textures (Fig.
253 4a-d). Studied basalts do not show presence of fragments from host-rocks or from previous magmatic
254 rocks, therefore can be defined as lithic-free (e.g., Geshi and Oikawa, 2014). The magmatic fabric is fluidal

255 as defined by the alignment of plagioclase laths in the groundmass. Based on the presence of clinopyroxene
256 (Cpx) in the mineral assemblage, basalts can be further subdivided into: (i) Cpx-free basalt of the extra-
257 caldera Texcal lava flow (LH18); and (ii) Cpx-bearing basalts of the intra-caldera lavas at western Los
258 Potrereros and at Xalapasco crater (LH5-2 and LH27-1, respectively).

259 Cpx-free basalt (LH18) contains euhedral to subhedral olivine (ca. 20 vol%) and euhedral to anhedral
260 plagioclase (ca. 25-30 vol%) phenocrysts in a holocrystalline groundmass. The latter **consists** of plagioclase
261 with swallow-tail morphology, dendritic to spinifex olivines and opaque oxides (Fig. 4a, b). Olivine and
262 plagioclase phenocrysts are generally slightly chemically zoned (see below), showing homogeneous cores
263 with normal concordant monotonous zoning texture at outer rim (Fig. 4a, b). Major phenocrysts of olivine
264 (up to 2.5 mm in size) with Cr-spinel inclusions are observed (Fig. 4a). **No** pyroxenes are observed in all
265 samples collected from Texcal basalt.

266 Cpx-bearing intra-caldera basalts (LH5-2, LH27-1) show euhedral to subhedral plagioclase (ca. 25 vol%),
267 euhedral olivine (ca. 10-15 vol%), subhedral to anhedral yellow to colorless clinopyroxene (ca. 10-15 vol%)
268 and rare subhedral anorthoclase (< 2 vol%) phenocrysts (Fig. 4c) in a holocrystalline groundmass (Fig. 4d).
269 The latter is made up of (in order of abundance) elongated platy plagioclase, olivine, colorless to green
270 clinopyroxene, opaque oxides and rare alkali-feldspar. All phenocrysts show core-rim zoning textures (Fig.
271 4c, d): (i) olivine, plagioclase and clinopyroxene with homogeneous cores and normal concordant
272 monotonous zoning **texture** at outer rims, (ii) plagioclase and clinopyroxene with homogeneous cores and
273 low-amplitude euhedral oscillatory zoning **texture** at rims, (iii) rare plagioclase and clinopyroxene with
274 homogeneous cores and normal concordant step zoning **texture** at rims, and (iv) very rare plagioclase with
275 patchy cores and normal convolute monotonous zoning **texture** at rims. Large phenocrysts of olivine (up to
276 1.5 mm in size) and plagioclase (up to 3 mm in length) are commonly observed. Vesicle size is up to 5mm in
277 diameter.

278

279 **5.2 Trachyandesites**

280 LHPCS intermediate volcanic products are lithic-free and show low- to medium-porphyritic textures
281 (phenocrysts ranging 10-40 vol%), with a general fluidal fabric as indicated by orientation of plagioclase and
282 clinopyroxene laths in the groundmass (Fig. 4e, f). Intermediate products vary from poorly vesicular (< 10
283 vol% in LH13) to vesicle-rich (ca. 30 vol% in LH4) lavas. In the highest vesiculated sample (LH4), size of
284 vesicles (3-5 mm in diameter) is comparable to those of intra-caldera basalts (LH5-2, LH27-1). Based on the
285 presence of orthopyroxene (Opx) in the mineral assemblage, trachyandesites can be further subdivided
286 into: (i) Opx-free (LH21, LH15); and (ii) Opx-bearing (LH4, LH13, LH17, LH26-1, LH26-2, LH27-2)
287 trachyandesites.

288 Opx-free trachyandesites shows euhedral to subhedral plagioclase (ca. 15-20 vol%), euhedral to subhedral
289 olivine (ca. 10 vol%), euhedral to anhedral yellow-to-colorless clinopyroxene (ca. 10-20 vol%), subhedral

290 alkali-feldspars (ca. 10-15 vol%) phenocrysts, in a holocrystalline microcrystalline groundmass composed of
291 elongated platy plagioclase, colorless clinopyroxene, **olivine**, alkali-feldspar and opaque oxides, in order of
292 microlites abundance.

293 Opx-bearing trachyandesites are generally characterized by euhedral to subhedral plagioclase (ca. 15-20
294 vol%), euhedral to subhedral clinopyroxene (ca. 10-20 vol%), euhedral colorless orthopyroxene (ca. 10-20
295 vol%), euhedral to subhedral alkali-feldspars (ca. 10-15 vol%) and euhedral to subhedral olivine (< 10 vol%)
296 phenocrysts in a holocrystalline to hypohyaline microcrystalline groundmass made of feldspar (plagioclase
297 and alkali-feldspars) microlites, pyroxene (clinopyroxene and orthopyroxene) microlites, olivine microlites,
298 opaque minerals and glass (Fig. 4f). **No olivines are observed in samples collected from the Maxtaloya**
299 **trachyandesite.**

300 Most of phenocrysts observed in LHPCS trachyandesites show zoning textures characterized by
301 homogeneous cores surrounded by (i) monotonous zoning at outer rims, (ii) low-amplitude euhedral
302 oscillatory zoning at rims and (iii) normal concordant step zoning at rims. Homogeneous unzoned
303 clinopyroxene phenocrysts are commonly observed. Major phenocrysts of clinopyroxene (up to 2 mm in
304 size) and plagioclase (up to 2 mm in length) characterized by homogeneous cores and normal concordant
305 monotonous zoning are reported in all studied trachyandesites. **We also report the presence** of (i) rare
306 clinopyroxene phenocrystals with growth mantle **texture**, (ii) rare plagioclase **phenocrysts with rounded**
307 **patchy cores**, (iii) very rare clinopyroxenes with homogeneous cores and growth mantle texture at rims are
308 observed. **Very rare large olivine phenocrysts (1.5-2.0 mm in size) presenting resorption patterns at rim and**
309 **characterized by spinel inclusions are reported in the LH26-1 sample.**

310

311 **5.3 Trachytes**

312 LHPCS trachytes show lithic-free phyric textures, with low porphyritic index (phenocrysts ranging 10-25
313 vol%), and fluidal fabrics as shown by iso-orientation of plagioclase, alkali-feldspars and clinopyroxene laths
314 in the groundmass (Fig. 4g, h). They range from vesicle-poor (< 5 vol%) to vesicle-free textures, with size of
315 vesicles never exceeding 0.05 mm in diameter. The two analyzed trachytic samples (LH5-1 and LH6) are
316 both characterized by the presence of orthopyroxene; however, the two mineral assemblages differ
317 substantially.

318 The low-SiO₂ (64.93 wt%) LH5-1 trachyte is characterized by euhedral to subhedral phenocrysts of
319 plagioclase (ca. 10-15 vol%), clinopyroxene (ca. 10 vol%), orthopyroxene (ca. 10 vol%), olivine (ca. 5-10
320 vol%) and sanidine (< 10 vol%), in a hypohyaline microcrystalline groundmass made of (in order of
321 abundance) sanidine, orthopyroxene, clinopyroxene, rare plagioclase, rare olivine, rare opaque minerals
322 and very rare glass. All phenocrysts are generally unzoned. **Mafic phenocrysts with homogeneous cores**
323 **surrounded by rims showing normal concordant monotonous zoning textures are also observed.** Rare
324 major plagioclase (up to 1.5 mm in length) phenocrysts present patchy cores and normal concordant step

325 zoning **texture** at rims. Rare major clinopyroxene (up to 1.0 mm in length) unzoned homogeneous
326 phenocrysts show inclusions of olivine + magnetite.

327 The high SiO₂ (67.58 wt%) LH6 trachyte is made up of sanidine (ca. 10 vol%), plagioclase (ca. 5-10 vol%) and
328 orthopyroxene (ca. 10 vol%) phenocrysts in a fine grained trachytic mesostasis. Only major plagioclase and
329 orthopyroxene phenocrysts show core-rim zoning textures with homogeneous cores associated either with
330 normal monotonous zoning or normal low-amplitude oscillatory zoning **textures** at rims. Dimension of
331 phenocrysts are comparable to those of LH5-1 trachyte.

332

333 **6.MINERAL CHEMISTRY**

334 Mineral compositions as obtained from electron microprobe analyses and mineral formulae for mineral
335 assemblages of LHPCS lavas are presented in Supplementary Tables 1, 2, 3, 4 and 5 (for feldspar,
336 clinopyroxene, olivine, orthopyroxene and spinel and opaque minerals, respectively).

337

338 **6.1 Feldspar**

339 In basaltic rocks (Fig. 5a), feldspars are predominantly plagioclase. Plagioclase phenocrysts show anorthitic
340 ($X_{An} = 59-81\%$, average 67%) cores and normally zoned ($X_{An} = 42-59\%$, average 53%) rims. Orthoclase
341 component (X_{Or}) is always less than 2%. Plagioclase microlites in the groundmass show andesine ($X_{An} = 19-$
342 60%) composition, with X_{Or} ranging 1-7%. Alkali-feldspars occur as both rare anorthoclase phenocrysts
343 ($Ab_{60}Or_{37}$), and microlites in groundmass ($Ab_{62-79}Or_{9-35}An_{0-13}$).

344 Plagioclase from trachyandesites (Fig. 5b) have anorthite-rich ($X_{An} = 45-87\%$, average 67%) cores and
345 normally zoned ($X_{An} = 27-69\%$, average 48%) rims. Cores with X_{An} in the range 72-87% are observed in all
346 major phenocrysts. Plagioclase core compositions are comparable to those of basalts. The X_{Or} ranges 1-8%.
347 Plagioclase microlites in groundmass show andesine ($X_{An} = 29-63\%$) composition with X_{Or} always less than
348 10%. Alkali-feldspars occur as (i) anorthoclase ($Ab_{59-68}Or_{11-30}$) and sanidine ($Ab_{49-50}Or_{43-48}$) phenocrysts, and
349 (ii) anorthoclase ($Ab_{49-70}Or_{15-38}$) and sanidine ($Ab_{38-48}Or_{47-61}$) microlites in groundmass.

350 Trachytes (Fig. 5c) show generally unzoned plagioclase phenocrysts with oligoclase-andesine ($X_{An} = 26-$
351 45%) composition. Rare An-rich ($X_{An} = 52-70\%$) cores are reported from major plagioclase phenocrysts in the
352 low-silica trachyte LH5-1. The X_{Or} is always less than 8%. Plagioclase microlites in groundmass are rare, with
353 Ab-rich ($An_{21-30}Ab_{66-69}Or_{4-10}$) composition. Alkali-feldspar is represented by anorthoclase as phenocrysts
354 ($Ab_{65-66}Or_{20-21}$) and groundmass microlites ($Ab_{64-66}Or_{21-24}$).

355

356 **6.2 Clinopyroxene**

357 Apart from the LH18 basalt and LH6 trachyte, **clinopyroxene is the most abundant mafic phase in LHPCS**
358 **analyzed samples**. It occurs generally as single crystal (Fig. 4e). However rare crystals showing growth
359 mantle **texture** are locally reported in trachyandesites. Very rare phenocrysts in trachyandesites show

360 patchy cores. Major clinopyroxene phenocrysts in trachyandesites and trachytes contain inclusions (Fig. 4e,
361 g) of olivine, magnetite and plagioclase.

362 Polarized light microscopy coupled with BSE images and chemical investigations highlighted the presence of
363 unzoned (Fig. 4g) and zoned (homogeneous cores surrounded by low-amplitude oscillatory zoning or
364 normal monotonous zoning or normal step zoning textures at rims; e.g., Fig. 4e) clinopyroxene phenocrysts.
365 Very rare phenocrysts showing growth mantle texture at rim are reported. No evidence of
366 resorption/dissolution textures are observed in LHPCS analyzed samples.

367 The Cpx population, based on textural observations and mineral chemistry, (Fig. 6 a-f) can be classified in
368 five major categories: (i) Cpx1 cluster is represented by homogeneous cores of all zoned phenocrysts in
369 basalts; (ii) Cpx2 population is represented by homogeneous cores of all zoned phenocrysts from
370 trachyandesites and trachytes; (iii) Cpx3 group represents both the unzoned phenocrysts in all studied
371 samples and the rims (low-amplitude oscillatory, normal monotonous and normal step zoning textures) of
372 cpx1 and cpx2 phenocrysts from all studied samples; (iv) Cpx4 population is constituted by microlites and
373 microphenocrystals in groundmass from all analyzed samples; and (v) Cpx5 cluster collects together the
374 emerald-green euhedral to subhedral microlites in groundmass of intra-caldera basalts (LH5-2, LH27-1) and
375 the rare green outer rims of major clinopyroxene (Cpx2) phenocrysts from few trachyandesites (LH15,
376 LH17, LH26-2).

377 The Cpx1 shows Mg# of 45-75, Ca 0.78-0.90 apfu, Q+J 1.84-1.94 and J/(J+Q) 0.03-0.06, and it can be
378 classified as Ti-rich augite ($Wo_{41-48}En_{25-42}Fs_{14-32}$).

379 The Cpx2 shows a Mg# of 59-84, Ca 0.20-0.92 apfu, Q+J 1.77-1.95 and J/(J+Q) 0.01-0.06, and it can be
380 classified as diopside-rich augite ($Wo_{11-48}En_{36-64}Fs_{9-32}$).

381 The Cpx3 shows Mg# of 20-86, Ca 0.27-0.97 apfu, Q+J 1.57-1.98 and J/(J+Q) 0.01-0.07, and it can be
382 classified as diopside-rich augite ($Wo_{12-49}En_{14-57}Fs_{8-62}$). The composition of Cpx3 partially overlaps those of
383 Cpx1 and Cpx2 groups, as it would be expected for phenocrysts with homogeneous cores (i.e. Cpx1 and
384 Cpx2) and the respective rims (Cpx3) characterized by low-amplitude oscillatory zoning or normal
385 monotonous zoning textures (e.g., Streck, 2008).

386 The Cpx4 shows Mg# of 31-81, Ca 0.24-0.87 apfu, Q+J 1.87-1.97 and J/(J+Q) 0.01-0.06, corresponding to
387 diopside-rich augite ($Wo_{12-46}En_{18-60}Fs_{11-38}$). The composition of Cpx4 partly overlaps that of Cpx3, however
388 their textural characteristics are completely different.

389 The Cpx5 differs from previous pyroxenes, with a large spread in Mg# ranging 5-73, Ca 0.03-0.83 apfu, Q+J
390 1.51-2.07 and J/(J+Q) 0.07-0.89. The Cpx5 can be classified as Aegirine-Augite ($Na < 0.3$ apfu, $X_{Aeg} < 0.30$;
391 with $X_{Aeg} = Na$ apfu if $Na < Fe^{3+ Tot}$, $X_{Aeg} = Fe^{3+ Tot}$ apfu if $Na > Fe^{3+ Tot}$) to Aegirines ($Na = 0.68-0.88$ apfu, $X_{Aeg} =$
392 $0.40-0.88$). Cpx5 clinopyroxenes are generally Ti-enriched (TiO_2 up to 2.8 wt%, Ti up to 0.08 apfu) and
393 straddle the $Q+J=2$ line defining the boundary for “normal” pyroxenes (Morimoto, 1989), thus indicating
394 the presence of a $NaR^{2+}_{0.5}Ti^{4+}_{0.5}Si_2O_6$ component (Morimoto, 1988, 1989; Huraiova et al., 2017) (Fig. 6c).

395 The compositional variation of clinopyroxenes can be summarized in the Na vs. Ti diagram (Fig. 6e-f).
396 Interestingly, Augite-rich (Cpx1, Cpx2, Cpx3 and Cpx4) clinopyroxenes generally show positive correlation
397 and linear distribution characterized by a progressive Ti- and Na-depletion, from Ti-Augite cores (Cpx1) in
398 basalts to DiHd-rich Augite (Cpx3, Cpx4) specimens in trachytes. The Cpx5, with Aegirine-Augite and
399 Aegirine **compositions**, diverges from this trend. It shows a negative correlation characterized by a
400 progressive enrichment of Na content, with respect to a general Ti-depletion. Aegirine enrichment could be
401 diagnostic of ferric iron (Fe³⁺) content increasing during the magmatic differentiation, whereas the
402 diopside-hedenbergite enrichment could testify an increase of ferrous iron (Fe²⁺) in magma (e.g. Huraiova
403 et al., 2017).

404

405 **6.3 Olivine**

406 Olivine is found in all analyzed samples, except for LH27-2 trachyandesite and LH6 trachyte. It consists of
407 idiomorphic (Fig. 4 a, c) to skeletal (e.g., Donaldson, 1974; Fowler et al., 2002; Faure et al., 2003; Welsch et
408 al., 2013) (Fig. 4b) phenocrysts, and microlites in the groundmass (Fig. 4h). Olivine crystals, both
409 phenocrysts and microcrystals, show homogeneous cores **and concordant normal monotonous zoning**
410 **textures at outer rims**. In basalts, olivine shows a continuous compositional range (Fig. 7a) from
411 Fo₈₆Fa₁₄MtC₀Tep₀ (phenocryst in LH5-2 basalt) to Fo₀₅Fa₉₁MtC₁Tep₃ (groundmass microlites in LH27-1
412 basalt). The highest MnO (up to 1.7 wt%) values are systematically found in Fe-rich olivine microlites in
413 basalts. Low monticellite concentration (CaO always < 1.0 wt%) in LHPCS samples is typical for magmatic
414 olivine (i.e., Melluso et al., 2014). CaO content positively correlates with the fayalite (FeO) compound (Fig.
415 5a). Together with the Mg#, the CaO content allows to discriminate olivine phenocrysts in three coherent
416 compositional clusters: i) olivine from basalts, with Mg#= 79-87 and CaO= 0.21-0.73 wt%, ii) olivine from
417 trachyandesites, with Mg#= 67-80 and CaO= 0.08-0.43 wt%, and iii) olivine from trachytes with Mg#= 58-63
418 and CaO= 0.16-0.42 wt%. A minor number of analyzed phenocrysts in basalts show Cr₂O₃ content in the
419 range ca. 0.05-0.07 wt%. **Cr₂O₃ is**, instead, below detection limit for almost all analyzed olivine crystals in
420 LHPCS lavas. A minor cluster of peridotite Mg-olivine (Fo₉₉Fa₁) xenocrysts, characterized by disequilibrium
421 textures (resorption patterns) at rim, have been identified in LH26-1 trachyandesite lava.

422

423 **6.4 Orthopyroxene**

424 Orthopyroxene occurs in most of the LHPCS trachyandesite (Fig. 4f) and trachyte samples (Fig. 4 g-h).
425 Orthopyroxene phenocrysts are generally unzoned with homogeneous textures. In trachyandesites, they
426 show intermediate (En₄₁₋₈₃FS₁₄₋₅₅WO₂₋₁₀) compositions (Fig. 7b), with Mg# of 43-86, Al₂O₃ up to 2.12 wt%,
427 TiO₂ 0.08-1.33 wt%, and CaO 1.20-4.72 wt%. Similar compositions (En₆₂₋₇₉FS₁₈₋₃₃WO₃₋₇) have been obtained
428 for microlites in groundmass (Fig. 7b) with Mg# of 65-81, Al₂O₃ 0.48-1.53 wt%, TiO₂ 0.21-0.60 wt% and CaO
429 1.35-3.49 wt%.

430 In trachytes, orthopyroxene phenocrysts present Mg# ranging 59-65, with low Al₂O₃ (0.18-0.73 wt%), low
431 TiO₂ (0.11-0.32 wt%) and CaO (0.81-1.88 wt%), corresponding to Fe-rich composition (En₅₆₋₆₃Fs₃₄₋₃₉Wo₂₋₄)
432 with a minor Ca-Cpx substitution (Fig. 7b). Orthopyroxene microlites in groundmass (Fig. 7b) show
433 comparable hypersthene (En₄₆₋₆₀Fs₃₅₋₄₅Wo₃₋₇) composition with Mg# of 50-63, Al₂O₃ 0.25-0.82 wt%, TiO₂
434 0.19-0.31 wt% and CaO 1.32-3.27 wt%.

435 The compositional variation of **orthopyroxene** is summarized in Al^{Tot} vs. Mg# diagram (Fig. 7c).
436 Orthopyroxene crystals from trachyandesites are characterized by higher content of Al (apfu) and higher
437 Mg#, whereas those from trachytes are richer in ferrous iron (lower Mg# values) and in manganese (Mn up
438 to 0.04 apfu).

439

440 **6.5 Spinel and Opaque Minerals**

441 Basalts show a diversified set of opaque minerals. Phenocrysts are (in order of abundance): i) Al-spinel (TiO₂
442 0.58-1.00 wt%; Mg# 58-71; Cr# 21-30, with [Cr# = 100 Cr/(Cr+Al)]), ii) Ti-magnetite (TiO₂ 1.83-21.58 wt%;
443 MgO 0.06-2.19 wt%; MnO 0.44-0.63 wt%) and (iii) ilmenite (MgO up to 2.18 wt%). Groundmass is
444 characterized by Fe-Ti oxides (ca. 20-30 μm in diameter; Fig. 4f) as ilmenite (MgO 0.27-1.50 wt%) and Ti-
445 magnetite (MgO 0.18-1.89 wt%). Cr-spinels (TiO₂ 3.37-8.55 wt%; Mg# 14-28; Cr# 62-72) are found just as
446 inclusions, up to 200 μm in diameter (Fig. 4a), in larger Mg-rich olivine phenocrysts.

447 Trachyandesites are characterized by phenocrysts of Ti-magnetite (MgO 0.07-3.84 wt%), ilmenite (MgO
448 1.11-4.79 wt%) and rare rutile (MgO 0.47 wt%). Groundmass microcrystals (ca. 20-30 μm in diameter) show
449 a comparable composition with Ti-magnetite (MgO 0.33-3.77 wt%), ilmenite (MgO 0.33-4.79 wt%) and rare
450 rutile (MgO < 0.05 wt%). Similar to basalts, Cr-spinels (TiO₂ 6.09-6.47 wt%; Mg# 19-21; Cr# 65-68) are found
451 only as inclusions (100-200 μm in diameter) in major Mg-rich olivine phenocrysts.

452 In trachytes, Fe-Ti oxides show euhedral to subhedral habit and, based on chemistry, they are ilmenite
453 (MgO 2.06-3.31 wt%) and Ti-magnetite (MgO 1.41-5.47 wt%). Phenocrysts (up to 50-100 μm in diameter;
454 Fig. 4g) and groundmass microcrystals (ca. 15-20 μm in diameter) show the same compositions.

455

456 **7. MINERAL-LIQUID THERMOBAROMETRY**

457 In order to define the thermobaric (T-P) environmental conditions of the magmatic feeding system of the
458 LHPCS, we integrate thermobarometry models based on olivine (Beattie, 1993; Putirka et al., 2007; Putirka,
459 2008), orthopyroxene (Putirka, 2008), plagioclase (Putirka, 2005b; Putirka, 2008), alkali-feldspar (Putirka,
460 2008) and clinopyroxene (Putirka et al., 1996, 2003; Putirka, 2008; Masotta et al., 2013) chemistry. Due to
461 the paucity/absence of glass, we assume the whole rock composition as representative of the original liquid
462 (or nominal melt) in equilibrium with phenocrysts (Putirka, 1997, 2008; Mordick and Glazner, 2006; Aulinas
463 et al., 2010; Dahren et al., 2012; Barker et al., 2015). We are aware that such a procedure put the focus on
464 early steps of the crystallization history, characterized by high melt/crystal ratios. Relatively late melt

465 compositions, related to the solidification of the groundmass, are not present or can simply not be
466 analyzed. Thermobarometric calculations were developed after the application of mineral-melt equilibrium
467 filters and considering pre-eruptive H_2O^{liq} values obtained through the plagioclase-liquid hygrometer model
468 (eq. 25b in Putirka, 2008). Plagioclase-liquid thermometry and barometry were calculated using eq. (24a)
469 and eq. (25a), respectively, of Putirka (2008), mainly based on the Ca/Na distribution between melt and Pl.
470 Alkali-feldspar-liquid thermometry was calculated considering the K-Na exchange, applying eq. (24b) in
471 Putirka (2008). Olivine-liquid equilibrium thermometry was calculated integrating the models of Beattie
472 (1993) and Herzberg and O'Hara (2002) with the thermometric eq. (2) in Putirka et al. (2007).
473 Orthopyroxene-liquid thermometry was calculated by Fe-Mg partitioning following the model of Beattie
474 (1993; in the revised form [eq. 28a] in Putirka, 2008). Barometry model of Wood (1974) based on the Na
475 and Al content in Opx, in the revised form [eq. 29a] in Putirka (2008), was applied.
476 Clinopyroxene-liquid thermometry and barometry, for diopside-augite pyroxenes in basalts and
477 trachyandesites (groups Cpx1, Cpx2, Cpx3, Cpx4), were calculated by the application of the Jd-DiHd
478 exchange thermometer (Putirka et al, 1996, 2003) using [eq. 33] in Putirka (2008) and the Al-partitioning
479 barometric model [eq. 32c] in Putirka (2008). Clinopyroxene-liquid thermometry and barometry, for
480 diopside-augite pyroxenes in trachytes (groups Cpx3 and Cpx4), were calculated by the application of the
481 Jd-DiHd exchange thermometer (Putirka et al, 1996, 2003; Putirka, 2008) recalibrated for alkaline
482 differentiated magmas using [eqn. Talk33] and [Eqn. Palk 2012], respectively, in Masotta et al. (2013).
483 Clinopyroxene-liquid thermometry and barometry, for augite-aegirine pyroxenes (Cpx5), were calculated
484 integrating [eq. 33] and [eq. 32c] in Putirka (2008) with equations [Eqn. Talk2012] and [Eqn. Palk 2012] in
485 Masotta et al. (2013). Results of mineral-melt equilibrium tests (Figs. 8, 9, 10), hygrometry calculations (Fig.
486 10) and geothermometric estimates are presented contextually in supplementary mineral chemistry tables.
487 Summary of the thermobarometry estimates are reported in a Pressure-Temperature diagram (Fig. 11).

488

489 **7.1 Test for Mineral-Melt Equilibrium**

490 Prerequisite for the application of mineral-liquid thermobarometry models based on mineral-melt
491 equilibrium conditions is to test and verify that the mineral and the chosen liquid compositions represent
492 chemical equilibrium pairs (e.g., Putirka, 2008; Keiding and Sigmarsson, 2012). Petrographic investigations
493 (i.e., polarized light and BSE imaging) and calculation of mineral-liquid partition coefficients were integrated
494 with the aim to select only mineral specimens at equilibrium with the hosting melt (e.g., Putirka, 2008;
495 Keiding and Sigmarsson, 2012).

496 The predominant euhedral to subhedral habit of crystals is generally considered as an evidence of
497 equilibrium with the surrounding melt (e.g., Keiding and Sigmarsson, 2012). **However, the mineral-liquid
498 thermo-barometric modeling requires paying careful attention to phenocrysts showing strongly zoned
499 textures** (patchy-, sector-, reverse-, coarse banding oscillatory-zoning), **or disequilibrium textures**

500 (resorption patterns, dissolution surfaces, reaction rims and mineral mantles/clots) (e.g. Ginibre et al.,
 501 2002; Streck, 2008). These textures imply that core(s) and rim(s), or different portions of the same grain,
 502 crystallized and reacted in an evolving liquid **with a progressively different composition** (e.g., Mordick and
 503 Glazner, 2006; Putirka, 2008; Keiding and Sigmarsson, 2012). As defined by Streck (2008), when crystals are
 504 complexly zoned, it can be difficult to find criteria to be used for evaluation of crystal populations and their
 505 equilibrium with respective hosting melt. However, it is not the case of the LHPCS studied samples, where
 506 phenocryst assemblages generally do not show disequilibrium patterns or complexly zoned textures (e.g.,
 507 Ginibre et al., 2002; Streck, 2008). All microprobe analyses related to those rare crystals presenting
 508 morphological evidence of disequilibrium texture, such as patchy zoning, were discarded.
 509 Then, the mineral-liquid equilibria between liquid and previous selected minerals, were investigated using:
 510 (i) the Fe-Mg exchange coefficient, (ii) the An-Ab partitioning coefficient, and (iii) the comparison between
 511 observed and predicted normative components of minerals.
 512 The partitioning of Fe-Mg between mineral and liquid is known as Fe-Mg exchange coefficient, or $K_D^{Min-Liq}$
 513 $^{Liq}(Fe-Mg)$ (defined as $K_D^{Min-Liq}(Fe-Mg) = [MgO^{Liq}FeO^{Min}]/[MgO^{Min}FeO^{Liq}]$, where *Liq* is the liquid composition,
 514 *Min* is the mineral composition and MgO and FeO are molar fractions; Roeder and Emslie, 1970; Langmuir
 515 and Hanson, 1981; Putirka, 2005a; Putirka, 2008). It is used here to test the equilibrium between mafic
 516 minerals (olivine, orthopyroxene and clinopyroxene) and liquid (e.g., Maclennan et al., 2001; Putirka, 2008;
 517 Stroncik et al., 2009; Aulinas et al., 2010; Keiding and Sigmarsson, 2012; Melluso et al., 2014; Feng and Zhu,
 518 2018).
 519 We calculated $K_D^{Min-Liq}(Fe-Mg)$ values using (i) equation (17) in Putirka (2008) for Ol and Opx; (ii)
 520 temperature-dependent equation (35) in Putirka (2008) for diopsidic-augitic Cpx in basalts and
 521 trachyandesites; and (iii) the Na-corrected equation (35a) in Masotta et al. (2013) for Na-rich Cpx5 group
 522 and for all Cpx from LH5-1 and LH6-1 trachytes. The calculated $K_D^{Min-Liq}(Fe-Mg)$ values for olivine and
 523 orthopyroxene are plotted in a **Rhodes diagram** (Dungan et al., 1978; Rhodes et al., 1979; Putirka, 2005;
 524 Putirka, 2008) to graphically test the equilibrium between Ol (Fig. 8a) or Opx (Fig. 8b) and the respective
 525 hosting melts (Liq). Furthermore, the **Rhodes diagram** is useful to recognize: (i) presence of xenocrystals
 526 and/or antecrystals; (ii) late or groundmass crystallization; (iii) crystal removal (decrease of $Mg\#^{Liq}$ only);
 527 and (iv) closed system crystallization (decrease of $Mg\#^{Min}$ only) by deviations of the measured compositions
 528 from the expected ones (Rhodes et al., 1979; Putirka, 2008; Melluso et al., 2014).
 529 The calculation of $K_D^{Cpx-Liq}(Fe-Mg)$ does not consider variations of Ca and Al contents in Cpx (Rhodes et al.,
 530 1979; Putirka, 1999, 2005b, 2008). Therefore, a further equilibrium test was achieved through the
 531 comparison of analyzed Cpx compositions (as expressed by the components EnFs, DiHd and CaTs; where
 532 CaTs is Ca-Tschermak) with components contents predicted from melt composition (e.g., Putirka, 2008;
 533 Mollo et al., 2010; Jeffery et al., 2013; Barker et al., 2015; Ellis et al., 2017). Normative components of Cpx
 534 were calculated following the scheme proposed in Putirka et al., (1996) and Putirka (2008). Calculation of

535 Cpx components based on melt composition was performed using equations (eq 3.1a) for DiHd, (eq 3.2) for
536 EnFs and (eq 3.4) for CaTs in Putirka (1999). A graphical presentation (e.g., Jeffery et al., 2013; Barker et al.,
537 2015) of this test is shown in Figure 9.

538 The partitioning of An-Ab between mineral and liquid is known as An-Ab exchange coefficient, or $K_D^{Pl-Liq}(An-Ab)$
539 (defined as $K_D^{Pl-Liq}(An-Ab) = [XAb^{Pl}XAlO_{1.5}^{Liq}XCaO^{Liq}]/[XAn^{Pl}XNaO_{0.5}^{Liq}XSiO_2^{Liq}]$, where *Liq* is the liquid
540 composition, *Pl* is the plagioclase composition and all components are in molar fractions; Carmichael et al.,
541 1977; Holland and Powell, 1992; Putirka et al., 2007; Putirka, 2008; Lange et al., 2009; Keiding and
542 Sigmarsson, 2012; Jeffery et al., 2013; Barker et al., 2015; Waters and Lange, 2015). Figure 10 presents a
543 comparison of measured composition of plagioclase with that calculated from the melt composition, using
544 the thermodynamic model eq (31) in Namur et al. (2012). A similar test can be applied for alkali-feldspars
545 (Putirka, 2008).

546 In summary, we accept: (i) Ol with $K_D^{Ol-Liq}(Fe-Mg) = 0.30 \pm 0.06$ (Roeder and Emslie, 1970; Putirka, 2005a;
547 Putirka, 2008 and references therein) (Fig. 8a); (ii) Opx with $K_D^{Opx-Liq}(Fe-Mg) = 0.29 \pm 0.06$ (Putirka, 2008 and
548 references therein) (Fig. 8b); (iii) Cpx with $K_D^{Cpx-Liq}(Fe-Mg) = 0.28 \pm 0.08$ (Putirka, 2008) and verifying the one-
549 to-one (± 0.1) relationship between predicted vs. observed normative components (EnFs, DiHd and CaTs)
550 for at least two of the monitored components (Fig. 9); (iv) Pl with $K_D^{Pl-Liq}(An-Ab) = 0.27 \pm 0.11$ for $T > 1050^\circ C$
551 and $K_D^{Pl-Liq}(An-Ab) = 0.10 \pm 0.05$ for $T < 1050^\circ C$ (Putirka, 2008) or falling within ± 0.1 of the one-to-one
552 relationship between predicted vs observed An components (Fig. 10); and (v) Afs with $K_D^{Afs-Liq}(An-Ab) = 0.27$
553 ± 0.18 (Putirka, 2008). All mineral-liquid pairs exceeding the accepted exchange coefficient values for Ol,
554 Cpx, Opx and Fsp were discarded for thermobarometric analyses.

555

556 7.2 Pre-eruptive H_2O^{Liq} content estimates

557 Thermobarometric models for volcanic systems require an initial estimate of the pre-eruptive water
558 concentration (wt%) in melt (H_2O^{Liq}). It was determined in this work by using the plagioclase-liquid
559 hygrometer model [eq. 25b] in Putirka (2008). Hygrometry calculations were produced after the application
560 of plagioclase-liquid equilibrium filters. The calculated pre-eruptive H_2O^{Liq} wt% values ($\pm 1\sigma$ standard
561 deviation of the weighted mean) are plotted as isolines in Fig. 10. The hygrometer of Putirka (2008)
562 indicates (Fig. 10): (i) H_2O^{Liq} negative values in basalts, from -0.20 to -0.40 wt%, with a weighted mean of -
563 0.37 ± 0.20 wt% (MSWD= 0.0026; n= 95); (ii) trachyandesites pre-eruptive water content in the range
564 H_2O^{Liq} : 0 – 1.40 wt% (weighted mean of 0.57 ± 0.13 wt%, MSWD= 0.13, n= 245); and (iii) trachytes with the
565 highest water concentration (H_2O^{Liq} : 1.40 – 1.90 wt%; weighted mean of 1.46 ± 0.32 wt%, MSWD= 0.059, n=
566 37). Following the approach of Keiding and Sigmarsson (2012), negative values in basalts are interpreted as
567 anhydrous melt compositions. Coherently with the existing literature (e.g., Webster et al., 1999), the
568 anhydrous character is then assumed as a $H_2O^{Liq} < 1$ wt% content.

569 Application of plagioclase-liquid hygrometer model (Putirka, 2008) defines anhydrous environment for
570 pressure-temperature calculations in LHPCS basalts. Whereas hydrous conditions are required for evolved
571 LHPCS melts and in particular for trachytic lavas, where the effect of 1 wt% H₂O is expected to generate a
572 temperature decrease of ca. -40 °C and a pressure increase of ca. + 1.0 kbar in geothermometers and
573 geobarometers, respectively (Putirka, 2008; Keiding and Sigmarsson, 2012).

574 On contrary, existing studies (e.g., Kushiro, 1969; Sisson and Grove, 1993; Yang et al., 1996; Putirka, 2005a,
575 2005b, 2008; Kelley and Barton, 2008; Keiding and Sigmarsson, 2012) demonstrated a negligible effect of
576 water for basaltic and intermediate melts showing H₂O^{Liq} ranging 0 – 1 wt%.

577

578 **7.3 Thermobarometry Results**

579 **7.3.1 Basalts**

580 When applied to phenocryst cores, the Pl-Liq thermobarometry (Fig. 11a-c) show that all LHPCS basaltic
581 materials have magmatic anhydrous T in the range 1230-1266 °C (weighted mean of 1250 ± 5 °C, ±1σ
582 standard deviation of the weighted mean, MSWD= 0.112, n= 95). Pressure estimates are in the range 6.5-
583 8.7 kbar (weighted mean of 7.9 ± 1.1 kbar, ±1σ standard deviation of the weighted mean, MSWD= 0.024,
584 n= 28) for LH18 Ol-basalts, and 7.2-10.3 kbar (weighted mean of 9.2 ± 0.7 kbar (±1σ), MSWD= 0.064, n= 67)
585 for LH5.2 and LH27.1 Ol-Cpx-basalt. Olivine-melt equilibrium (Fig. 11a-c), for the olivine compositional
586 range of Fo 80-85%, yields T window of 1240-1297 ± 27 °C (±1σ), consistent with the results obtained with
587 Pl-Liq thermometry. The Cpx-thermobarometry (Fig. 11a, c), for both Cpx1 (phenocryst cores) and Cpx3
588 (phenocryst rims and unzoned phenocrysts), provides temperature of 1006-1209 °C (weighted mean of
589 1124 ± 12 °C (±1σ), MSWD= 3.4, n= 82). **Pressure estimates are in the range** 3.1-11.5 kbar (weighted mean
590 of 7.6 ± 0.8 kbar (±1σ), MSWD= 2.7, n= 36) for Cpx1, and 2.5-7.7 kbar (weighted mean of 4.0 ± 0.8 kbar
591 (±1σ), MSWD= 0.63, n= 14) for Cpx3. Thermobaric estimates for Cpx4 (microlites in groundmass) indicate
592 shallow conditions (0.3 – 3.0; weighted mean of 1.6 ± 1.2 kbar (±1σ), MSWD= 0.38, n= 6) for temperatures
593 (1006-1123 °C; weighted mean of 1060 ± 54 °C (±1σ), MSWD= 2.9, n= 6) comparable to those obtained for
594 Cpx1 and Cpx3. Higher temperature estimates (1067-1221 °C; weighted mean of 1157 ± 53 °C (±1σ),
595 MSWD= 2.4, n= 7) **at low-pressure conditions** (0.4-4.7; weighted mean of 2.9 ± 1.1 kbar (±1σ), MSWD=
596 0.83, n= 7) are instead obtained for a limited number of Cpx5 (aegirine-rich) compositions (Fig. 11a, c).

597

598 **7.3.2 Trachyandesites**

599 Based on the Opx- presence/absence criterion, two populations of trachyandesites have been
600 discriminated in this study.

601 Opx-free trachyandesites LH15 and LH21-2 (El Limón and Sarabia lava flows, respectively) are characterized
602 by i) plagioclase phenocryst cores crystallized at T of 1190-1263 °C (weighted mean of 1248 ± 7 °C (±1σ),
603 MSWD= 1.09, n= 39) and P of 4.8-9.4 kbar (weighted mean of 7.7 ± 0.9 kbar (±1σ), MSWD= 0.14, n= 39); ii)

604 comparable temperature (1193-1263 °C; weighted mean of 1227 ± 37 °C ($\pm 1\sigma$), MSWD= 2.3, n= 6) and
605 pressure (6.7-9.6 kbar, mean value of 7.8 ± 2.4 kbar ($\pm 1\sigma$), MSWD= 0.101, n= 6) obtained for rare
606 phenocryst rims and microlites at equilibrium; iii) olivine-melt equilibrium (with Fo: 75-80%) showing a T
607 window of $1030-1055 \pm 27$ °C ($\pm 1\sigma$); iv) rare Cpx2 (clinopyroxene phenocryst cores) showing equilibrium
608 with melt and yielding T $1061-1239$ °C (weighted mean of 1116 ± 29 °C ($\pm 1\sigma$), MSWD= 2.3, n= 12) and P ca.
609 2.9 -8.3 kbar (weighted mean of 5.2 ± 1.2 kbar ($\pm 1\sigma$), MSWD= 1.5, n= 12); v) Cpx3 (rims of and unzoned
610 phenocrysts) showing equilibrium with melt and yielding thermobarometric results (T $938-1139$ °C, with
611 weighted mean of 1074 ± 15 °C ($\pm 1\sigma$), MSWD= 1.9, n= 32; and P 1.0-4.4 kbar with weighted mean of $2.8 \pm$
612 0.5 kbar ($\pm 1\sigma$), MSWD= 0.22, n= 32); vi) Cpx4 (groundmass microcrystals) compositions indicating, with
613 respect to Cpx3, comparable temperatures ($1026-1127$ °C, with weighted mean of 1059 ± 16 °C ($\pm 1\sigma$),
614 MSWD= 0.71, n= 14) at lower pressure conditions (0.3 – 3.6 kbar with weighted mean of 1.4 ± 0.8 kbar
615 ($\pm 1\sigma$), MSWD= 0.35, n= 14). The unique Cpx5-liquid pair at equilibrium yielded P-T conditions of 5.6 ± 1.5
616 kbar and 1122 ± 30 °C.

617 Thermobarometric estimates (Fig. 11a, d) for Opx-bearing trachyandesites (LH4, LH13, LH17; LH26-1; LH26-
618 2; LH27-2) show overlapping P-T conditions for plagioclase populations with: i) phenocryst cores
619 crystallizing at T $1145-1228$ °C (weighted mean of 1187 ± 4 °C ($\pm 1\sigma$), MSWD= 1.17, n= 166) and P 4.1-7.7
620 kbar (weighted mean of 5.8 ± 0.5 kbar ($\pm 1\sigma$), MSWD= 0.059, n= 166), and ii) phenocryst rims and
621 microcrystals forming at T $1140-1224$ °C (weighted mean of 1168 ± 8 °C ($\pm 1\sigma$), MSWD= 0.92, n= 34) and P
622 4.4-8.5 kbar (weighted mean of 6.4 ± 1.0 kbar ($\pm 1\sigma$), MSWD= 0.14, n= 34). Lower temperatures ($1050-1090$
623 ± 27 °C ($\pm 1\sigma$)) are obtained using olivine (Fo 70-80%) – liquid equilibrium model.

624 Thermobarometers applied to pyroxenes indicate: i) Cpx2 (phenocryst cores) crystallizing at T $979-1204$ °C
625 (weighted mean of 1060 ± 8 °C ($\pm 1\sigma$), MSWD= 1.8, n= 101) and P 3.4 -11.5 kbar (weighted mean of $7.0 \pm$
626 0.3 kbar ($\pm 1\sigma$), MSWD= 0.94, n= 101), ii) Cpx3 crystallizing at T $959-1106$ °C (weighted mean of 1026 ± 6 °C
627 ($\pm 1\sigma$), MSWD= 1.3, n= 145) and P 1.2-6.9 kbar (weighted mean of 4.3 ± 0.2 kbar ($\pm 1\sigma$), MSWD= 0.72, n=
628 145), iii) rare Cpx4 showing general equilibrium with melt and forming at P-T conditions of T $920-1123$ °C
629 (weighted mean of 1020 ± 21 °C ($\pm 1\sigma$), MSWD= 2.7, n= 24) and P 0.1-3.4 kbar (weighted mean of 1.8 ± 0.6
630 kbar ($\pm 1\sigma$), MSWD= 0.56, n= 24), and iv) Opx yielding crystallization conditions, for both phenocrysts and
631 microlites, of T $1048-1123$ °C (weighted mean of 1078 ± 5 °C ($\pm 1\sigma$), MSWD= 0.24, n= 129) and P 0 -2.8 kbar
632 (weighted mean of 1.1 ± 0.6 kbar ($\pm 1\sigma$), MSWD= 0.057, n= 84). In all trachyandesite samples, temperature
633 estimates obtained through the Ol-Liq model and the Cpx-Liq model are comparable (Fig. 11a, d), whereas
634 the Pl-Liq model shows higher T values. These results can be interpreted as an earlier plagioclase
635 crystallization with respect to olivine and clinopyroxene. Furthermore, orthopyroxene (Opx) can be
636 considered a tracer of trachyandesitic magma stagnations at shallow depths, as indicated by the lower
637 pressure estimates obtained through the Opx-liquid barometer.

638

639 **7.3.3 Trachytes**

640 Magmatic P-T conditions (Fig. 11a, e) of trachytic (LH5.1 and LH6) melts are defined by: i) plagioclase
641 crystallization at T 1050-1094 °C (weighted mean of 1069 ± 6 °C ($\pm 1\sigma$), MSWD= 0.39, n= 37) and P 4.7-9.0
642 kbar (weighted mean of 6.5 ± 1.0 kbar ($\pm 1\sigma$), MSWD= 0.20, n= 37), ii) olivine (Fo55-65%) – liquid regression
643 indicating olivine crystallization at $900-920 \pm 27$ °C ($\pm 1\sigma$), iii) clinopyroxene crystallization, both phenocrysts
644 (Cpx3) and groundmass (Cpx4), at temperature of ca. 955 °C (weighted mean of 956 ± 14 °C ($\pm 1\sigma$), MSWD=
645 0.00056, n= 17) and very shallow-depth conditions (P weighted means of 2.3 ± 0.9 kbar ($\pm 1\sigma$), MSWD=
646 0.047, n= 10 and 1.6 ± 1.1 kbar ($\pm 1\sigma$), MSWD= 0.04, n= 7; for Cpx3 and Cpx4, respectively). Shallow-depth
647 conditions are also obtained for orthopyroxene crystallization with T 960-1006 °C (weighted mean of $990 \pm$
648 7 °C ($\pm 1\sigma$), MSWD= 0.28, n= 49) and P 0.2-3.6 kbar (weighted mean of 1.6 ± 0.9 kbar ($\pm 1\sigma$), MSWD= 0.101,
649 n= 35). The alkali-feldspar-liquid thermometer provided temperature estimates always <500°C, here
650 interpreted as feldspar re-equilibration in subsolvus/subsolidus post-eruptive conditions (Nekvasil, 1992;
651 Brown and Parsons, 1994; Plumper and Putnis, 2009; Kontonikas-Charos et al., 2017; Latutrie et al., 2017).
652 Interestingly, temperatures obtained through Pl-Liq model are higher than those obtained with Ol-Liq, Cpx-
653 Liq and Opx-Liq, suggesting an earlier crystallization of plagioclase with respect to mafic minerals.
654 Moreover, the Pl-Liq models indicate thermobaric estimates comparable to those obtained for
655 trachyandesitic rocks.

656

657

658 8. DISCUSSION

659 8.1 Major-elements mass balance modeling

660 Based on the textural **evidences** documenting: (i) Cpx-bearing basalts being mainly characterized by
661 euhedral olivine and plagioclase and subhedral-anhedral clinopyroxene, indicating crystallization of olivine
662 and plagioclase prior to clinopyroxene (e.g., Bindeman and Bailey, 1999); and (ii) all LHPCS volcanic rocks
663 not showing disequilibrium textures (such as fine-sieve textures, resorption surface, crystal clots,
664 disequilibrium growth-mantel, reverse zoning, reaction-rims, breakdown mantle and dissolution; e.g.,
665 Streck, 2008) typical of AFC-mixing processes, we suggest that the studied LHPCS volcanic rocks represent
666 cogenetic melts, belonging to the same line of descent, excluding major mass-change due to assimilation
667 and mixing (AFC-mixing) processes. In order to test this hypothesis, we applied fractional crystallization (FC)
668 modeling (e.g., White et al., 2009; Moghadam et al., 2016; Lucci et al., 2016). The FC-modeling is focused
669 on these hypotheses: (i) direct cogenetic relationship between all LHPCS basalts, and (ii) common genesis
670 for all LHPCS trachyandesites and trachytes through differentiation via fractional crystallization starting
671 from the same basaltic parental melt.

672 Major-elements mass balance models (e.g., Bryan et al., 1969) can be used to test and define relative
673 **proportions** of phases involved in Rayleigh fractional crystallization (RFC, Daughter = Parent - fractionating
674 assemblage) and crystal accumulation (Cumulate = Melt + accumulated assemblage) hypotheses (e.g.,
675 White et al., 2009; Moghadam et al., 2016; Lucci et al., 2016).

676 If Parent melt (for RFC) or Cumulate (for crystal accumulation) **compositions are assumed** as matrix **b**, and
677 the FC-model is solved for **b**, then **b** = Liquid (Daughter or Melt) + Minerals (fractionating or accumulated
678 assemblage). If compositions of Liquid and Minerals are known (matrix **A**), it is possible to estimate, by least
679 squares approximation, their proportion (in matrix **c**). The similarity of **b'** (matrix **c** multiplied with matrix **A**)
680 to **b** (real value) is quantified with the sum of the square of the residuals (Σr^2) as:

$$681 \Sigma r^2 = \Sigma_{i=1}^n (b'_i - b_i)^2 \quad (\text{Eq. 1})$$

682 RFC and Cumulate model results are considered acceptable when $\Sigma r^2 < 1.0$. Proportion of Liquid (Daughter
683 or Melt) is expressed with **F** in matrix **c**.

684 Major-elements mass balance models are calculated in the system SiO₂-TiO₂-Al₂O₃-FeO*-MnO-MgO-CaO-
685 Na₂O-K₂O. The LH5-2 Cpx-bearing basalt, with the lowest SiO₂ and the highest MgO contents, was selected
686 as possible source for all pyroxene-bearing trachyandesites and trachytes. The fractional crystallization
687 hypothesis is then tested for all the LHPCS studied rocks and considering the magmatic mineralogy made of
688 An-rich plagioclase, Ti-rich clinopyroxene, Mg-rich olivine, spinel. The same mineral assemblage was used
689 then to verify the cogenetic relationship between studied LHPCS basalts through progressive crystal
690 accumulation. All calculations were managed with Microsoft Office Excel 2019. Results of FC-models are
691 presented in Supplementary Table 6.

692 The RFC modeling has been applied to all studied trachyandesites and trachytes. It was verified that a
693 fractionation of the Pl+Cpx+Ol+Sp assemblage in the range of: (i) 45-63 wt% (Σr^2 0.37-0.92) is necessary to
694 produce Opx-free trachyandesites, (ii) 59-69 wt% (Σr^2 0.38-0.92) is capable to produce Opx-bearing
695 trachyandesites, and (iii) 73-74 wt% (Σr^2 0.88-0.91) is requested to produce trachytes. The crystal
696 accumulation has been tested to verify the genetic linkage between Cpx-free basalt (LH18-1) and Cpx-
697 bearing basalts (LH5-2, LH27-1). It was verified that a crystal accumulation of the Pl+Cpx+Ol+Sp assemblage
698 in the range of 16-17 wt% (Σr^2 0.05-0.15), with Cpx ranging 5-7 wt%, can produce the LHPCS Cpx-bearing
699 basalts.

700 The results obtained from FC-models thus indicate that the LHPCS volcanic rocks are genetically linked
701 melts, due to crystal accumulation (basalts) and fractional crystallization (intermediate and felsic rocks) of a
702 Pl+Cpx+Ol+Sp mineral assemblage. Trachyandesites and trachytes represent different degrees of
703 fractionation (RFC values in the range 45-74%) starting from a Cpx-bearing basaltic source. Cpx-bearing
704 basalts are interpreted as the result of crystallization and accumulation of Cpx, together with Pl+Ol+Sp, in a
705 pristine Cpx-free basaltic melt. Results from FC-models also confirm the possibility to produce hydrous
706 felsic melts starting from a nominal anhydrous ($H_2O < 1$ wt%; e.g., Webster et al., 1999) mafic parental
707 melt. Integrating FC-model and hygrometer (Putirka, 2008) results, LHPCS trachytes show H_2O ca. 1.4-2.0
708 wt% and represent the ca. 25 wt% fractionated residual melt from a parental basaltic source characterized
709 by H_2O in the range 0.3-0.5 wt%.

710

711 **8.2 Magma evolution beneath Los Humeros**

712 The conceptual model of the present-day LHPCS magmatic plumbing system beneath the Los Humeros
713 caldera is presented in Fig. 12. Based on textural observations, mineral chemistry and thermobaric
714 estimates the early HT (1230-1270 °C) stage of LHPCS magma evolution is represented by high-anorthite
715 plagioclase phenocrysts and Mg-rich olivine ($X_{Fo} = 80-85\%$) crystallizing in the deep (ca. 8 kbar) basaltic
716 reservoir. Where these magmas erupted directly, they formed Cpx-free Ol-basalt lava flows such as the
717 Texcal Lava flow (LH18). This scenario, for LH18 basalt sample, is confirmed by (i) olivine and plagioclase
718 with homogeneous cores and normal monotonous zoning textures at rims, indicating a fast growth during
719 ascent of magma (e.g., Streck, 2008); (ii) olivine with spinifex, dendritic and skeletal textures, interpreted as
720 supercooling mineral texture largely resulting from rapid olivine-supersaturated magma rise from deeper
721 level during the eruption (e.g., Donaldson, 1974; Nakagawa et al., 1998; Fowler et al., 2002; Dahren et al.,
722 2012; Welsch et al., 2013), and (iii) plagioclase specimens with swallow-tailed crystal morphology,
723 interpreted as rapid plagioclase growth due to undercooling related to eruption process (e.g., Renjith,
724 2014).

725 **On the other hand,** a permanence of these basaltic melts in the deep reservoir, together with a
726 temperature decrease of ca. 100 °C can lead to clinopyroxene appearance/crystallization in the system

727 (e.g., Groove, 2000) and its progressive accumulation in the phenocryst assemblage. This hypothesis is
728 supported by Cpx-Liq thermometry models for Cpx1 (Ti-rich augites in basalts) indicating Cpx **appearance** at
729 ca. 7-8 Kbar and 1150 °C (mean values), and by FC-models indicating a Pl+Cpx+Ol+Sp crystal accumulation
730 up to 15-17 wt% in the pristine basaltic melt to produce the Cpx-bearing basalts.

731 Where these magmas erupted as intra-caldera basalts (LH5-2, LH27-1), they are characterized by the
732 further crystallization of (i) progressively Fe-rich olivine (up to $X_{Fo}= 17-20\%$), (ii) Ab-rich plagioclase ($X_{An}= 25-$
733 30%), (iii) Cpx3 unzoned homogeneous phenocrysts and overgrowth (normal monotonous and normal low-
734 amplitude oscillatory **zoning textures**) on Cpx1-cores, (iv) Cpx4 (Di-rich) microcrystals and microlites and (v)
735 Cpx5 (Aeg-Aug) Na-clinopyroxenes. This mineral assemblage (mineral chemistry and textures) together with
736 the obtained thermobarometric results, describes a near-isothermal magma uprising within a narrow
737 temperature window of ca. 1070-1150 °C. Such crystal-bearing magmas ascend from the deeper reservoir
738 to intermediates and shallower stagnation levels, where different phases would crystallize, before the
739 eruption (e.g., Feng and Zhu, 2018). In particular, (i) the homogeneous unzoned cores of phenocrysts
740 represent the early crystallization at equilibrium with the melt, (ii) the normal low-amplitude oscillatory
741 zoning **textures at rims** of Pl and Cpx phenocrysts **indicate** a kinetically driven crystallization (e.g., Ginibre
742 et al., 2002; Streck, 2008; Renjith, 2014), whereas the normal monotonous zoning **textures at rims**
743 observed in many Pl, Cpx and Ol phenocrysts **indicate** a fast growth during ascent of the magma (e.g.,
744 Streck, 2008); (iii) microlites formation indicates water exsolution driven crystallization (e.g., Rutherford,
745 2008; Renjith, 2014) during a relative rapid ascent or eruption processes (e.g. Renjith, 2014); and (iv) the
746 similarity of compositions between Pl and Cpx phenocrysts rims and microlites confirms that there were
747 essentially no major changes in the temperature of any of these basaltic magmas during the ascent (e.g.,
748 Rutherford, 2008). This scenario of rapid ascent of LHPCS basaltic magmas is also supported by the
749 observed high-vesicularity textures, interpreted as bubble-growth processes during a relative fast magma
750 rise precluding exsolved volatile to escape (e.g. Sparks, 1978; Sparks et al., 1998; Rutherford and Gardner,
751 2000; Rutherford, 2008; Costa et al., 2013; Feng and Zhu, 2018).

752 Fractional crystallization of An-rich plagioclase, Fo-rich olivine, Ti-rich augite and spinel (Pl+Ol+Cpx+Sp in
753 RFC-models) in the primary Cpx-bearing basaltic magmas produces residual melts (ca. 30-55 wt%) of
754 trachyandesitic compositions. These evolved buoyant melts will be prone to leave the basaltic reservoir to
755 produce shallower intrusions in a vertically extensive magmatic system (e.g., Jackson et al., 2018), carrying
756 early-formed phenocrysts (i.e., anorthitic plagioclase antecrystals) to the intermediate reservoir and stall.
757 Within this intermediate vertically-distributed layered storage system in the middle crust, Cpx2
758 clinopyroxene and all the rest of plagioclase phenocrysts start to crystallize producing progressively evolved
759 felsic residual melts able to migrate upward in the feeding system or erupt (e.g., Freundt and Schminke,
760 1995; Patanè et al., 2003; Klugel et al., 2005; Stroncik et al., 2009; Aulinas et al., 2010; Dahren et al., 2012;
761 Keiding and Sigmarsson, 2012; Scott et al., 2012; Jeffery et al., 2013; Coombs and Gardner, 2001; Barker et

762 al., 2015; Feng and Zhu, 2018). Similarly to LHPCS basalts, the phenocryst morphologies and textures,
763 together with the microlites compositions and the vesicle-rich textures **described** in trachyandesitic melts,
764 suggest a nearly isothermal rapid ascent precluding exsolved volatiles to escape and producing water
765 exsolution driven crystallization (e.g., Rutherford, 2008; Renjith, 2014).

766 The shallowest magma stagnation level (< 3kbar; mean 1.5 kbar) has been here interpreted as a complex
767 magma plexus constituted by a system of small magma volumes, distributed in locally interconnected
768 pockets and batches. In this plexus mafic and intermediate magmas shortly stall prior to erupt. Whereas
769 more evolved melts reside for a relatively longer time, enough to crystallize orthopyroxene and to enabling
770 the escape of part of the exsolved volatiles (e.g., Sparks et al., 1998; Feng and Zhu, 2018; Clarke et al.,
771 2007), as suggested by phenocryst textures and compositions, and by poor-vesicle textures observed in
772 Opx-trachyte samples (LH5-1, LH6-1).

773 Compositional reverse zoning associated with disequilibrium textures and dissolution/resorption patterns
774 in phenocrysts, are widely considered indicators of both magma-replenishment or assimilation processes
775 (e.g., Wright and Fiske, 1972; Duda and Schminkcke, 1985; Clague et al., 1995; Yang et al., 1999; Klugel et
776 al., 2000; Zhu and Ogasawara, 2004; Stroncik et al., 2009; Ubide et al., 2014; Viccaro et al., 2015; Gernon et
777 al., 2016; Feng and Zhu, 2018). In the case of LHVC, almost all investigated LHPCS samples, from basalts to
778 trachytes, contain mainly phenocrysts with homogeneous cores and low-amplitude oscillatory or normal
779 monotonous zoned rims (Pl+Ol+Cpx) or unzoned homogeneous phenocrysts (as in case of Cpx3 and Opx).
780 Rare specimens not suitable for mineral-liquid thermobarometry, such as plagioclase and clinopyroxene
781 with patchy cores or olivine xenocrysts, are reported. The general absence of disequilibrium textures and
782 **dissolution** patterns in LHPCS studied samples, is therefore interpreted as a lack of evidence of major
783 mixing/recharge and/or assimilation processes acting in the plumbing system (e.g., Cashman et al., 2017
784 and references therein). This hypothesis is in line with the results obtained from tests for mineral-melt
785 equilibria. **Rhodes** diagram (Rhodes et al., 1979; Putirka, 2008) for olivine compositions (Fig. 8a) highlights a
786 progressive decrease in $Mg\#^{liq}$ from basalts to trachytes coupled with general absence of
787 xenocrystals/antecrystals cargo. This behavior is compatible with a complete removal from the melt of
788 previously crystallized Mg-olivine (Roeder and Emslie, 1970; Dungan et al., 1978; Rhodes et al., 1979;
789 Putirka, 2008; Melluso et al., 2014). All LHPCS melts (from basalts to trachytes) invariably show suites of
790 olivines with maximum forsterite (Fo) contents in equilibrium with the respective whole rocks, and vertical
791 trends consistent with closed-system melt differentiation (Roeder and Emslie, 1970; Rhodes et al., 1979;
792 Putirka, 2008; Melluso et al., 2014). Similar behavior is obtained for orthopyroxene (Fig. 8b), where again
793 **Rhodes test** highlights (i) absence of antecrystals, and (ii) Opx-suites progressively and normally Fe-enriched
794 from trachyandesites to trachytes. The absence of clinopyroxene clots and overgrowth mantle textures on
795 orthopyroxene crystals, again excludes the occurrence of magma mixing/recharge processes (Laumonier et
796 al., 2014; Neave et al., 2014; Zhang et al., 2015; Feng and Zhu, 2018). Such interpretation is supported also

797 by field observations, where the interbedded basaltic andesite and trachydacite fall deposits of the ca. 7 ka
798 Cuicuiltic Member show no evidence of magma-mixing (Dávila-Harris and Carrasco-Núñez, 2014).
799 An-Ab partition coefficients (e.g., Putirka, 2008; Jeffery et al., 2013) show a comparable scenario (Fig. 10) in
800 which: (i) the LHPCS basalts are characterized by suites of plagioclases with maximum anorthite (An)
801 contents in equilibrium with the respective whole rocks, and progressive An^{Pl} decrease consistent with
802 closed-system differentiation; and (ii) the progressive decrease in predicted An^{Liq} from basalt to trachyte is
803 compatible with evolved melts differentiation via fractional crystallization. The LHPCS intermediate and
804 evolved products show plagioclase phenocrysts characterized by An-rich homogeneous cores (An 70-85%),
805 with compositions comparable to those of basalts. These An-rich cores can be crystallized in two possible
806 scenarios. The first one is related to the H₂O content in magma. Increasing the water content in melt
807 strongly favors crystallization of An-richer plagioclase. A water content rise from 0.5 to 2.0 wt% could lead
808 to an increase of the An component up to 6-8 mol% (Bindeman and Bailey, 1999; Sano e Yamashita, 2004;
809 Ushioda et al., 2014). In this view, the An-rich plagioclase in intermediate and felsic rocks can be
810 interpreted as the response to the increasing water-content in the fractionated melt. The second scenario
811 implies that An-rich plagioclase taps a more primitive stage of basalt segregations. Since plagioclase
812 phenocrysts with An in the range 65-81% are commonly found in LHPCS basalts, the An-rich plagioclase
813 cores in trachyandesites and trachytes could represent either antecrysts derived from crystallization of
814 early sills in the magmatic reservoir system (sensu Jackson et al., 2018) or crystallization products in an
815 earlier stage of the trachyandesite and trachyte segregation from the basaltic reservoir (e.g., Bindeman and
816 Bailey, 1999; Kinman and Neal, 2006). We suggest that both scenarios concurred to the genesis of An-rich
817 phenocrysts in trachyandesites and trachytes. Noteworthy, when An-rich plagioclase crystals are found (in
818 mafic and intermediate rocks with Pl+Ol+Cpx assemblages), it implies that no significant clinopyroxene
819 crystallization has occurred prior to the anorthitic plagioclase (Bindman and Bailey, 1999).
820 With respect to plagioclase, a similar behavior is observed also for clinopyroxene and in particular for Cpx1
821 and Cpx2 (clinopyroxene cores in basalts and in trachyandesites + trachytes, respectively) populations.
822 Since these mineral cores (Pl, Cpx1 and Cpx2) generally present normal growth rims (i.e., Ab-rich Pl and
823 Cpx3), we suggest that stagnation levels at both intermediate and shallower depths underwent
824 crystallization in a closed system. Otherwise, features such as: i) diffused reverse zoning textures, ii) high-
825 temperature crystal-clots, mantling and overgrowth textures, iii) disequilibrium and dissolution textures
826 (e.g., Stroncik et al., 2009; Cashman et al., 2017; Feng and Zhu, 2018 and references therein), should be
827 widely observed, but this is not the case in the LHPCS studied lavas.

828

829 **8.3 The magma plumbing system**

830 The petrological archive constituted by the LHPCS lavas, spanning from transitional- and alkali-basalts to
831 trachytes, describes the Holocene activity of the LHVC. Harker diagrams for major element bulk

832 compositions of the LHPCS lavas are characterized by linear trends (Fig. 3 b-d) comparable to those
833 expected for cogenetic melts (e.g., Giordano et al., 2012). Major-elements FC-modeling confirms the
834 hypothesis of a common genesis for the LHPCS volcanic rocks through crystal fractionation/accumulation
835 processes of the same mineral assemblage (Pl+Cpx+Ol+Sp). Furthermore, textural observations and results
836 from FC-models permit to exclude mass-change or mass-addition processes driven by AFC-Mixing
837 processes.

838 Results obtained from the application of different and independent thermobarometry models (Fig. 11)
839 confirm the working hypothesis of a complex magmatic plumbing system rather than a single “standard”
840 magma chamber (e.g., Keiding and Sigmarsson, 2012; Cashman and Giordano, 2014; Cashman et al., 2017;
841 Feng and Zhu, 2018) developed beneath the active Los Humeros caldera and feeding the LHPCS volcanism.

842 With the aim to propose an updated and realistic conceptual model of the present-day main storage zones
843 and magma plumbing system within the crust below Los Humeros caldera, we integrate pressure-
844 temperature estimates acquired in this study with the existing data related to the crustal structure and
845 corresponding physical parameters of the study area. The resulted model is shown in Figure 12.

846 The density of TMVB crust shows a large range between 1800 kg/m³ for unconsolidated sediments to about
847 3000 kg/m³ for the lower crust and 3300 kg/m³ for the upper mantle (Dziewonski and Anderson, 1981;
848 Campos-Enríquez and Sánchez-Zamora, 2000; Davies, 2013). The available compilation of crustal data for
849 LHVC is recovered by the measure N°10 of the Crust 1.0 global model (Dziewonski and Anderson, 1981;
850 Davies, 2013). The measure N°10 (yellow star in Fig. 1) is located within the study area at the southern
851 termination of the Tepeyahualco Lava Flow and describes a crust made of five main seismic layers (Fig. 12):
852 (i) upper sediments (thickness: 1 km, density 2110 kg/m³); (ii) middle sediments (thickness: 0.5 km, density
853 2370 kg/m³); (iii) upper crust (thickness: 13.6 km, density 2740 kg/m³); (iv) middle crust (thickness: 15.3 km,
854 density 2830 kg/m³); and (v) lower crust (thickness: 13.6 km, density 2920 kg/m³). Inferred (seismic) Moho
855 depth is reported at -41.7 km with an upper mantle density of 3310 kg/m³ (Dziewonski and Anderson,
856 1981; Davies, 2013). Here we use a five-tiered density model as derived from the Crust 1.0 global model to
857 convert obtained pressure estimates to crustal depths below LHVC.

858 The thermobarometry models applied to the LHPCS lavas define a broad region of crystallization between
859 ca. 0 and 30 km in depth that can be described with a quadrimodal distribution of pressure values (Fig. 12).

860 This allows us to propose a complex polybaric continuous heterogenous multilayered transport and storage
861 magmatic system.

862 A deep-seated anhydrous Ol-basalt reservoir at depths of ca. 28-33 km (7.6-9.2 kbar), at the boundary
863 between lower and middle crust, below the caldera is recorded by (i) An-rich Pl cores (X_{An} = 50-70 %), and
864 (ii) Ti-rich augitic Cpx₁ cores (Mg# up to 75, TiO₂ up to 4.57 wt%). For this mafic reservoir, the overlapping
865 of the calculated anhydrous temperature estimates as derived from Pl-Liq, Cpx₁-Liq and Ol-Liq pairs spans
866 ca. 1000 – 1300 °C. The highest anhydrous temperature values are derived from the Cpx-free Ol-basalt

867 Texcal lava flow (LH18), where the convergence of Pl-Liq thermobarometry and Ol-Liq thermometry models
868 indicate conditions of T ca. 1230-1270 °C at P ca. 8 kbar. Lower anhydrous temperatures of ca. 1000-1210
869 °C are obtained at a comparable average pressure values for Cpx-bearing intra caldera Ol-basalts (LH5-2; LH
870 27-1). These results are in agreement with existing literature on the near-liquidus melting behavior of high-
871 Al basaltic magmas (Mg# ca. 60-70 and Al_2O_3 : 17-19 wt%) under dry conditions (e.g., Thompson, 1974;
872 Grove et al., 1982; Crawford et al., 1987; Bartels et al., 1991; Grove, 2000). At 1250-1300 °C and ca. 10 kbar
873 (Point A in Fig. 11) the basaltic melt is in equilibrium with a mantle peridotite mineral assemblage of olivine
874 + clinopyroxene (Kushiro and Yoder, 1966; Presnall et al., 1978; Grove et al., 1982; Fuji and Scarfe, 1985;
875 Takahashi, 1986; Fallon and Green, 1987; Bartels et al., 1991; Sisson and Layne, 1993; Wagner et al., 1995;
876 Grove et al., 1997; Grove, 2000; Kinzler et al., 2000). Following the models proposed by Thompson (1974),
877 Bartels et al. (1991) and Grove (2000), a temperature decrease would lead primary melts to pass the “dry
878 basaltic liquidus” and start the crystallization of Ol+Pl (higher temperatures) or Ol+Cpx+Pl (lower
879 temperatures) assemblages (see stability fields in Fig. 11). Given the ubiquitous presence in all LHPCS
880 basalts of well-developed euhedral to subhedral olivine crystals (both as phenocrysts and microlites) at
881 equilibrium with anorthitic plagioclase, it is possible to exclude that crystallization history started at depth >
882 ca. 10-12 kbar where olivine is not a stable phase and the primary assemblage would be characterized only
883 by Cpx+Pl+Sp in equilibrium with melt (Kushiro and Yoder, 1966; Thompson, 1974; Presnall et al., 1978;
884 Bartels et al., 1991; Grove, 2000).

885 **A second magma transport and storage system** can be recognized at depths of 15-30 km (ca. 4.5 – 7.8
886 kbar), in continuity with the deeper basaltic reservoir and distributed along the whole middle crust
887 thickness, as recorded by the wide range of pressure estimates obtained from plagioclase (X_{An} = 40-70%)
888 and Cpx2 clinopyroxene cores (Mg# 59-84; TiO_2 mean value 0.99 wt%). Thermometry models based on
889 plagioclase, Cpx2 clinopyroxene and olivine show convergence for hydrous temperature values in the range
890 of 979 – 1263 °C. Thermobarometry models, together with textures and petrographic relations in all
891 analyzed trachyandesite and trachyte samples suggest that all plagioclase, all Cpx2 clinopyroxene
892 phenocrysts, and part of microlites grew in this second storage system. In particular, it is possible to
893 observe two main crystallization temperature conditions: (i) at ca. 1190 °C (weighted mean value, MSWD=
894 2.2, n= 205) plagioclase phenocrysts crystallization in trachyandesite melts is observed, whereas (i) at the
895 lower temperature of ca. 1070 °C (weighted mean value, MSWD= 1.7, n= 155) is reported the crystallization
896 of all olivine, all Cpx2 phenocrysts, and plagioclase phenocrysts in trachytes. We interpret the common
897 Pl+Cpx2 phenocryst-forming barometric conditions as the evidence of a growth-dominated regime within
898 this second magma storage zone (e.g., Barclay et al., 1998; Humphreys et al., 2006; Scott et al., 2012).

899 **Whereas** the smaller crystals (microcrystals and microlites) represent the nucleation-dominated regime
900 (Scott et al., 2012) that can be associated with ascent-related decompression of melts at shallower levels
901 (e.g., Cashman, 1992; Cashman and Blundy, 2000; Humphreys et al., 2009).

902 The third melt storage zone occurs at shallower depths of ca. 10-15 km, possibly corresponding to the
903 transition between middle- and upper-crust, as indicated by convergence of barometric estimates
904 (weighted mean value of 3.9 ± 0.2 kbar ($\pm 1\sigma$), MSWD= 0.80, n= 203; P ranging ca. 1-7 kbar) obtained from
905 Cpx3 clinopyroxene (i.e., unzoned phenocrysts and overgrowth/rims around earlier formed Cpx1- and
906 Cpx2-cores) population. For this third storage zone, the Cpx3-Liq thermometry model indicates a mean
907 temperature of 1040 °C (weighted mean value, MSWD= 2.6, n= 203; T ranging ca. 940-1210 °C),
908 comparable to those calculated for Ol+Cpx2 assemblages in the previous described second and deeper
909 stagnation system. The obtained pressure estimates for the second and the third storage systems are
910 compatible with multiple magma storage pockets in which melts of comparable compositions ascend
911 slowly enough for phenocrysts to form (e.g. Scott et al., 2012), and start cooling before the final ascent to
912 shallower conditions (e.g., Dahren et al., 2012; Chadwick et al., 2013; Gardner et al., 2013; Jeffery et al.,
913 2013; Preece et al., 2013; Troll et al., 2013). Taking into account the textures and the chemistry of Cpx3
914 clinopyroxene phenocrysts, the obtained thermobarometric estimates could be interpreted as the
915 pressure-temperature environment of last major levels of magma stagnation and fractionation (Putirka,
916 1997; Klugel et al., 2005; Galipp et al., 2006; Stroncik et al., 2009).

917 The fourth shallowest storage zone located at depths of ca. 3-7 km (weighted mean value of 1.5 ± 0.2 kbar
918 ($\pm 1\sigma$), MSWD= 0.24, n= 177; P ranging ca. 0.1-4.5 kbar), is required to explain the presence of (i) Cpx4
919 clinopyroxene (microcrystals and microlites) in all LHPCS lavas, and (ii) Aeg-rich Cpx5 clinopyroxene in
920 basalts, and (iii) Fe-olivine (Fo = 55-65%) and orthopyroxene in Opx-bearing evolved LHPCS lavas. Magmas in
921 this shallow storage system show a wide range of temperature values calculated for hydrous melts: (i) ca.
922 1060 °C (weighted mean value, MSWD= 2.4, n= 7) for Aeg-rich Cpx5 crystallization in basalts; (ii) ca. 1070 °C
923 (weighted mean value, MSWD= 1.09, n= 168) for Cpx4 and Opx crystallization in trachyandesites; and (iii)
924 ca. 965 °C (weighted mean value, MSWD= 2.2, n= 78) for olivine, Cpx4 and Opx crystallization in trachytes.
925 Thermobaric estimates obtained for Aeg-rich Cpx5 agree with those calculated for transitional basalts at
926 Pantelleria (White et al., 2009 and references therein), whereas orthopyroxene crystallization conditions
927 overlap with the existing literature for intermediate rocks (e.g., Rutherford et al., 1985; Wallace and
928 Anderson, 2000; Reubi and Nicholls, 2004; Allan et al., 2013; Jeffery et al., 2013). The broad distribution of
929 melt chemistry from basalt to trachyte, together with the obtained thermobaric estimates, defines a
930 shallow magma storage environment characterized by progressive accumulation of small locally
931 interconnected magma pockets and batches (e.g., Reubi and Nicholls, 2004; Jeffery et al., 2013) dispersed
932 in the upper crust (<10 km) with a possible magma plexus at a depth of 2-4 km under the caldera (e.g.,
933 Armienti et al., 1989; Freundt and Schminke, 1995; Pietruszka and Garcia, 1999; Patanè et al., 2003; Klugel
934 et al., 2005; Stroncik et al., 2009; Dahren et al., 2012; Jeffery et al., 2013; Coombs and Gardner,, 2001,
935 2004).

936

937 **8.4 “Standard” versus multilayered magmatic plumbing system**

938 Existing conceptual models for LHVC are based on the “Standard Model” (*sensu* Gualda and Ghiorso, 2013),
939 considering a single, bowl-shaped and long-lived, melt-dominated magma chamber of 1000-1500 km³, at
940 depth of 5 to 10 km (Verma, 1983, 1984, 1985a, 1985b; Verma and Lopez, 1982; Verma et al., 1990; Verma
941 and Andaverde, 1995; Verma et al., 2011; Verma et al. 2013; Carrasco-Núñez et al., 2018). However, these
942 models mainly refer to the Los Humeros Caldera stage activity (Carrasco-Núñez et al., 2018 and references
943 therein), lasted ca. 130 ky, where the major caldera-forming events (Xaltipan and Zaragoza ignimbrites, 115
944 km³ and 15 km³ DRE, respectively) and the large Plinian eruptive episode (Faby Tuff, 10 km³ DRE)
945 necessitated feeding from a huge, voluminous magma chamber (Carrasco-Núñez and Branney, 2005;
946 Carrasco-Núñez et al., 2018).

947 On the other hand, the Holocene eruptive phase of the LHPCS **is characterized by a** bimodal volcanism
948 (Carrasco- Núñez et al., 2017a; Carrasco-Núñez et al., 2017b; Carrasco-Núñez et al., 2018), typified by
949 alternating episodes of effusive and explosive **activity** with a **wide compositional range of volcanic products**,
950 spanning from basaltic to trachytic lava flows and mafic to felsic pumice and scoria fall deposits, erupted by
951 tens of **monogenetic centers** located in the LHVC (e.g., Norini et al., 2015; Carrasco- Núñez et al., 2017a;
952 Carrasco-Núñez et al., 2017b; Carrasco-Núñez et al., 2018). **The LHPCS** volcanic activity is characterized by
953 spatially distributed, small volumes of erupted material (ca. 6 km³ of mafic lavas, 10 km³ of intermediate
954 and felsic lava, and 1 km³ of mafic and felsic tephra; Carrasco-Núñez and Branney, 2005). Furthermore, key
955 elements, such as the lithic-free character of the LHPCS volcanic products, their overall textures and
956 chemistry of the constituent mineral assemblages, coupled with the results from RFC-models, suggest that
957 LHPCS magmatism is characterized by batches of magma evolving in a nearly closed system, unaffected by
958 magmatic assimilation and mixing/recharge processes. In particular, the almost complete lack of magma
959 mixing/recharge events (e.g., Lee et al., 2014) is confirmed by the absence of the typical expected **mineral**
960 textures (e.g., Streck, 2008; Renjith, 2014) such as: (i) fine-sieve textures and resorption surfaces due to
961 reaction with a more primitive magma; (ii) glomerocryst-forming due to the recrystallization/suturing at rim
962 of resorbed crystals; (iii) reverse zoning **textures** due to compositional inversion in open/recharged system;
963 and (iv) reaction rims, breakdown mantles and crystal clots due to the disequilibrium-triggered
964 recrystallization into a new set of minerals.

965 The existing literature focused on magma recharge processes (e.g., De Paolo, 1981; Hofmann, 2012; O’Neill
966 and Jenner, 2012; Lee et al., 2014) highlights that a high evacuation/eruption efficiency would shorten the
967 residence-time of magma in the storage chamber and would reduce the effect of crystallization in
968 modifying the magma composition (Lee et al., 2014). Moreover, in case of eruption/evacuation rates higher
969 than the recharge rates (e.g., Lee et al., 2014), it is possible to hypothesize a magmatic system dominated
970 by ephemeral, closed-system magma batches not affected by major mixing processes prior **to** their
971 evacuation/eruption (e.g., De Paolo, 1981; Hofmann, 2012; O’Neill and Jenner, 2012; Lee et al., 2014). This

972 scenario best approximates the characteristics observed for all the Holocene LHPCS magmatic products. In
973 addition, the lack of liquid-dominated zone(s) (e.g., Bachmann and Bergantz, 2008), where mixing could
974 occur (e.g., Cashman and Giordano, 2014), suggests that the remnants of the huge magma chamber of the
975 LH caldera stage are now completely solidified and crosscut by the uprising LHPCS mafic and felsic magmas.
976 This scenario is also coherent with the post-caldera eruption behavior observed in other volcanic
977 complexes, such Ischia (e.g., Casalini et al., 2017), and it is consistent with the recent literature proposing
978 complex magma chamber reservoirs made up of multiple discrete melt pockets with no mass-exchange and
979 reactivated shortly before eruption (e.g., Cashman and Giordano, 2014; Cashman et al., 2017; Casalini et
980 al., 2017).

981 Thermobarometric estimates obtained in this study, combined with the existing literature and integrated
982 with information from the crustal structure beneath Los Humeros caldera, therefore permit us to discard
983 the “standard model” of the huge voluminous chamber in favor of a more feasible conceptual model
984 characterized by a polybaric magmatic plumbing system made up of multiple, more or less interconnected
985 magma transport and storage layers, i.e. transient batches and ponds of different magmas, localized
986 beneath Los Humeros nested caldera and feeding the Holocene activity of the LHVC. In particular, our
987 results indicate that magma transport and storage levels beneath Los Humeros caldera are vertically
988 distributed across the whole crust from ca. 30 to 3 km (from the lower- to the very upper-crust) with
989 density contrasts between the different crustal layers acting as a controlling parameter for ascending or
990 stalling magmas (e.g., Dahren et al., 2012), reflecting the buoyant magma compositions and the melt
991 fractions (e.g., Cashman et al., 2017; Jackson et al., 2018). Moreover, it is possible to propose that each of
992 these crust/density boundaries have determined lateral transport and grow of magma stagnation pockets
993 (e.g., Dahren et al., 2012; Jackson et al., 2018). At depths < 5 km, buoyant magmas and fractionated melts
994 (from mafic to felsic) ascending from all the lower storage zones are stalled once more. The shallowest
995 complex multi-storage system is interpreted as a plexus of scattered, more or less interconnected,
996 ephemeral small-volume batches and pockets of melts, without any defined spatial distribution, as
997 confirmed by field-locations of the LHPCS studied lavas eruptive centers.

998 A shallow storage zone presenting magmas with heterogenous compositions (from mafic to felsic) has been
999 already proposed by Dávila-Harris and Carrasco-Núñez (2014) to explain the eruptive history of the intra-
1000 caldera Cuicuiltic Member that was produced by the coeval eruption of mafic and felsic unmixed magmas.
1001 However, a shallow ponding system characterized by heterogeneous composition of magmas involved
1002 beneath Los Humeros caldera is not an exceptional case. Examples of shallow heterogeneous reservoirs
1003 beneath active volcanic complexes are widely reported (e.g., Nairn et al., 1998; Kratzmann et al., 2009;
1004 Sigmarsson et al., 2011; Keiding and Sigmarsson, 2012).

1005 Our results also agree with the work of Creon et al. (2018), where calculated fluid saturation depths derived
1006 for melt inclusions in post-caldera lavas indicate different magma-ponding levels within a range of depths

1007 between 5 and 13 km, together with a possible deeper reservoir (26-32 km) and a final shallow stagnation
1008 level at ca. 1.5-3.0 km.

1009

1010 **8.5 Implications for the active geothermal system**

1011 The geothermal activity of a volcanic complex is expected to be the result of stagnation and cooling of
1012 magmas in the shallower storage zone (e.g., Gunnarsson and Aradóttir, 2015), where classic conductive
1013 models are adopted to model the heat source, mainly controlled by age and volume of the magmatic
1014 system (Smith and Shaw, 1975; Cathles et al., 1997; Duffield and Sass, 2003; Gunnarsson and Aradóttir,
1015 2015; Carrasco-Núñez et al., 2018). As widely demonstrated (e.g., Smith and Shaw, 1975; Cathles et al.,
1016 1997), a very large intrusion would produce a long-lived hydrothermal/geothermal system. Many numerical
1017 models (e.g., Cathles et al., 1997) suggest that, in the most favorable conditions, a voluminous (>2000 km³)
1018 intrusion/chamber of mafic melt could be able to sustain a convective geothermal system up to 800 Ky. On
1019 the other hand, very small mafic sills and **dikes** intrusions (<10 km³) would produce very localized thermal
1020 anomalies and could cool down to the solidus temperature in less than 0.1 ky (Nabelek et al., 2012), and
1021 definitively cool in ca. 1 ky (e.g. Cathles et al., 1997). Convection due to hydrothermal fluid circulation,
1022 increases the cooling rate of a magmatic intrusion (Cathles et al., 1997).

1023 The present geothermal activity of LHVC is characterized by a limited NNW-SSE non-homogeneous areal
1024 distribution within the Los Potreros nested caldera (e.g., Norini et al., 2015; Urbani et al., 2019). Based on
1025 (i) the young age (Upper Pleistocene-Holocene) of most of the LHPCS volcanic activity; (ii) the relatively
1026 small erupted volumes of the LHPCS lavas, in particular of those erupted within the Los Potreros caldera;
1027 and (iii) the existence of a shallower magmatic plexus characterized by heterogeneous unmixed magmas
1028 (this study), we therefore discard the hypothesis of a single, large and voluminous shallow magmatic
1029 chamber homogeneously distributed beneath the caldera, in favor of a more feasible scenario characterized
1030 by an upper crustal plexus made of small, single-charge ephemeral pockets of different magmas localized
1031 beneath Los Humeros nested caldera, very close or within the Los Humeros exploited geothermal field. In
1032 this scenario, every LHPCS magma pocket and cryptodome within the Los Humeros caldera (see Urbani et
1033 al., 2019) could be interpreted as a scattered and localized short-lived (ca. 0.1-1 ky; Cathles et al., 1997)
1034 heat source, whereas the cooling and solidified remnants of the huge magma chamber of the caldera stage
1035 could still represent a background positive thermal anomaly affecting the volcanic field.

1036 Our reconstruction of the Los Humeros heat source therefore suggests the possible existence of a wide
1037 background positive thermal anomaly associated to the cooling solidified remnants of the voluminous
1038 magma chamber of the caldera stage, with juxtaposition of scattered high-frequency heat sources related
1039 to the very shallow intrusive complex that make-up the surficial (upper crustal) plexus of the LHPCS
1040 magmatic plumbing system.

1041 In the light of our results, a revision/update of the heat source feeding the Los Humeros geothermal system
1042 is needed to produce correct and up-to-date geothermal potential estimates of the geothermal field and to
1043 develop efficient geothermal exploration and exploitation strategies.

1044

1045 **9. CONCLUSIONS**

1046 In this study we propose an integrated field-based petrographic-mineralogical approach to unravel the
1047 evolution and configuration of the present-day magmatic plumbing system feeding the post-caldera stage
1048 activity of LHVC. The main results of this study can be summarized as follows:

1049 (i) The Rayleigh fractional crystallization (RFC) models demonstrate that all LHPCS magmas, from
1050 basalts to trachytes, belong to the same line of descent and evolve through a progressive
1051 fractionation of the Pl+Cpx+Ol+Sp mineral assemblage.

1052 (ii) A complex polybaric magmatic transport and storage system, characterized by multiple magma
1053 levels more or less interconnected in space and time, has been recognized based on application of
1054 mineral-melt thermobarometry models.

1055 (iii) A deep mafic reservoir (at ca. 30 km depth) is identified by the Pl+Ol assemblage in basalts.
1056 Intermediate magma storage systems (in the whole middle crust) are described by the composition
1057 of the Cpx phenocrysts, whereas a shallow magmatic stagnation system (ca. 1.5 kbar; 3-5 km
1058 depth) is defined by crystallization of Cpx microlites (aegirine clinopyroxenes in basalt) and, in
1059 particular, by Opx growth in most evolved melts. All the Cpx-bearing lavas are produced by
1060 progressive differentiation via polybaric fractional crystallization during magma ascent through the
1061 plumbing system.

1062 (iv) The chemical composition of the main phases (Ol, Pl, Cpx, Opx), together with results from FC-
1063 modelling, do not support a magmatic feeding system dominated by magma mixing and magma
1064 replenishment. They are instead compatible with a plumbing system dominated by discrete levels,
1065 pockets and batches of melts.

1066 (v) The thermobarometric results **indicate the** configuration of the magmatic plumbing system is
1067 vertically extensive across the entire crust, **with a deeper residence zone for basalts at ca. 8 kbar**
1068 **(ca. 30-33 km depth). A complex zone, from middle (6-4 kbar) to upper crust (0.5 kbar) depths,**
1069 **where rapidly ascending basalts stall before their eruption, is proposed. This complex zone also**
1070 **corresponds to depths where smaller batches of mafic magmas, at times interconnected with the**
1071 **lower feeding zone, differentiate to trachyandesites and trachytes.**

1072 (vi) The main outcome for the modeling of the magmatic heat source of the LHVC geothermal system is
1073 the inadequacy of conservative conceptual models based on the classical melt-dominated, single,
1074 long-lived and voluminous magma chamber (i.e., "Standard Model"), in favor of an innovative and
1075 more realistic vision of the magmatic plumbing **system** made of multiple, more or less

1076 interconnected, magma transport and storage layers within the crust, feeding small (ephemeral)
1077 magma pockets at shallow-crust conditions.

1078 (vii) The proposed model for the magmatic plumbing system at LHVC provides a new configuration of
1079 the heat source feeding the present geothermal reservoir that must be taken into account for
1080 geothermal exploration and exploitation purposes.

1081

1082 **APPENDIX A: Analytical details**

1083 **A.1 Petrography of volcanic samples**

1084 Rock magmatic fabrics, textures and mineral assemblages were studied on polished thin sections, using a
1085 Nikon Eclipse 50iPol polarized light microscope (PLM) equipped with Nikon Ds-Fi2 CCD camera (Nikon,
1086 Tokyo, Japan) and Nikon Nis-Elements software (Ver4.30.01), at Laboratorio di Microtettonica, Dip. Science,
1087 Università Roma Tre (Roma, Italia). Mineral abbreviations follow Whitney and Evans (2010).

1088

1089 **A.2 Bulk major element geochemistry**

1090 After washing in distilled water, samples were grounded in an agate mill, pre-contaminated with an aliquot
1091 of sample. Whole-rock major element concentrations (4 samples) were measured at the Activation
1092 Laboratories (Ontario, Canada), through ion coupled plasma (ICP)- optical emission (OE). For major
1093 elements the uncertainty (1σ) is estimated better than 2% for values higher than 5 wt %, and better than
1094 5% in the range 0.1-5 wt %. Additional samples (9) were analyzed by X-ray fluorescence (XRF) using a ZSX
1095 Primus II (Rigaku Co., Japan) at Nagoya University, Japan. Loss on ignition (LOI) was measured from the
1096 sample powder weight in a quartz glass beaker in the oven at 950°C for five hours. XRF-analyses were
1097 carried out following the procedure presented in Azizi et al., (2015; 2018a; 2018b). For major elements the
1098 uncertainty (1σ) is estimated better than 1% for values higher than 10 wt %, and better than 5% in the
1099 range 0.1-10 wt %.

1100

1101 **A.3 Mineral chemistry**

1102 Polished thin sections (13 samples) selected for petrography investigations, were then studied for mineral
1103 chemistry and ca. 2400 analyses of mineral phases were obtained with a Cameca SX100 electron
1104 microprobe (EMP) at the Institut für Anorganische Chemie, Universität Stuttgart.

1105 Operating conditions were 15 kV and 10 to 15 nA, counting times of 20 s both for peak and background.
1106 Spot sizes were 1-10 μm depending on the phases analyzed. Compositions were determined relative to
1107 natural and synthetic standards.

1108 A set of reference materials (i.e., natural and synthetic oxides, and minerals) was used for routine
1109 calibration and instrument stability monitoring. In particular we used: (i) Si, Ca: natural wollastonite (P&H
1110 Developments); (ii) Si, Fe: natural fayalite USNM 85276 (Jarosewich et al., 1980); (iii) K: natural orthoclase
1111 (P&H Developments); (iv) Na: natural pure albite from Crete (Greece); (v) Al: synthetic corundum (P&H
1112 Developments); (vi) Mg: synthetic periclase (P&H Developments); (vii) Mn: natural rhodonite (P&H
1113 Developments); (viii) Ti: synthetic rutile (P&H Developments); (ix) Cr: synthetic chromium oxide (P&H
1114 Developments). Repeated analyses of the standards (Supplementary Table 7) resulted in one-sigma (1σ)
1115 standard deviations close to the ones calculated from counting statistics. For the major minerals, calculated
1116 1σ (%) precisions are (i) better than 1.5 % for Si; (ii) better than 2% for Al; (iii) 1 to 5% for Ca, Mg, Fe, Mn, Ti

1117 and Cr, applying the above-mentioned applied conditions. For Na and K, calculated 1σ (%) precisions are
1118 below 5% for analyses of feldspars and Aeg-rich clinopyroxene. The 1σ accuracy is estimated to be up to
1119 three times larger than the precision because additional effects such as uncertainty of the mass absorption
1120 coefficients that are used for the matrix correction of the microprobe raw data or instability of the beam
1121 may play a role.

1122 Validation of mineral chemistry results were also achieved through opportune comparisons with the
1123 existing literature for (i) Mg-olivine (e.g., Hirano et al., 2004; White et al., 2009; Giordano et al., 2012;
1124 Melluso et al., 2014); (ii) Fe-olivine (e.g., Aldanmaz, 2006; White et al., 2009; Melluso et al., 2010; Giordano
1125 et al., 2012); (iii) aegirine-augite clinopyroxene (Cpx5 group; e.g., Piilonen et al., 1998; White et al., 2009;
1126 Njonfang et al., 2013); (iv) augite-diopside clinopyroxene (Cpx1-4 groups; e.g., Dawson and Hill, 1998;
1127 Aldanmaz, 2006; Melluso et al., 2010, 2014); (v) orthopyroxene (e.g., Papike et al., 1995; Aldanmaz, 2006;
1128 Carvalho and de Assis Janasi, 2012; Hu et al., 2018); (vi) feldspar (e.g., Keil et al., 1972; Giordano et al.,
1129 2012; Innocenti et al., 2013; Njonfang et al., 2013); and (vii) spinel and opaque minerals (e.g., Melluso et al.,
1130 2014). Back Scattered Electron (BSE) imaging was obtained by using the same electron microprobe with
1131 operating conditions of 15 kV, 50 nA. Mineral structural formulae of feldspar, olivine and spinel were
1132 calculated through the software CalcMin_32 (Brandelik, 2009). Mineral structural formulae of
1133 orthopyroxene were calculated following Putirka et al. (1996) and Putirka (2008). Clinopyroxene formula
1134 has been calculated following procedures reported in Putirka et al. (1996), Putirka (2008), Masotta et al.
1135 (2013). Clinopyroxenes were then classified integrating the Wo-En-Fs scheme (Morimoto, 1989) and J vs. Q
1136 scheme (Morimoto, 1988, 1989) with $J = 2\text{Na apfu}$ and $Q = (\text{Ca} + \text{Mg} + \text{Fe}^{2+}) \text{ apfu}$. Aegirine (X_{Aeg}) component
1137 correction, for Na-rich Cpx (Aegirine-Augite series), followed the scheme ($X_{\text{Aeg}} = \text{Na apfu}$ if $\text{Na} < \text{Fe}^{3+ \text{ Tot}}$, $X_{\text{Aeg}} =$
1138 $\text{Fe}^{3+ \text{ Tot}}$ apfu if $\text{Na} > \text{Fe}^{3+ \text{ Tot}}$) proposed by Putirka et al. (1996), Putirka (2008) and based on $\text{Fe}^{2+} - \text{Fe}^{3+}$
1139 correction of Lindsley (1983).

1140

1141 **ACKNOWLEDGMENTS**

1142 The authors are grateful to the Editor (Dr. C.J. Lissenberg), to Dr. C.M. Petrone and to an anonymous
1143 reviewer for their helpful and constructive comments that deeply contributed to improve the manuscript.
1144 The authors wish to thank the Comisión Federal de Electricidad (CFE, Mexico) for their assistance and
1145 support. This paper presents results of the GEMex Project, funded by the European Union's Horizon 2020
1146 programme for Research and Innovation under grant agreement No. 727550 (scientific responsibility Guido
1147 Giordano), and by the Mexican Energy Sustainability Fund CONACYT-SENER, Project 2015-04-268074 (WP
1148 4.5, scientific responsibility Gerardo Carrasco-Núñez). More information can be found on the GEMex
1149 Website: <http://www.gemex-h2020.eu>.

1150 Authors would like to thank G. Norini for usefull discussions in the field. Special thanks to Javier Hernández,
1151 Jaime Cavazos, Francisco Fernández and Alessandra Pensa for their support in the fieldwork and logistics.

1152 The Grant to Department of Science, Roma Tre University (MIUR-Italy Dipartimenti di Eccellenza, ARTICOLO
1153 1, COMMI 314-337 LEGGE 232/2016) is gratefully acknowledged.

1154

1155

1156 **REFERENCES**

- 1157 Aldanmaz, E.: Mineral-chemical constraints on the Miocene calc-alkaline and shoshonitic volcanic rocks of
1158 western Turkey: disequilibrium phenocryst assemblages as indicators of magma storage and mixing
1159 conditions. *Turkish J. Earth Sci.*, 15(1), 47-73, 2006.
1160
- 1161 Allan, A. S., Morgan, D. J., Wilson, C. J., and Millet, M. A.: From mush to eruption in centuries: assembly of
1162 the super-sized Oruanui magma body. *Contrib. Mineral. Petr.*, 166, 143-164, 2013.
1163
- 1164 Annen, C.: From plutons to magma chambers: Thermal constraints on the accumulation of eruptible silicic
1165 magma in the upper crust. *Earth Planet. Sc. Lett.*, 284, 409-416, 2009.
1166
- 1167 Armienti, P., Innocenti, F., Petrinì, R., Pompilio, M., and Villari, L.: Petrology and Sr-Nd isotope geochemistry
1168 of recent lavas from Mt. Etna: bearing on the volcano feeding system. *J. Volcanol. Geoth. Res.*, 39,
1169 315-327, 1989.
1170
- 1171 Arndt, N. T., and Jenner, G. A.: Crustally contaminated komatiites and basalts from Kambalda, Western
1172 Australia. *Chem. Geol.*, 56, 229-255, 1986.
1173
- 1174 Aulinas, M., Gimeno, D., Fernandez-Turiel, J. L., Perez-Torrado, F. J., Rodriguez-Gonzalez, A., and Gasperini,
1175 D.: The Plio-Quaternary magmatic feeding system beneath Gran Canaria (Canary Islands, Spain):
1176 constraints from thermobarometric studies. *J. Geol. Soc. London*, 167, 785-801, 2010.
1177
- 1178 Azizi, H., Najari, M., Asahara, Y., Catlos, E. J., Shimizu, M., and Yamamoto, K.: U–Pb zircon ages and
1179 geochemistry of Kangareh and Taghiabad mafic bodies in northern Sanandaj–Sirjan Zone, Iran:
1180 Evidence for intra-oceanic arc and back-arc tectonic regime in Late Jurassic. *Tectonophysics*, 660,
1181 47-64, 2015.
1182
- 1183 Azizi, H., Lucci, F., Stern, R. J., Hasannejad, S., and Asahara, Y.: The Late Jurassic Panjeh submarine volcano
1184 in the northern Sanandaj-Sirjan Zone, northwest Iran: Mantle plume or active margin? *Lithos*, 308,
1185 364-380, 2018a.
1186
- 1187 Azizi, H., Nouri, F., Stern, R. J., Azizi, M., Lucci, F., Asahara, Y., Zarinkoub, M. H., and Chung, S. L.: New
1188 evidence for Jurassic continental rifting in the northern Sanandaj Sirjan Zone, western Iran: the
1189 Ghalaylan seamount, southwest Ghorveh. *Int. Geol. Rev.*, DOI: 10.1080/00206814.2018.1535913,
1190 2018b.
1191
- 1192 Bachmann, O., and Bergantz, G.W.: On the origin of crystal-poor rhyolites: extracted from batholithic
1193 crystal mushes, *J. Petrol.*, 45, 1565-1582, 2004.
1194
- 1195 Bachmann, O., and Bergantz, G.W.: Rhyolites and their source mushes across tectonic settings, *J. Petrol.*,
1196 49, 2277-2285, 2008.
1197
- 1198 Barberi, F., Ferrara, G., Santacroce, R., Treuil, M., and Varet, J.: A transitional basalt-pantellerite sequence
1199 of fractional crystallization, the Boina Centre (Afar Rift, Ethiopia), *J. Petrol.*, 16(1), 22-56, 1975.
1200
- 1201 Barclay, J., Rutherford, M. J., Carroll, M. R., Murphy, M. D., Devine, J. D., Gardner, J., and Sparks, R. S. J.:
1202 Experimental phase equilibria constraints on pre-eruptive storage conditions of the Soufrière Hills
1203 magma. *Geophys. Res. Lett.*, 25, 3437-3440, 1998.
1204
- 1205 Barker, A. K., Troll, V. R., Carracedo, J. C., and Nicholls, P. A.: The magma plumbing system for the 1971
1206 Teneguía eruption on La Palma, Canary Islands. *Contrib. Mineral. Petr.*, 170, 54, 2015.
1207

1208 Bartels, K. S., Kinzler, R. J., and Grove, T. L.: High pressure phase relations of primitive high-alumina basalts
1209 from Medicine Lake volcano, northern California. *Contrib. Mineral. Petr.*, 108, 253-270, 1991.
1210
1211 Beattie, P.: Olivine-melt and orthopyroxene-melt equilibria. *Contrib. Mineral. Petr.*, 115, 103-111, 1993.
1212
1213 Bégué, F., Deering, C. D., Gravley, D. M., Kennedy, B. M., Chambefort, I., Gualda, G. A. R., and Bachmann,
1214 O.: Extraction, storage and eruption of multiple isolated magma batches in the paired Mamaku and
1215 Ohakuri eruption, Taupo Volcanic Zone, New Zealand. *J. Petrol.*, 55, 1653-1684, 2014.
1216
1217 Bellieni, G., Justin Visentin, E., Le Maitre, R. W., Piccirillo, E., and Mand Zanettin, B.: Proposal for a division
1218 of the basaltic (B) field of the TAS diagram. IUGS subcommission on the Systematics of Igneous Rocks.
1219 Circular no.38, Contribution no.102, 1983.
1220
1221 Bindeman, I. N., and Bailey, J. C.: Trace elements in anorthite megacrysts from the Kurile Island Arc: a
1222 window to across-arc geochemical variations in magma compositions. *Earth Planet. Sc. Lett.*, 169(3-4),
1223 209-226, 1999.
1224
1225 Brandelik, A.: CALCMIN—an EXCEL™ Visual Basic application for calculating mineral structural formulae from
1226 electron microprobe analyses. *Comput. Geosci-UK*, 35, 1540-1551, 2009.
1227
1228 Brown, W. L., and Parsons, I.: Feldspars in igneous rocks. In Parsons I. (Ed): “Feldspars and their reactions”
1229 (pp. 449-499). Springer, Dordrecht, 1994.
1230
1231 Bryan, W. B., Finger, L. T., and Chayes, F.: Estimating proportions in petrographic mixing equations by least-
1232 squares approximation. *Science*, 163(3870), 926-927, 1969.
1233
1234 Campos-Enríquez, J. O., Garduño-Monroy, V. H.: The shallow structure of Los Humeros and Las
1235 Derrumbadas geothermal fields, Mexico. *Geothermics*, 16, 539-554, 1987.
1236
1237 Campos-Enriquez, J. O., and Sánchez-Zamora, O.: Crustal structure across southern Mexico inferred from
1238 gravity data. *J. S. Am. Earth Sci.*, 13, 479-489, 2000.
1239
1240 Carmichael, I. S. E., Nicholls, J., Spera, F. J., Wood, B. J., and Nelson, S. A.: High-temperature properties of
1241 silicate liquids: applications to the equilibration and ascent of basic magma. *Philos. Tr. R. Soc. S-A*, 286,
1242 373-431, 1977.
1243
1244 Carrasco-Núñez, G., and Branney, M.: Progressive assembly of a massive layer of ignimbrite with normal-to-
1245 reverse compositional zoning: the Zaragoza ignimbrite of central Mexico. *B. Volcanol.*, 68, 3-20, 2005.
1246
1247 Carrasco-Núñez, G., Gómez-Tuena, A., and Lozano, L.: Geologic map of Cerro Grande volcano and
1248 surrounding area, Central México. Geological Society of America Maps and Charts series MCH 081, pp.
1249 10, 1997.
1250
1251 Carrasco-Núñez, G., Siebert, L., Díaz-Castellón, R., Vázquez-Selem, L., Capra, L.: Evolution and hazards of a
1252 long-quiescent compound shield-like volcano: Cofre de Perote, Eastern Trans-Mexican Volcanic Belt. *J.*
1253 *Volcanol. Geoth. Res.*, 197, 209-224, <http://dx.doi.org/10.1016/j.jvolgeores.2009.08.010>, 2010.
1254
1255 Carrasco-Núñez, G., Dávila-Harris, P., Riggs, N. R., Ort, M. H., Zimmer, B. W., Willcox, C. P., and Branney, M.
1256 J.: Recent explosive volcanism at the Eastern Trans-Mexican Volcanic Belt, in: Aranda-Gómez, J. J.,
1257 Tolson, G., and Molina-Garza, R. S. (eds.), *The Southern Cordillera and Beyond*. Geological Society of
1258 America Field Guide 25, p. 83–113, doi:10.1130/2012.0025(05), 2012a.
1259

1260 Carrasco-Núñez, G., McCurry, M., Branney, M. J., Norry, M., and Willcox, C.: Complex magma mixing,
1261 mingling, and withdrawal associated with an intra-Plinian ignimbrite eruption at a large silicic caldera
1262 volcano: Los Humeros of central Mexico. *Geol. Soc. Am. Bull.*, 124(11-12), 1793-1809, 2012b.
1263

1264 Carrasco-Núñez, G., López-Martínez, M., Hernández, J., and Vargas, V.: Subsurface stratigraphy and its
1265 correlation with the surficial geology at Los Humeros geothermal field, eastern Trans-Mexican Volcanic
1266 Belt. *Geothermics*, 67, 1-17, 2017a.
1267

1268 Carrasco-Núñez, G., Hernández, J., De León, L., Dávila, P., Norini, G., Bernal, J. P., Jicha, B., Navarro, M., and
1269 López-Quiroz, P.: Geologic Map of Los Humeros volcanic complex and geothermal field, eastern Trans-
1270 Mexican Volcanic Belt/Mapa geológico del complejo volcánico Los Humeros y campo geotérmico,
1271 sector oriental del Cinturón Volcánico Trans-Mexicano. *Terradigitalis*, 1, 1-11. DOI:
1272 10.22201/igg.terrardigitalis.2017.2.24.78, 2017b.
1273

1274 Carrasco-Núñez, G., Bernal, J. P., Davila, P., Jicha, B., Giordano, G., and Hernández, J.: Reappraisal of Los
1275 Humeros volcanic complex by new U/Th zircon and ⁴⁰Ar/³⁹Ar dating: Implications for greater
1276 geothermal potential. *Geochem. Geophys. Geosy.*, 19, 132-149, 2018.
1277

1278 Carvalho, B. B., and de Assis Janasi, V.: Crystallization conditions and controls on trace element residence in
1279 the main minerals from the Pedra Branca Syenite, Brazil: an electron microprobe and LA-ICPMS study.
1280 *Lithos*, 153, 208-223, 2012.
1281

1282 Casalini, M., Avanzinelli, R., Heumann, A., de Vita, S., Sansivero, F., Conticelli, S., and Tommasini, S.:
1283 Geochemical and radiogenic isotope probes of Ischia volcano, Southern Italy: Constraints on magma
1284 chamber dynamics and residence time. *Am. Mineral.*, 102(2), 262-274, 2017.
1285

1286 Cashman, K. V.: Groundmass crystallization of Mount St. Helens dacite, 1980–1986: a tool for interpreting
1287 shallow magmatic processes. *Contrib. Mineral. Petr.*, 109, 431-449, 1992.
1288

1289 Cashman, K., and Blundy, J.: Degassing and crystallization of ascending andesite and dacite. *Philos. T. Roy.*
1290 *Soc. A*, 358, 1487-1513, 2000.
1291

1292 Cashman, K. V., and Giordano, G.: Calderas and magma reservoirs. *J. Volcanol. Geoth. Res.*, 288, 28-45,
1293 2014.
1294

1295 Cashman, K. V., Sparks, R. S. J., and Blundy, J. D.: Vertically extensive and unstable magmatic systems: a
1296 unified view of igneous processes. *Science*, 355, eaag3055, 2017.
1297

1298 Cathles, L. M., Erendi, A. H. J., and Barrie, T.: How long can a hydrothermal system be sustained by a single
1299 intrusive event? *Econ. Geol.*, 92(7-8), 766-771, 1997.
1300

1301 Chadwick, J. P., Troll, V. R., Waight, T. E., van der Zwan, F. M., and Schwarzkopf, L. M.: Petrology and
1302 geochemistry of igneous inclusions in recent Merapi deposits: a window into the sub-volcanic
1303 plumbing system. *Contrib. Mineral. Petr.*, 165, 259-282, 2013.
1304

1305 Charlier, B. L. A., Bachmann, O., Davidson, J. P., Dungan, M. A., and Morgan, D. J.: The upper crustal
1306 evolution of a large silicic magma body: evidence from crystal-scale Rb–Sr isotopic heterogeneities in
1307 the Fish Canyon magmatic system, Colorado. *J. Petrol.*, 48, 1875-1894, 2007.
1308

1309 Clague, D. A., Moore, J. G., Dixon, J. E., and Friesen, W. B.: Petrology of submarine lavas from Kilauea's Puna
1310 Ridge, Hawaii. *Oceanogr. Lit. Rev.*, 10, 857-858, 1995.
1311

1312 Clarke, A. B., Stephens, S., Teasdale, R., Sparks, R. S. J., and Diller, K.: Petrologic constraints on the
1313 decompression history of magma prior to Vulcanian explosions at the Soufrière Hills volcano,
1314 Montserrat. *J. Volcanol. Geoth. Res.*, 161, 261-274, 2007.
1315

1316 Coombs, M. L., and Gardner, J. E.: Shallow-storage conditions for the rhyolite of the 1912 eruption at
1317 Novarupta, Alaska. *Geology*, 29, 775-778, 2001.
1318

1319 Coombs, M. L., and Gardner, J. E.: Reaction rim growth on olivine in silicic melts: Implications for magma
1320 mixing. *Am. Mineral.*, 89, 748-758, 2004.
1321

1322 Costa, F., Andreatuti, S., de Maisonneuve, C. B., and Pallister, J. S.: Petrological insights into the storage
1323 conditions, and magmatic processes that yielded the centennial 2010 Merapi explosive eruption. *J.*
1324 *Volcanol. Geoth. Res.*, 261, 209-235, 2013.
1325

1326 Crawford, A. J., Falloon, T. J., and Eggins, S.: The origin of island arc high-alumina basalts. *Contrib. Mineral.*
1327 *Petr.*, 97, 417-430, 1987.
1328

1329 Créon, L., Levresse, G., Carrasco-Nuñez, G., and Remusat, L.: Evidence of a shallow magma reservoir below
1330 Los Humeros volcanic complex: Insights from the geochemistry of silicate melt inclusions. *J. S. Am.*
1331 *Earth Sci.*, 88, 446-458, 2018.
1332

1333 Dahren, B., Troll, V. R., Andersson, U. B., Chadwick, J. P., Gardner, M. F., Jaxybulatov, K., and Koulakov, I.:
1334 Magma plumbing beneath Anak Krakatau volcano, Indonesia: evidence for multiple magma storage
1335 regions. *Contrib. Mineral. Petr.*, 163, 631-651, 2012.
1336

1337 Daubeny, C. G. B.: Some account of the eruption of Vesuvius, which occurred in the month of August, 1834,
1338 extracted from the manuscript notes of the cavaliere monticelli, foreign associate of the Geological
1339 Society, and from other sources; together with a statement of the products of the eruption, and of the
1340 condition of the volcano subsequently to it. In: *Abstracts of the Papers Printed in the Philosophical*
1341 *Transactions of the Royal Society of London*, London: The Royal Society, 3, 326-327, 1837.
1342

1343 Davies, J. H.: Global map of solid Earth surface heat flow. *Geochem. Geophys. Geosy.*, 14, 4608-4622, 2013.
1344

1345 Dávila-Harris, P., and Carrasco-Núñez, G.: An unusual syn-eruptive bimodal eruption: the Holocene
1346 Cuicuiltic Member at Los Humeros caldera, Mexico. *J. Volcanol. Geoth. Res.*, 271, 24-42, 2014.
1347

1348 Dawson, J. B., and Hill, P. G.: Mineral chemistry of a peralkaline combeitelamprophyllite nephelinite from
1349 Oldoinyo Lengai, Tanzania. *Mineral. Mag.*, 62(2), 179-196, 1998.
1350

1351 Demant, A.: Características del Eje Neovolcánico Transmexicano y sus problemas de interpretación. *Rev.*
1352 *Mex. Cienc. Geol.*, 2, 172-187, 1978.
1353

1354 DePaolo, D. J.: Trace element and isotopic effects of combined wallrock assimilation and fractional
1355 crystallization. *Earth Planet. Sc. Lett.*, 53(2), 189-202, 1981.
1356

1357 Di Renzo, V., Wohletz, K., Civetta, L., Moretti, R., Orsi, G., and Gasparini, P.: The thermal regime of the
1358 Campi Flegrei magmatic system reconstructed through 3D numerical simulations. *J. Volcanol. Geoth.*
1359 *Res.*, 328, 210-221, 2016.
1360

1361 Donaldson, C. H.: Olivine crystal types in harrisitic rocks of the Rhum pluton and in Archean spinifex rocks.
1362 *Geol. Soc. Am. Bull.*, 85, 1721-1726, 1974.
1363

1364 Duda, A., and Schmincke, H. U.: Polybaric differentiation of alkali basaltic magmas: evidence from green-
1365 core clinopyroxenes (Eifel, FRG). *Contrib. Mineral. Petr.*, 91, 340-353, 1985.
1366

1367 Duffield, W. A., and Sass, J. H.: *Geothermal energy: Clean power from the earth's heat* (Vol. 1249, p. 34).
1368 Reston, VA: U.S. Geothermal Development, US Geological Survey, 2003.
1369

1370 Dungan, M. A., Long, P. E., and Rhodes, J. M.: Magma mixing at mid-ocean ridges: Evidence from legs 45
1371 and 46-DSDP. *Geophys. Res. Lett.*, 5, 423-425, 1978.
1372

1373 Dziewonski, A. M., and Anderson, D. L.: Preliminary reference Earth model. *Phys. Earth Planet. In.*, 25, 297-
1374 356, 1981.
1375

1376 Elardo, S. M., and Shearer, C. K.: Magma chamber dynamics recorded by oscillatory zoning in pyroxene and
1377 olivine phenocrysts in basaltic lunar meteorite Northwest Africa 032. *Am. Mineral.*, 99, 355-368, 2014.
1378

1379 Ellis, B. S., Szymanowski, D., Wotzlaw, J. F., Schmitt, A. K., Bindeman, I. N., Troch, J., Harris, C., Bachmann,
1380 O., and Guillong, M.: Post-caldera volcanism at the Heise volcanic field: implications for petrogenetic
1381 models. *J. Petrol.*, 58, 115-136, 2017.
1382

1383 Eskandari, A., Amini, S., De Rosa, R., and Donato, P.: Nature of the magma storage system beneath the
1384 Damavand volcano (N. Iran): An integrated study. *Lithos*, 300, 154-176, 2018.
1385

1386 Falloon, T. J., and Green, D. H.: Anhydrous partial melting of MORB pyrolite and other peridotite
1387 compositions at 10 kbar: implications for the origin of primitive MORB glasses. *Miner. Petrol.*, 37(3-4),
1388 181-219, 1987.
1389

1390 Faure, F., Trolliard, G., Nicollet, C., and Montel, J. M.: A developmental model of olivine morphology as a
1391 function of the cooling rate and the degree of undercooling. *Contrib. Mineral. Petr.*, 145(2), 251-263,
1392 2003.
1393

1394 Feng, W., and Zhu, Y.: Decoding magma storage and pre-eruptive processes in the plumbing system
1395 beneath early Carboniferous arc volcanoes of southwestern Tianshan, Northwest China. *Lithos*, 322,
1396 362-375, 2018.
1397

1398 Ferrari, L., López-Martínez, M., Aguirre-Díaz, G., and Carrasco-Núñez, G.: Space-time patterns of Cenozoic
1399 arc volcanism in Central Mexico: from the Sierra Madre Occidental to the Mexican Volcanic Belt.
1400 *Geology*, 27, 303-306, 1999.
1401

1402 Ferrari, L., Orozco-Esquivel, T., Manea, V., Manea, M.: The dynamic history of the Trans-Mexican Volcanic
1403 Belt and the Mexico subduction zone. *Tectonophysics*, 522, 122-149, 2012.
1404

1405 Ferriz, H., and Mahood, G. A.: Eruption rates and compositional trends at Los Humeros volcanic center,
1406 Puebla, Mexico. *J. Geophys. Res-Sol. Ea.*, 89(B10), 8511-8524, 1984.
1407

1408 Ferriz, H., and Mahood, G. A.: Strong compositional zonation in a silicic magmatic system: Los Humeros,
1409 Mexican Neovolcanic Belt. *J. Petrol.*, 28, 171-209, 1987.
1410

1411 Fitz-Díaz, E., Lawton, T. F., Juárez-Arriaga, E., and Chávez-Cabello, G.: The Cretaceous-Paleogene Mexican
1412 orogen: Structure, basin development, magmatism and tectonics. *Earth-Sci. Rev.*, 183, 56-84, 2018.
1413

- 1414 Fowler, A. D., Berger, B., Shore, M., Jones, M. I., and Ropchan, J.: Supercooled rocks: development and
1415 significance of varioles, spherulites, dendrites and spinifex in Archaean volcanic rocks, Abitibi
1416 Greenstone belt, Canada. *Precambrian Res.*, 115, 311-328, 2002.
- 1417
- 1418 Freundt, A., and Schmincke, H. U.: Petrogenesis of rhyolite-trachyte-basalt composite ignimbrite P1, Gran
1419 Canada, Canary Islands. *J. Geophys. Res-Sol. Ea.*, 100(B1), 455-474, 1995.
- 1420
- 1421 Fujii, T., and Scarfe, C. M.: Composition of liquids coexisting with spinel lherzolite at 10 kbar and the genesis
1422 of MORBs. *Contrib. Mineral. Petr.*, 90, 18-28, 1985.
- 1423
- 1424 Galipp, K., Klügel, A., and Hansteen, T. H.: Changing depths of magma fractionation and stagnation during
1425 the evolution of an oceanic island volcano: La Palma (Canary Islands). *J. Volcanol. Geoth. Res.*, 155,
1426 285-306, 2006.
- 1427
- 1428 Gao, J. F., and Zhou, M. F.: Generation and evolution of siliceous high magnesium basaltic magmas in the
1429 formation of the Permian Huangshandong intrusion (Xinjiang, NW China). *Lithos*, 162, 128-139, 2013.
- 1430
- 1431 Gardner, M. F., Troll, V. R., Gamble, J. A., Gertisser, R., Hart, G. L., Ellam, R. M., Harris, C., and Wolf, J. A.:
1432 Shallow level differentiation processes at Krakatau: evidence for late-stage crustal contamination. *J.*
1433 *Petrol.*, 54, 149-182, 2013.
- 1434
- 1435 Gernon, T. M., Upton, B. G. J., Ugra, R., Yücel, C., Taylor, R. N., and Elliott, H.: Complex subvolcanic magma
1436 plumbing system of an alkali basaltic maar-diatreme volcano (Elie Ness, Fife, Scotland). *Lithos*, 264, 70-
1437 85, 2016.
- 1438
- 1439 Geshi, N., and Oikawa, T.: The spectrum of basaltic feeder systems from effusive lava eruption to explosive
1440 eruption at Miyakejima volcano, Japan. *B. Volcanol.*, 76(3), 797, 2014.
- 1441
- 1442 Ginibre, C., Kronz, A., and Wörner, G.: High-resolution quantitative imaging of plagioclase composition
1443 using accumulated backscattered electron images: new constraints on oscillatory zoning. *Contrib.*
1444 *Mineral. Petr.*, 142(4), 436-448, 2002.
- 1445
- 1446 Ginibre, C., Wörner, G., and Kronz, A.: Crystal zoning as an archive for magma evolution. *Elements*, 3, 261-
1447 266, 2007.
- 1448
- 1449 Giordano, G., Lucci, F., Phillips, D., Cozzupoli, D., and Runci, V.: Stratigraphy, geochronology and evolution
1450 of the Mt. Melbourne volcanic field (North Victoria Land, Antarctica). *B. Volcanol.*, 74, 1985-2005,
1451 2012.
- 1452
- 1453 Giuffrida, M., and Viccaro, M.: Three years (2011–2013) of eruptive activity at Mt. Etna: working modes and
1454 timescales of the modern volcano plumbing system from micro-analytical studies of crystals. *Earth-Sci.*
1455 *Rev.*, 171, 289-322, 2017.
- 1456
- 1457 Glazner, A. F., Bartley, J. M., Coleman, D. S., Gray, W., and Taylor, R. Z.: Are plutons assembled over millions
1458 of years by amalgamation from small magma chambers? *GSA today*, 14, 4-12, 2004.
- 1459
- 1460 Gómez-Tuena, A., and Carrasco-Núñez, G.: Cerro Grande volcano: the evolution of a Miocene stratocone in
1461 the early Trans-Mexican Volcanic Belt, *Tectonophysics*, 318, 249-280, 2000.
- 1462
- 1463 Gómez-Tuena, A., LaGatta, A.B., Langmuir, C.H., Goldstein, S.L., Ortega-Gutiérrez, F., Carrasco-Núñez, G.:
1464 Temporal control of subduction magmatism in the eastern Trans-Mexican Volcanic Belt: mantle

1465 sources, slab contributions, and crustal contamination. *Geochem. Geophys. Geos.*, 4,
1466 <http://dx.doi.org/10.1029/2003GC000524>, 2003.

1467

1468 Gómez-Tuena, A., Langmuir, C.H., Goldstein, S.L., Straub, S., Ortega-Gutiérrez, F.: Geochemical evidence for
1469 slab melting in the Trans-Mexican Volcanic Belt. *J. Petrol.*, 48, 537–562, 2007a.

1470

1471 Gómez-Tuena, A., Orozco-Esquivel, M.T., Ferrari, L.: Igneous petrogenesis of the Transmexican Volcanic
1472 Belt. In: Alaniz-Álvarez, S.A., Nieto-Samaniego, A.F. (Eds.), *Geology of México: Celebrating the*
1473 *Centenary of the Geological Society of México*. *Geol. S. Am. S.*, 422, 129–181, 2007b.

1474

1475 Gómez-Tuena, A., Mori, L., Straub, S.: Geochemical and petrological insights into the tectonic origin of the
1476 Transmexican Volcanic Belt, *Earth-Sci. Rev.* 183, 153-181.
1477 <http://dx.doi.org/10.1016/j.earscirev.2016.12.006>, 2018.

1478

1479 Gregg, P. M., De Silva, S. L., Grosfils, E. B., and Parmigiani, J. P.: Catastrophic caldera-forming eruptions:
1480 Thermomechanics and implications for eruption triggering and maximum caldera dimensions on Earth.
1481 *J. Volcanol. Geoth. Res.*, 241, 1-12, 2012.

1482

1483 Grove, T. L.: Origin of Magmas, *Encyclopedia of Volcanoes*, 133-148, 2000.

1484

1485 Grove, T. L., Gerlach, D. C., and Sando, T. W.: Origin of calc-alkaline series lavas at Medicine Lake volcano by
1486 fractionation, assimilation and mixing. *Contrib. Mineral. Petr.*, 80, 160-182, 1982.

1487

1488 Grove, T. L., Donnelly-Nolan, J. M., and Housh, T.: Magmatic processes that generated the rhyolite of Glass
1489 Mountain, Medicine Lake volcano, N. California. *Contrib. Mineral. Petr.*, 127, 205-223, 1997.

1490

1491 Gualda, G. A., and Ghiorso, M. S.: The Bishop Tuff giant magma body: an alternative to the Standard Model.
1492 *Contrib. Mineral. Petr.*, 166, 755-775, 2013.

1493

1494 Gunnarsson, G., and Aradóttir, E. S.: The deep roots of geothermal systems in volcanic areas: boundary
1495 conditions and heat sources in reservoir modeling. *Transport in Porous Media*, 108, 43-59, 2015.

1496

1497 Herzberg, C., and O'Hara, M. J.: Plume-associated ultramafic magmas of Phanerozoic age. *J. Petrol.*, 43,
1498 1857-1883, 2002.

1499

1500 Hildreth, W.: The Bishop Tuff: Evidence for the origin of compositional zonation in silicic magma chambers.
1501 *Geol. S. Am. S.*, 180, 43-75, 1979.

1502

1503 Hildreth, W.: Gradients in silicic magma chambers: implications for lithospheric magmatism. *J. Geophys.*
1504 *Res-Sol. Ea.*, 86(B11), 10153-10192, 1981.

1505

1506 Hildreth, W., and Wilson, C. J.: Compositional zoning of the Bishop Tuff. *J. Petrol.*, 48, 951-999, 2007.

1507

1508 Hirano, N., Yamamoto, J., Kagi, H., and Ishii, T.: Young, olivine xenocryst-bearing alkali-basalt from the
1509 oceanward slope of the Japan Trench. *Contrib. Mineral. Petr.*, 148(1), 47-54, 2004.

1510

1511 Hofmann, A. W.: Magma chambers on a slow burner. *Nature* 49, 677–678, 2012.

1512

1513 Holland, T., and Powell, R.: Plagioclase feldspars: activity-composition relations based upon Darken's
1514 quadratic formalism and Landau theory. *Am. Mineral.*, 77, 53-61, 1992.

1515

1516 Hu, J. H., Song, X. Y., He, H. L., Zheng, W. Q., Yu, S. Y., Chen, L. M., and Lai, C. K.: Constraints of texture and
1517 composition of clinopyroxene phenocrysts of Holocene volcanic rocks on a magmatic plumbing system
1518 beneath Tengchong, SW China. *J. Asian Earth Sci.*, 154, 342-353, 2018.
1519

1520 Humphreys, M. C., Blundy, J. D., and Sparks, R. S. J.: Magma evolution and open-system processes at
1521 Shiveluch Volcano: Insights from phenocryst zoning. *J. Petrol.*, 47, 2303-2334, 2006.
1522

1523 Humphreys, M. C., Christopher, T., and Hards, V.: Microlite transfer by disaggregation of mafic inclusions
1524 following magma mixing at Soufrière Hills volcano, Montserrat. *Contrib. Mineral. Petr.*, 157, 609-624,
1525 2009.
1526

1527 Huraiová, M., Konečný, P., Holický, I., Milovská, S., Nemeč, O., and Hurai, V.: Mineralogy and origin of
1528 peralkaline granite-syenite nodules ejected in Pleistocene basalt from Bulhary, southern Slovakia.
1529 *Period. Mineral.*, 86, 1-17, 2017.
1530

1531 Innocenti, S., del Marmol, M. A., Voight, B., Andreastuti, S., and Furman, T.: Textural and mineral chemistry
1532 constraints on evolution of Merapi Volcano, Indonesia. *J. Volcanol. Geoth. Res.*, 261, 20-37, 2013.
1533

1534 Jackson, M. D., Blundy, J., and Sparks, R. S. J.: Chemical differentiation, cold storage and remobilization of
1535 magma in the Earth's crust. *Nature*, 564(7736), 405, 2018.
1536

1537 Jarosewich, E., Nelen, J. A., and Norberg, J.A.: Reference samples for electron microprobe analysis.
1538 *Geostandard. Newslett.*, 4, 43-47 with corrections in: *Geostandard. Newslett.*, 4, 257-258, 1980.
1539

1540 Jeffery, A. J., Gertisser, R., Troll, V. R., Jolis, E. M., Dahren, B., Harris, C., Tindle, A. G., Preece, K., O'Driscoll,
1541 B., Humaida, H., and Chadwick, J. P.: The pre-eruptive magma plumbing system of the 2007–2008
1542 dome-forming eruption of Kelut volcano, East Java, Indonesia. *Contrib. Mineral. Petr.*, 166, 275-308,
1543 2013.
1544

1545 Jellinek, A. M., and DePaolo, D. J.: A model for the origin of large silicic magma chambers: precursors of
1546 caldera-forming eruptions. *B. Volcanol.*, 65, 363-381, 2003.
1547

1548 Keiding, J. K., and Sigmarsson, O.: Geothermobarometry of the 2010 Eyjafjallajökull eruption: New
1549 constraints on Icelandic magma plumbing systems. *J. Geophys. Res-Sol. Ea.*, 117(B9),
1550 doi:10.1029/2011JB008829, 2012.
1551

1552 Keil, K., Fodor, R. V., and Bunch, T. E.: Contributions to the mineral chemistry of Hawaiian rocks. *Contrib.*
1553 *Mineral. Petr.*, 37(4), 253-276, 1972.
1554

1555 Kelley, D. F., and Barton, M.: Pressures of crystallization of Icelandic magmas. *J. Petrol.*, 49, 465-492, 2008.
1556

1557 Kinman, W. S., and Neal, C. R.: Magma evolution revealed by anorthite-rich plagioclase cumulate xenoliths
1558 from the Ontong Java Plateau: insights into LIP magma dynamics and melt evolution. *J. Volcanol.*
1559 *Geoth. Res.*, 154(1-2), 131-157, 2006.
1560

1561 Kinzler, R. J., Donnelly-Nolan, J. M., and Grove, T. L.: Late Holocene hydrous mafic magmatism at the Paint
1562 Pot Crater and Callahan flows, Medicine Lake Volcano, N. California and the influence of H₂O in the
1563 generation of silicic magmas. *Contrib. Mineral. Petr.*, 138, 1-16, 2000.
1564

1565 Klügel, A., Hoernle, K. A., Schmincke, H. U., and White, J. D.: The chemically zoned 1949 eruption on La
1566 Palma (Canary Islands): Petrologic evolution and magma supply dynamics of a rift zone eruption. *J.*
1567 *Geophys. Res-Sol. Ea.*, 105(B3), 5997-6016, 2000.

1568
1569 Klügel, A., Hansteen, T. H., and Galipp, K.: Magma storage and underplating beneath Cumbre Vieja volcano,
1570 la Palma (Canary Islands). *Earth Planet. Sc. Lett.*, 236, 211-226, 2005.
1571
1572 Kontonikas-Charos, A., Ciobanu, C. L., Cook, N. J., Ehrig, K., Krneta, S., and Kamenetsky, V. S.: Feldspar
1573 evolution in the Roxby Downs Granite, host to Fe-oxide Cu-Au-(U) mineralisation at Olympic Dam,
1574 South Australia. *Ore Geol. Rev.*, 80, 838-859, 2017.
1575
1576 Kratzmann, D. J., Carey, S., Scasso, R., and Naranjo, J. A.: Compositional variations and magma mixing in the
1577 1991 eruptions of Hudson volcano, Chile. *B. Volcanol.*, 71, 419-439, DOI:10.1007/s00445-008-0234-x,
1578 2009.
1579
1580 Kushiro, I.: The system forsterite-diopside-silica with and without water at high pressures. *Am. J. Sci.*,
1581 267(A), 269-294, 1969.
1582
1583 Kushiro, I., and Yoder, H. S., Jr.: Melting of forsterite and enstatite at high pressures and hydrous
1584 conditions. *Carnegie Inst. Wash. Yrbk.*, 67, 153-158, 1969.
1585
1586 Lange, R. A., Frey, H. M., and Hector, J.: A thermodynamic model for the plagioclase-liquid
1587 hygrometer/thermometer. *Am. Mineral.*, 94, 494-506, 2009.
1588
1589 Langmuir, C. H., and Hanson, G. N.: An evaluation of major element heterogeneity in the mantle sources of
1590 basalts. *Philos. Tr. R. Soc. S-A*, 297(1431), 383-407, 1980.
1591
1592 Latutrie, B., Harris, A., Médard, E., and Gurioli, L.: Eruption and emplacement dynamics of a thick trachytic
1593 lava flow of the Sancy volcano (France). *Bulletin of Volcanology*, 79(1), 4, 2017.
1594
1595 Laumonier, M., Scaillet, B., Arbaret, L., and Champallier, R.: Experimental simulation of magma mixing at
1596 high pressure. *Lithos*, 196, 281-300, 2014.
1597
1598 Le Maitre, R. W., Streckeisen, A., Zanettin, B., Le Bas, M. J., Bonin, B., Bateman, P., Bellieni, G., Dudek, A.,
1599 Efremova, S., Keller, J., Lameyre, J., Sabine, P. A., Schmid, R., Sørensen, H., Woolley, A. R.: *Igneous
1600 Rocks. A Classification and Glossary of terms. Recommendations of the IUGS Subcommission on the
1601 Systematics of Igneous Rocks*, Cambridge University Press, pp. 236, 2002.
1602
1603 Lee, C. T. A., Lee, T. C., and Wu, C. T.: Modeling the compositional evolution of recharging, evacuating, and
1604 fractionating (REFC) magma chambers: Implications for differentiation of arc magmas. *Geochim.
1605 Cosmochim. Ac.*, 143, 8-22, 2014.
1606
1607 Lindsley, D. H.: Pyroxene thermometry. *Am. Mineral.*, 68, 477-493, 1983.
1608
1609 Lucci, F., Rossetti, F., White, J. C., Moghadam, H. S., Shirzadi, A., and Nasrabady, M.: Tschermak
1610 fractionation in calc-alkaline magmas: the Eocene Sabzevar volcanism (NE Iran). *Arab. J. Geosci.*, 9(10),
1611 573, 2016.
1612
1613 Lucci, F., Rossetti, F., Becchio, R., Theye, T., Gerdes, A., Opitz, J., Baez, W., Bardelli, L., De Astis, G.,
1614 Viramonte, J., and Giordano, G.: Magmatic Mn-rich garnets in volcanic settings: Age and longevity of
1615 the magmatic plumbing system of the Miocene Ramadas volcanism (NW Argentina). *Lithos*, 322, 238-
1616 249, 2018.
1617
1618 MacLennan, J., McKenzie, D., Gronvöld, K., and Slater, L.: Crustal accretion under northern Iceland. *Earth
1619 Planet. Sc. Lett.*, 191, 295-310, 2001.

1620
1621 Martinez, M., Fernindez, R., Visque, R., Vega, R., Reyes, S. A.: Asimilacion del metodo magnetotelurico
1622 para la exploracion geotermica. Quinto informe tecnico CICESE-IIE, Mexico, 1983.
1623
1624 Masotta, M., Mollo, S., Freda, C., Gaeta, M., and Moore, G.: Clinopyroxene–liquid thermometers and
1625 barometers specific to alkaline differentiated magmas. *Contrib. Mineral. Petr.*, 166, 1545-1561, 2013.
1626
1627 Matthews, N. E., Vazquez, J. A., Calvert, A. T.: Age of the Lava Creek supereruption and magma chamber
1628 assembly at Yellowstone based on $^{40}\text{Ar}/^{39}\text{Ar}$ and U-Pb dating of sanidine and zircon crystals.
1629 *Geochem. Geophys. Geosy.*, 16, 2508–2528, 2015.
1630
1631 Melluso, L., Conticelli, S., and De'Gennaro, R.: Kirschsteinite in the Capo di Bove melilite leucitite lava
1632 (cecilite), Alban Hills, Italy. *Mineral. Mag.*, 74(5), 887-902, 2010.
1633
1634 Melluso, L., Morra, V., Guarino, V., De'Gennaro, R., Franciosi, L., and Grifa, C.: The crystallization of
1635 shoshonitic to peralkaline trachyphonolitic magmas in a H₂O–Cl–F-rich environment at Ischia (Italy),
1636 with implications for the feeder system of the Campania Plain volcanoes. *Lithos*, 210, 242-259, 2014.
1637
1638 Moghadam, H. S., Rossetti, F., Lucci, F., Chiaradia, M., Gerdes, A., Martinez, M. L., Ghorbani, G., and
1639 Nasrabad, M.: The calc-alkaline and adakitic volcanism of the Sabzevar structural zone (NE Iran):
1640 implications for the Eocene magmatic flare-up in Central Iran. *Lithos*, 248, 517-535, 2016.
1641
1642 Mollo, S., Del Gaudio, P., Ventura, G., Iezzi, G., and Scarlato, P.: Dependence of clinopyroxene composition
1643 on cooling rate in basaltic magmas: implications for thermobarometry. *Lithos*, 118, 302-312, 2010.
1644
1645 Mordick, B. E., and Glazner, A. F.: Clinopyroxene thermobarometry of basalts from the Coso and Big Pine
1646 volcanic fields, California. *Contrib. Mineral. Petr.*, 152, 111-124, 2006.
1647
1648 Morimoto, N.: Nomenclature of pyroxenes. *Am. Mineral.*, 73, 1123-1133, 1988.
1649
1650 Morimoto, N.: Nomenclature of pyroxenes. *Mineral. J.*, 14, 198-221, 1989.
1651
1652 Mutch, E. J. F., Blundy, J. D., Tattitch, B. C., Cooper, F. J., and Brooker, R. A.: An experimental study of
1653 amphibole stability in low-pressure granitic magmas and a revised Al-in-hornblende geobarometer.
1654 *Contrib. Mineral. Petr.*, 171:85, 1-27, <https://doi.org/10.1007/s00410-016-1298-9>, 2016.
1655
1656 Nabelek, P. I., Hofmeister, A. M., and Whittington, A. G.: The influence of temperature-dependent thermal
1657 diffusivity on the conductive cooling rates of plutons and temperature-time paths in contact aureoles.
1658 *Earth Planet. Sc. Lett.*, 317, 157-164, 2012.
1659
1660 Nairn, I. A., Kobayashi, T., and Nakagawa, M.: The ~10 ka multiple vent pyroclastic eruption sequence at
1661 Tongariro Volcanic Centre, Taupo Volcanic Zone, New Zealand: Part 1. Eruptive processes during
1662 regional extension. *J. Volcanol. Geoth. Res.*, 86, 19-44, 1998.
1663
1664 Nakagawa, M., Nairn, I. A., and Kobayashi, T.: The similar to 10 ka multiple vent pyroclastic eruption
1665 sequence at Tongariro Volcanic Centre, Taupo Volcanic Zone, New Zealand: Part 2. Petrological insights
1666 into magma storage and transport during regional extension. *J. Volcanol. Geoth. Res.*, 86, 45-65, 1998.
1667
1668 Namur, O., Charlier, B., Toplis, M. J., and Vander Auwera, J.: Prediction of plagioclase-melt equilibria in
1669 anhydrous silicate melts at 1-atm. *Contrib. Mineral. Petr.*, 163, 133-150, 2012.
1670

1671 Neave, D. A., Maclennan, J., Hartley, M. E., Edmonds, M., and Thordarson, T.: Crystal storage and transfer in
1672 basaltic systems: the Skuggafjöll eruption, Iceland. *J. Petrol.*, 55, 2311-2346, 2014.
1673

1674 Nengendak, J. F. W., Emmermann, R., Krawczyk, R., Mooser, F., Tobschall, H., and Werle, D.: Geological and
1675 geochemical investigations on the eastern trans mexican volcanic belt. *Geofis. Int.*, 24, 477-575, 1985.
1676

1677 Nekvasil, H.: Feldspar crystallisation in felsic magmas: a review. *Earth Env. Sci. Tr. So.*, 83(1-2), 399-407,
1678 1992.
1679

1680 Njonfang, E., Tchoneng, G. T., Cozzupoli, D., and Lucci, F.: Petrogenesis of the Sabongari alkaline complex,
1681 cameroon line (central Africa): Preliminary petrological and geochemical constraints. *J. Afr. Earth Sci.*,
1682 83, 25-54, 2013.
1683

1684 Norini, G., Gropelli, G., Sulpizio, R., Carrasco-Núñez, G., Dávila-Harris, P., Pellicoli, C., Zucca, F., and De
1685 Franco, R.: Structural analysis and thermal remote sensing of the Los Humeros Volcanic Complex:
1686 Implications for volcano structure and geothermal exploration. *J. Volcanol. Geoth. Res.*, 301, 221-237,
1687 2015.
1688

1689 O'Neill, H. S. C. and Jenner, F.: The global pattern of trace element distributions in ocean floor basalts.
1690 *Nature* 491, 698–705, 2012.
1691

1692 Pamukcu, A. S., Gualda, G. A., Bégué, F., and Gravley, D. M.: Melt inclusion shapes: Timekeepers of short-
1693 lived giant magma bodies. *Geology*, 43, 947-950, 2015.
1694

1695 Papike, J. J., Spilde, M. N., Fowler, G. W., Layne, G. D., and Shearer, C. K.: The Lodran primitive achondrite:
1696 Petrogenetic insights from electron and ion microprobe analysis of olivine and orthopyroxene.
1697 *Geochim. Cosmochim. Ac.*, 59(14), 3061-3070, 1995.
1698

1699 Patanè, D., De Gori, P., Chiarabba, C., and Bonaccorso, A.: Magma ascent and the pressurization of Mount
1700 Etna's volcanic system. *Science*, 299, 2061-2063, 2003.
1701

1702 Petrone, C. M., Bugatti, G., Braschi, E., and Tommasini, S.: Pre-eruptive magmatic processes re-timed using
1703 a non-isothermal approach to magma chamber dynamics. *Nat. Commun.*, 7, 12946, 2016.
1704

1705 Pietruszka, A. J., and Garcia, M. O.: The size and shape of Kilauea Volcano's summit magma storage
1706 reservoir: a geochemical probe. *Earth Planet. Sc. Lett.*, 167, 311-320, 1999.
1707

1708 Piilonen, P. C., McDonald, A. M., and Lalonde, A. E.: The crystal chemistry of aegirine from Mont Saint-
1709 Hilaire, Quebec. *Can. Mineral.*, 36(3), 779-791, 1998.
1710

1711 Plümper, O., and Putnis, A.: The complex hydrothermal history of granitic rocks: multiple feldspar
1712 replacement reactions under subsolidus conditions. *J. Petrol.*, 50(5), 967-987, 2009
1713

1714 Preece, K., Barclay, J., Gertisser, R., and Herd, R. A.: Textural and micro-petrological variations in the
1715 eruptive products of the 2006 dome-forming eruption of Merapi volcano, Indonesia: implications for
1716 sub-surface processes. *J. Volcanol. Geoth. Res.*, 261, 98-120, 2013.
1717

1718 Presnall, D. C., Dixon, S. A., Dixon, J. R., O'Donnell, T. H., Brenner, N. L., Schrock, R. L., and Dycus, D. W.:
1719 Liquidus phase relations on the join diopside-forsterite-anorthite from 1 atm to 20 kbar: their bearing
1720 on the generation and crystallization of basaltic magma. *Contrib. Mineral. Petr.*, 66, 203-220, 1978.
1721

1722 Putirka, K.: Magma transport at Hawaii: Inferences based on igneous thermobarometry. *Geology*, 25, 69-72,
1723 1997.
1724

1725 Putirka, K.: Clinopyroxene+liquid equilibria to 100 kbar and 2450 K. *Contrib. Mineral. Petr.*, 135, 151-163,
1726 1999.
1727

1728 Putirka, K. D.: Mantle potential temperatures at Hawaii, Iceland, and the mid-ocean ridge system, as
1729 inferred from olivine phenocrysts: Evidence for thermally driven mantle plumes. *Geochem. Geophys.*
1730 *Geosy.*, 6, doi:10.1029/2005GC000915, 2005a.
1731

1732 Putirka, K. D.: Igneous thermometers and barometers based on plagioclase+ liquid equilibria: Tests of some
1733 existing models and new calibrations. *Am. Mineral.*, 90, 336-346, 2005b.
1734

1735 Putirka, K. D.: Thermometers and barometers for volcanic systems. *Rev. Mineral. Geochem.*, 69, 61-120,
1736 2008.
1737

1738 Putirka, K., Johnson, M., Kinzler, R., Longhi, J., and Walker, D.: Thermobarometry of mafic igneous rocks
1739 based on clinopyroxene-liquid equilibria, 0–30 kbar. *Contrib. Mineral. Petr.*, 123, 92-108, 1996.
1740

1741 Putirka, K., Ryerson, F. J., and Mikaelian, H.: New igneous thermobarometers for mafic and evolved lava
1742 compositions, based on clinopyroxene+ liquid equilibria. *Am. Mineral.*, 88, 1542-1554, 2003.
1743

1744 Putirka, K. D., Perfit, M., Ryerson, F. J., and Jackson, M. G.: Ambient and excess mantle temperatures,
1745 olivine thermometry, and active vs. passive upwelling. *Chem. Geol.*, 241, 177-206, 2007.
1746

1747 Redman, B. A., and Keays, R. R.: Archaean basic volcanism in the eastern Goldfields province, Yilgarn Block,
1748 western Australia. *Precambrian Res.*, 30, 113-152, 1985.
1749

1750 Renjith, M. L.: Micro-textures in plagioclase from 1994–1995 eruption, Barren Island Volcano: evidence of
1751 dynamic magma plumbing system in the Andaman subduction zone. *Geosci. Front.*, 5(1), 113-126,
1752 2014.
1753

1754 Reubi, O., and Nicholls, I. A.: Magmatic evolution at Batur volcanic field, Bali, Indonesia: petrological
1755 evidence for polybaric fractional crystallization and implications for caldera-forming eruptions. *J.*
1756 *Volcanol. Geoth. Res.*, 138, 345-369, 2004.
1757

1758 Rhodes, J. M., Dungan, M. A., Blanchard, D. P., and Long, P. E.: Magma mixing at mid-ocean ridges:
1759 evidence from basalts drilled near 22 N on the Mid-Atlantic Ridge. *Tectonophysics*, 55, 35-61, 1979.
1760

1761 Rivera, T. A., Schmitz, M. D., Crowley, J. L., and Storey, M.: Rapid magma evolution constrained by zircon
1762 petrochronology and ⁴⁰Ar/³⁹Ar sanidine ages for the Huckleberry Ridge Tuff, Yellowstone, USA,
1763 *Geology*, 42, 643-646, 2014.
1764

1765 Roeder, P. L., and Emslie, R.: Olivine-liquid equilibrium. *Contrib. Mineral. Petr.*, 29, 275-289, 1970.
1766

1767 Rojas-Ortega, E.: Litoestratigrafía, petrografía y geoquímica de la toba Llano, y su relación con el cráter el
1768 Xalapazco, Caldera de LosHumeros, Puebla. MS Thesis, IPICYT, San Luis Potosí, México, pp. 129, 2016.
1769

1770 Romo-Jones, J. M., Gutiérrez-Negrín, L. C. A., Flores-Armenta, M., Del Valle, J. L., and García, A: Mexico, in:
1771 2017 Annual Report, IEA Geothermal, 66–72, available at:
1772 <https://drive.google.com/file/d/1ztLIE5MFdLwSndR7iLmAkMXnQth4c86T/view>, 2017.
1773

1774 Rutherford, M. J.: Magma ascent rates. *Rev. Mineral. Geochem.*, 69(1), 241-271, 2008.
1775
1776 Rutherford, M. J., and Gardner, J. E.: Rates of magma ascent. *Encyclopedia of Volcanoes*, 207-217, 2000.
1777
1778 Rutherford, M. J., Sigurdsson, H., Carey, S., and Davis, A.: The May 18, 1980, eruption of Mount St. Helens:
1779 1. Melt composition and experimental phase equilibria. *J. Geophys. Res-Sol. Ea.*, 90(B4), 2929-2947,
1780 1985.
1781
1782 Sano, T., and Yamashita, S.: Experimental petrology of basement lavas from Ocean Drilling Program Leg
1783 192: implications for differentiation processes in Ontong Java Plateau magmas. *Geol. Soc. Spec. Publ.*,
1784 229(1), 185-218, 2004.
1785
1786 Scott, J. A., Mather, T. A., Pyle, D. M., Rose, W. I., and Chigna, G.: The magmatic plumbing system beneath
1787 Santiaguito Volcano, Guatemala. *J. Volcanol. Geoth. Res.*, 237, 54-68, 2012.
1788
1789 Shane, P., and Coote, A.: Thermobarometry of Whangarei volcanic field lavas, New Zealand: Constraints on
1790 plumbing systems of small monogenetic basalt volcanoes. *J. Volcanol. Geoth. Res.*, 354, 130-139, 2018.
1791
1792 Sigmarsson, O., Vlastélic, I., Andreasen, R., Bindeman, I., Devidal, J. L., Moune, S., Keiding, J. K., Larsen, G.,
1793 Hoskuldsson, A., and Thordarson, T.: Dynamic magma mixing revealed by the 2010 Eyjafjallajökull
1794 eruption. *Solid Earth Discussions*, 3, 591-613, 2011.
1795
1796 Sisson, T. W., and Grove, T. L.: Temperatures and H₂O contents of low-MgO high-alumina basalts. *Contrib.*
1797 *Mineral. Petr.*, 113, 167-184, 1993.
1798
1799 Sisson, T. W., and Layne, G. D.: H₂O in basalt and basaltic andesite glass inclusions from four subduction-
1800 related volcanoes. *Earth Planet. Sc. Lett.*, 117, 619-635, 1993.
1801
1802 Smith, R. L., and Shaw, H. R.: Igneous-related geothermal systems. *US Geological Survey Circular 726*, 58-83,
1803 1975.
1804
1805 Solano, J. M. S., Jackson, M. D., Sparks, R. S. J., and Blundy, J.: Evolution of major and trace element
1806 composition during melt migration through crystalline mush: implications for chemical differentiation
1807 in the crust. *Am. J. Sci.*, 314(5), 895-939, 2014.
1808
1809 Sparks, R. S. J.: The dynamics of bubble formation and growth in magmas: a review and analysis. *J. Volcanol.*
1810 *Geoth. Res.*, 3(1-2), 1-37, 1978.
1811
1812 Sparks, R. S. J., Young, S. R., Barclay, J., Calder, E. S., Cole, P., Darroux, B., Davies, M. A., Druitt, T. H.,
1813 Harford, C., Herd, R., James, M., Lejeune, A. M., Loughliun, S., Norton, G., Skerrit, G., Stasiuk, M. V.,
1814 Stevens, N. S., Toothill, J., Wadge, G., and Watts, R.: Magma production and growth of the lava dome
1815 of the Soufriere Hills Volcano, Montserrat, West Indies: November 1995 to December 1997. *Geophys.*
1816 *Res. Lett.*, 25(18), 3421-3424, 1998.
1817
1818 Streck, M. J.: Mineral textures and zoning as evidence for open system processes. *Rev. Mineral. Geochem.*,
1819 69(1), 595-622, 2008
1820
1821 Stroncik, N. A., Klügel, A., and Hansteen, T. H.: The magmatic plumbing system beneath El Hierro (Canary
1822 Islands): constraints from phenocrysts and naturally quenched basaltic glasses in submarine rocks.
1823 *Contrib. Mineral. Petr.*, 157, 593-607, DOI:10.1007/s00410-008-0354-5, 2009.
1824

1825 Suter, M.: Structural traverse across the Sierra Madre Oriental fold-thrust belt in east-central Mexico. *Geol.*
1826 *Soc. Am. Bull.*, 98(3), 249-264, 1987.

1827

1828 Takahashi, E.: Melting of a dry peridotite KLB-1 up to 14 GPa: Implications on the origin of peridotitic upper
1829 mantle. *J. Geophys. Res-Sol. Ea.*, 91(B9), 9367-9382, 1986.

1830

1831 Thompson, R. N.: Primary basalts and magma genesis. *Contrib. Mineral. Petr.*, 45, 317-341, 1974.

1832

1833 Troll, V. R., Deegan, F. M., Jolis, E. M., Harris, C., Chadwick, J. P., Gertisser, R., Schwarzkopf, L. M., Borisova,
1834 A., Bindeman, I. N., Sumarti, S., and Preece, K.: Magmatic differentiation processes at Merapi Volcano:
1835 inclusion petrology and oxygen isotopes. *J. Volcanol. Geoth. Res.*, 261, 38-49, 2013.

1836

1837 Ubide, T., Gale, C., Arranz, E., Lago, M., and Larrea, P.: Clinopyroxene and amphibole crystal populations in
1838 a lamprophyre sill from the Catalonian Coastal Ranges (NE Spain): a record of magma history and a
1839 window to mineral-melt partitioning. *Lithos*, 184, 225-242, 2014.

1840

1841 Urbani, S., Giordano, G., Lucci, F., Rossetti, F., Acocella, V., and Carrasco-Núñez, G.: Estimating the depth
1842 and evolution of intrusions at resurgent calderas: Los Humeros (Mexico), *Solid Earth Discuss.*,
1843 <https://doi.org/10.5194/se-2019-100>, in review, 2019.

1844

1845 Ushioda, M., Takahashi, E., Hamada, M., and Suzuki, T.: Water content in arc basaltic magma in the
1846 Northeast Japan and Izu arcs: an estimate from Ca/Na partitioning between plagioclase and melt.
1847 *Earth Planets Space*, 66(1), 127, 2014.

1848

1849 Verma, S. P.: Magma genesis and chamber processes at Los Humeros caldera, Mexico—Nd and Sr isotope
1850 data. *Nature*, 302(5903), 52, 1983.

1851

1852 Verma, S. P.: Alkali and alkaline earth element geochemistry of Los Humeros caldera, Puebla, Mexico. *J.*
1853 *Volcanol. Geoth. Res.*, 20, 21–40, 1984.

1854

1855 Verma, S. P.: Heat source in Los Humeros geothermal area, Puebla, Mexico. *Geoth. Res. T.*, 9, 521-525,
1856 1985a.

1857

1858 Verma, S. P.: On the magma chamber characteristics as inferred from surface geology and geochemistry:
1859 examples from Mexican geothermal areas. *Phys. Earth Planet. In.*, 41, 207-214, 1985b.

1860

1861 Verma, S. P.: Geochemical evidence for a lithospheric source for magmas from Los Humeros caldera,
1862 Puebla, Mexico. *Chem. Geol.*, 164, 35-60, 2000.

1863

1864 Verma, S. P., and López, M.: Geochemistry of Los Humeros caldera, Puebla, Mexico. *B. Volcanol.*, 45, 63-79,
1865 1982.

1866

1867 Verma M. P., Verma, S. P. and Sanvincente, H.: Temperature field simulation with stratification model of
1868 magma chamber under Los Humeros caldera, Puebla, Mexico. *Geothermics*, 19, 187-197, 1990.

1869

1870 Verma, S. P., and Andaverde, J.: Temperature field distribution from cooling of a magma chamber.
1871 *Proceeding World Geothermal Congress*, 1119-1121, 1995.

1872

1873 Verma, S. P., Gomez-Arias, E. and Andaverde J.: Thermal sensitivity analysis of emplacement of the magma
1874 chamber in Los Humeros caldera, Puebla, Mexico. *Int. Geol. Rev.*, 53, 905-925, 2011.

1875

- 1876 Verma, S. P. and Gomez-Arias, E.: Three-dimensional temperature field simulation of magma chamber in
1877 the Los Humeros geothermal field, Puebla, Mexico. *Appl. Therm. Eng.*, 52, 512-515, 2013.
1878
- 1879 Viccaro, M., Calcagno, R., Garozzo, I., Giuffrida, M., and Nicotra, E.: Continuous magma recharge at Mt. Etna
1880 during the 2011–2013 period controls the style of volcanic activity and compositions of erupted lavas.
1881 *Miner. Petrol.*, 109, 67-83, 2015.
1882
- 1883 Viccaro, M., Barca, D., Bohrsen, W. A., D'Oriano, C., Giuffrida, M., Nicotra, E., and Pitcher, B. W.: Crystal
1884 residence times from trace element zoning in plagioclase reveal changes in magma transfer dynamics
1885 at Mt. Etna during the last 400 years. *Lithos*, 248, 309-323, 2016.
1886
- 1887 Viniegra-Osorio, F.: *Geología del Macizo de Teziutlán y la Cuenca Cenozoica de Veracruz*. Asoc. Mex.
1888 *Geólogos Petroleros Bol.*, 17, 101-163, 1965.
1889
- 1890 Wagner, T. P., Donnelly-Nolan, J. M., and Grove, T. L.: Evidence of hydrous differentiation and crystal
1891 accumulation in the low-MgO, high-Al₂O₃ lake basalt from Medicine Lake volcano, California. *Contrib.*
1892 *Mineral. Petr.*, 121, 201-216, 1995.
1893
- 1894 Wallace, P., and Anderson, A. T. Jr.: Volatiles in Magmas. *Encyclopedia of Volcanoes*, 149–170, 2000.
1895
- 1896 Waters, L. E., and Lange, R. A.: An updated calibration of the plagioclase-liquid hygrometer-thermometer
1897 applicable to basalts through rhyolites. *Am. Mineral.*, 100, 2172-2184, 2015.
1898
- 1899 Webster, J. D., Kinzler, R. J., and Mathez, E. A.: Chloride and water solubility in basalt and andesite melts
1900 and implications for magmatic degassing. *Geochim. Cosmochim. Ac.*, 63(5), 729-738, 1999.
1901
- 1902 Welsch, B., Faure, F., Famin, V., Baronnet, A., and Bachèlery, P.: Dendritic crystallization: A single process
1903 for all the textures of olivine in basalts? *J. Petrol.*, 54, 539-574, 2013.
1904
- 1905 White, J. C., Parker, D. F., and Ren, M.: The origin of trachyte and pantellerite from Pantelleria, Italy:
1906 insights from major element, trace element, and thermodynamic modelling. *J. Volcanol. Geoth. Res.*,
1907 179, 33-55, 2009.
1908
- 1909 Whitney, D. L., and Evans, B. W.: Abbreviations for names of rock-forming minerals. *Am. Mineral.*, 95(1),
1910 185-187, 2010.
1911
- 1912 Wilcox, C.: *Eruptive, Magmatic and Structural Evolution of a Large Explosive Caldera Volcano: Los Humeros*
1913 *México*. PhD Thesis. University of Leicester, UK, pp. 485, 2011.
1914
- 1915 Wohletz, K., Civetta, L., and Orsi, G.: Thermal evolution of the Phlegraean magmatic system. *J. Volcanol.*
1916 *Geoth. Res.*, 91, 381-414, 1999.
1917
- 1918 Wood, B. J.: The solubility of alumina in orthopyroxene coexisting with garnet. *Contrib. Mineral. Petr.*,
1919 46(1), 1-15, 1974.
1920
- 1921 Wotzlaw, J. R.-F., Bindeman, I. N., Watts, K. E., Schmitt, A. K., Caricchi, L. and Schaltegger, U.: Linking rapid
1922 magma reservoir assembly and eruption trigger mechanisms at evolved Yellowstone type
1923 supervolcanoes. *Geology*, 42, 807–810, 2014.
1924
- 1925 Wright, T. L., and Fiske, R. S.: Origin of the differentiated and hybrid lavas of Kilauea volcano, Hawaii. *J.*
1926 *Petrol.*, 12, 1-65, 1971.
1927

- 1928 Yáñez, C., and García, S.: Exploración de la región geotérmica Los Humeros-Las Derrumbadas, Estados de
1929 Puebla y Veracruz, C.F.E. Mexico, Internal Report, 1-96, 1982.
- 1930 Yang, H. J., Kinzler, R. J., and Grove, T. L.: Experiments and models of anhydrous, basaltic olivine-
1931 plagioclase-augite saturated melts from 0.001 to 10 kbar. *Contrib. Mineral. Petr.*, 124, 1-18, 1996.
1932
- 1933 Yang, H. J., Frey, F. A., Clague, D. A., and Garcia, M. O.: Mineral chemistry of submarine lavas from Hilo
1934 Ridge, Hawaii: implications for magmatic processes within Hawaiian rift zones. *Contrib. Mineral. Petr.*,
1935 135, 355-372, 1999.
1936
- 1937 Zhang, J., Davidson, J. P., Humphreys, M. C. S., Macpherson, C. G., and Neill, I.: Magmatic enclaves and
1938 andesitic lavas from Mt. Lamington, Papua New Guinea: implications for recycling of earlier-
1939 fractionated minerals through magma recharge. *J. Petrol.*, 56, 2223-2256, 2015.
1940
- 1941 Zheng, J., Mao, J., Chai, F., and Yang, F.: Petrogenesis of Permian A-type granitoids in the Cihai iron ore
1942 district, Eastern Tianshan, NW China: Constraints on the timing of iron mineralization and implications
1943 for a non-plume tectonic setting. *Lithos*, 260, 371-383, 2016.
1944
- 1945 Zhu, Y., and Ogasawara, Y.: Clinopyroxene phenocrysts (with green salite cores) in trachybasalts:
1946 implications for two magma chambers under the Kokchetav UHP massif, North Kazakhstan. *J. Asian
1947 Earth Sci.*, 22, 517-527, 2004.
1948
1949

1950 **SUPPLEMENTARY MATERIALS**

1951 *Supplementary Tables S1: Feldspar, EMPA complete dataset.*

1952 *Supplementary Table S2: Clinopyroxene, EMPA complete dataset.*

1953 *Supplementary Table S3: Olivine, EMPA complete dataset.*

1954 *Supplementary Table S4: Orthopyroxene, EMPA complete dataset.*

1955 *Supplementary Table S5: Opaque Minerals and Spinel, EMPA complete dataset.*

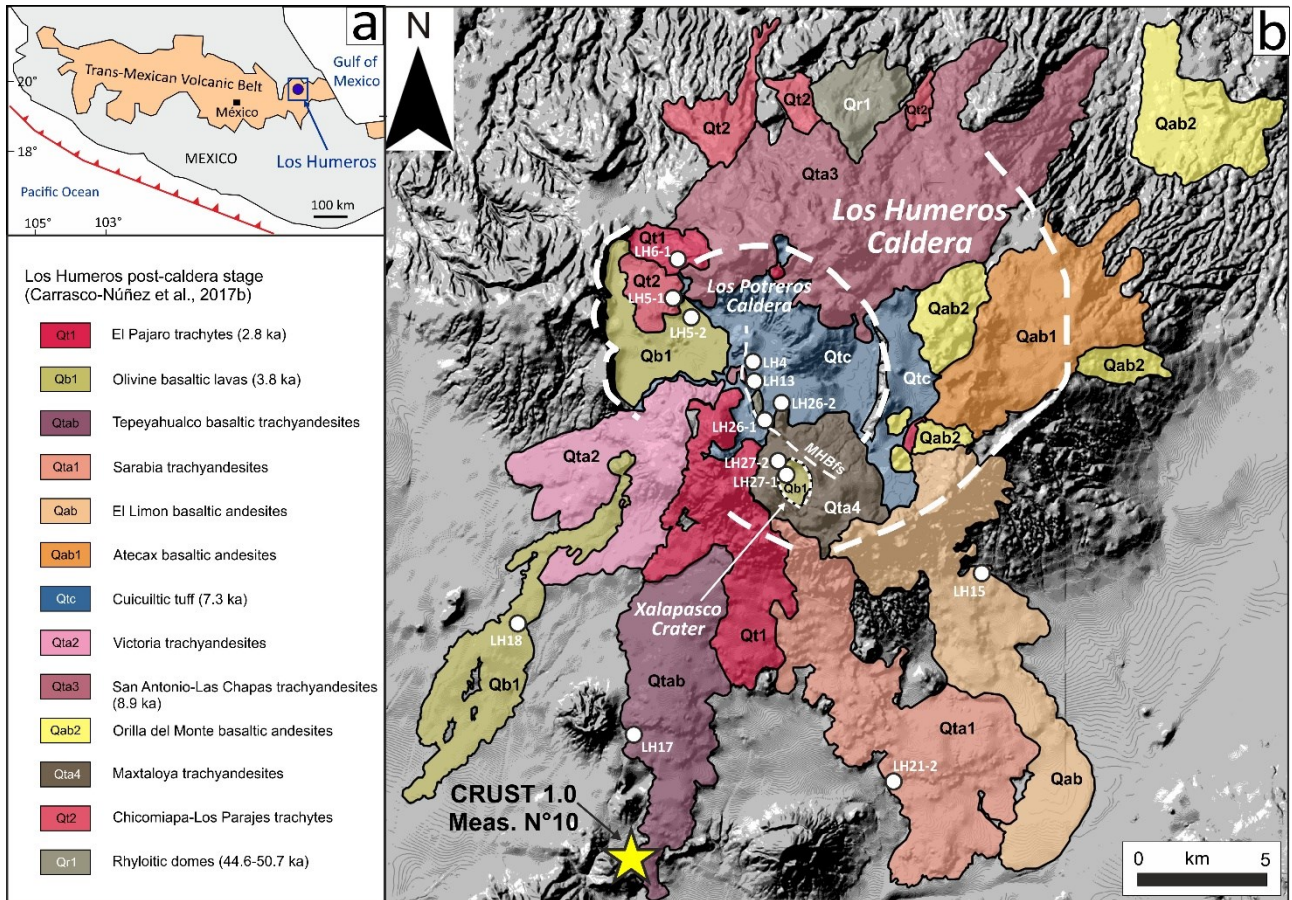
1956 *Supplementary Table S6: Major-Elements Mass-Balance Models.*

1957 *Supplementary Table S7: Repeated measurement of EMP standards*

1958

1959 FIGURES

1960 Figure 1



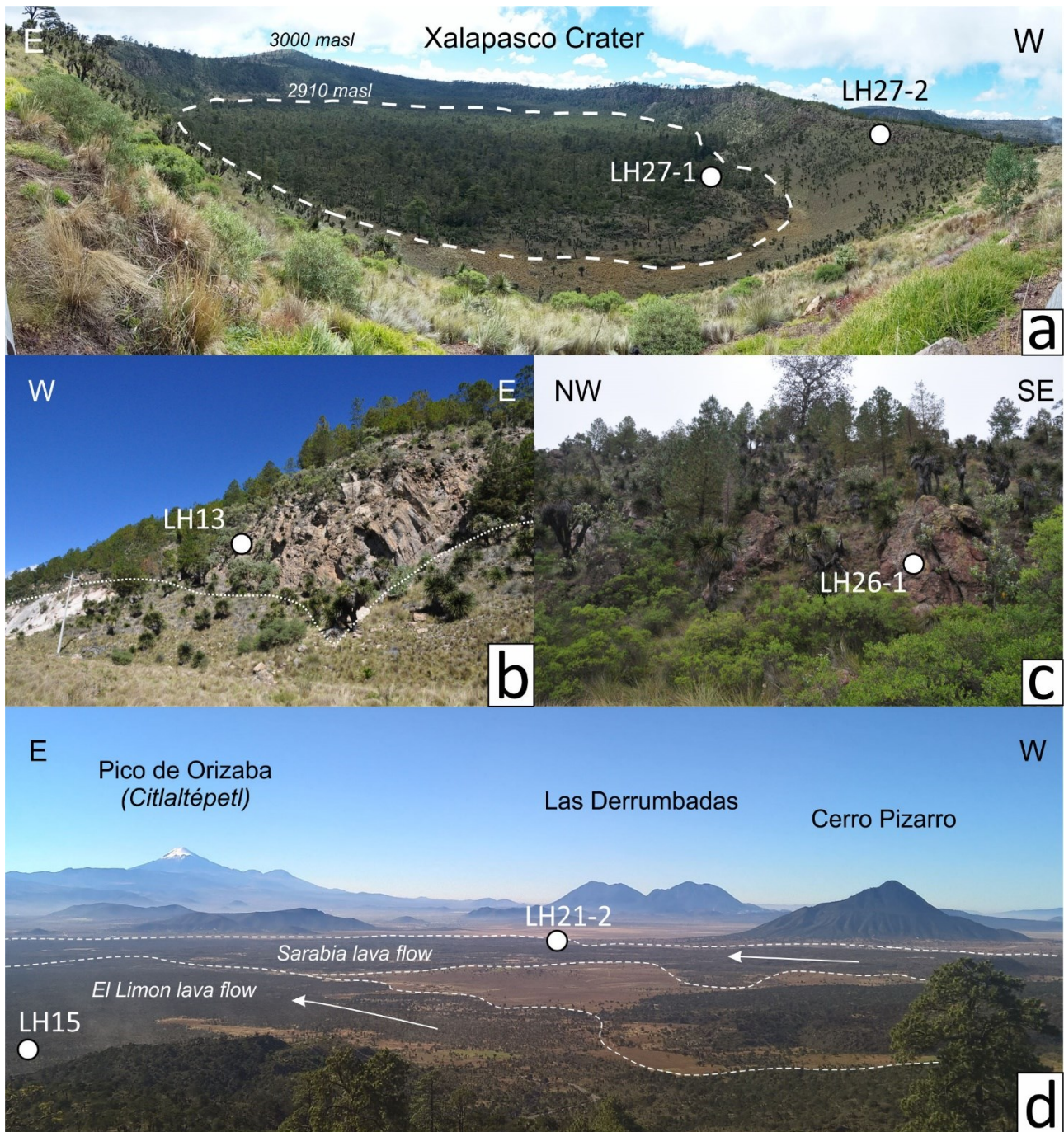
1961

1962 **Figure-1.** Geological Context. (a) The Los Humeros volcanic complex (LHVC, blue dot) with respect to the
1963 Trans-Mexican Volcanic Belt (TMVB). (b) Shaded relief image obtained from 15 m resolution digital
1964 elevation model (DEM) of the LHVC. Volcanic products of the Los Humeros post-caldera stage are redrawn
1965 from Carrasco-Núñez et al. (2017b). The description of the volcanic units, their names and abbreviations
1966 follow Carrasco et al. (2017b). The map shows location (white dots) and volcanological significance of the
1967 samples used in this study. The yellow star indicates the locality of the measure N°10 of the Crust 1.0
1968 global model (Dziewonski and Anderson, 1981; Davies, 2013).

1969

1970

Figure 2



1972

1973

1974

1975

1976

1977

1978

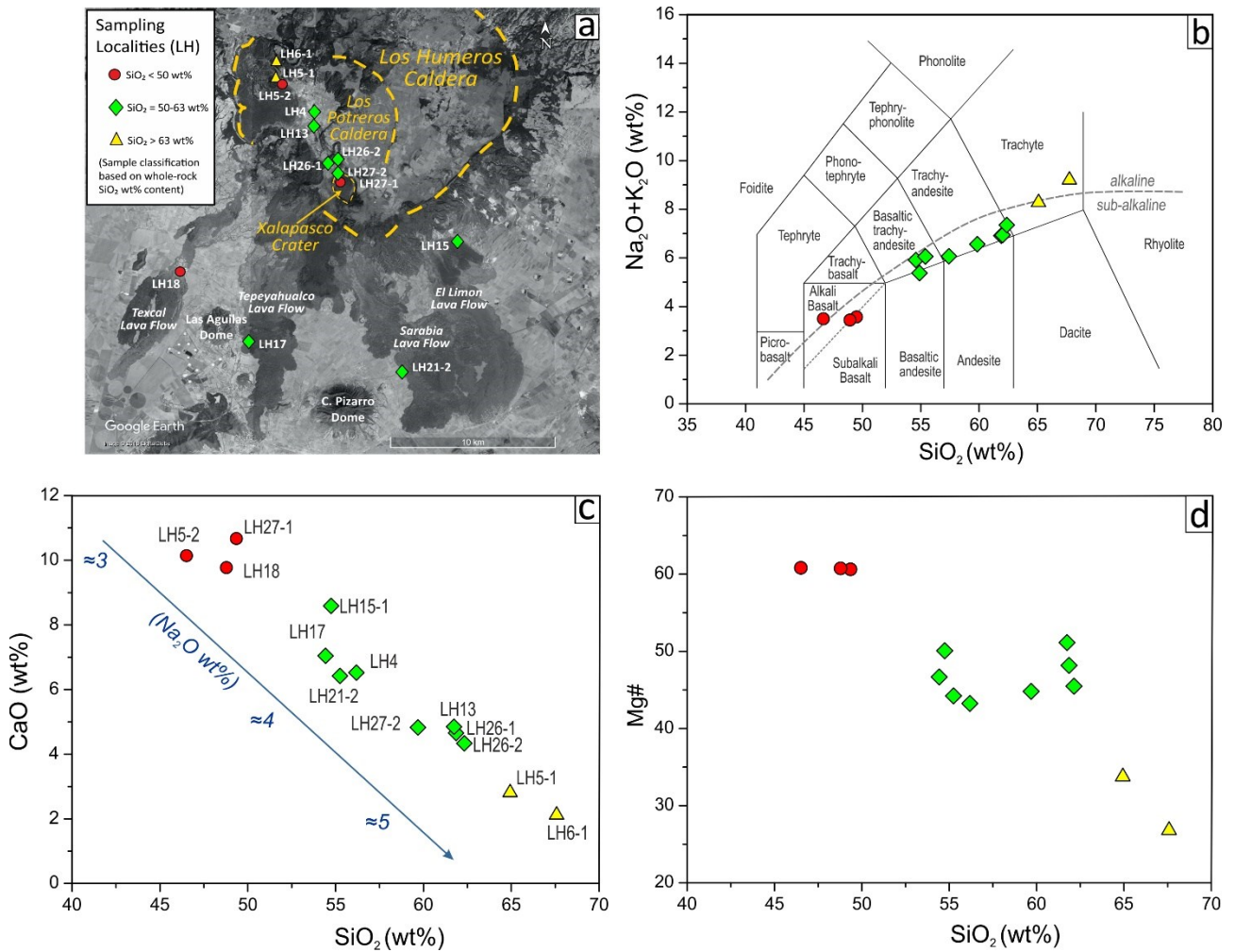
1979

1980

1981

Figure-2. Field photographs of LHPCS volcanic products. (a) E-W panoramic view of Xalapasco crater; the white dashed line indicates the limit of Cpx-bearing OI-basalts lavas filling the crater. (b) Intra-caldera trachyandesitic lavas outcropping at Los Potreros, south to Los Humeros town. (c) Trachyandesitic lava-dome outcropping inside Los Potreros caldera, north to Xalapasco crater. (d) E-W panoramic view from the SE Los Humeros caldera rim. With dashed lines are indicated the two major trachyandesitic lava flows of “El Limón” and “Sarabia”. Pico de Orizaba, Las Derrumbadas and Cerro Pizarro volcanoes are also indicated. White dots indicate sampling localities.

1982 **Figure 3**

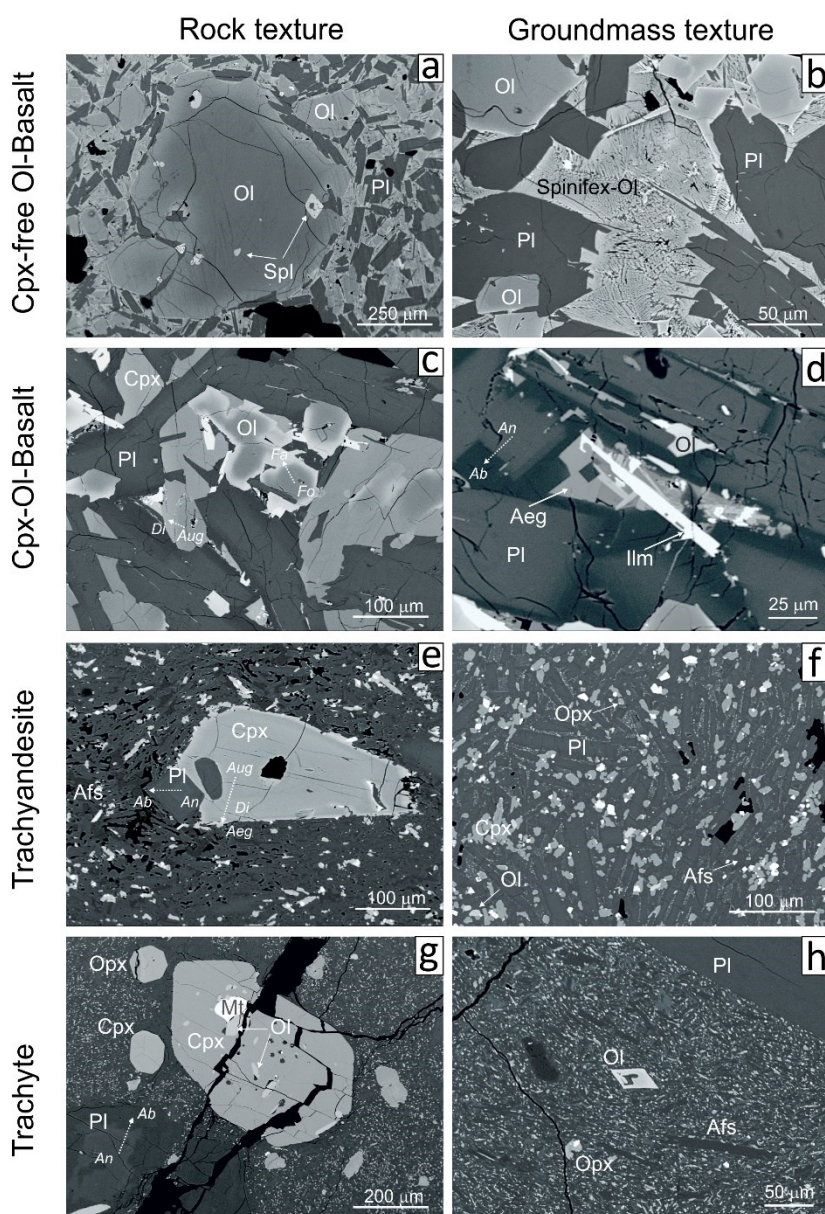


1983

1984 **Figure-3.** (a) Satellite image of the LHVC (Image Landsat from Google Earth Pro, 2018 Digital Globe;
 1985 courtesy of Google) with localization of samples selected for the application of Rayleigh Fractional
 1986 Crystallization model and for thermobarometry models. (b) Total alkali versus silica (TAS) diagram (Le
 1987 Maitre et al., 2002). (c-d) Major elements selected Harker diagrams for LHPCS studied lavas. The different
 1988 symbols (circle for basalt, diamond for trachyandesite and triangle for trachyte) represent the graphic code
 1989 that will be used coherently along the manuscript.

1990

1991



1993

1994

1995

1996

1997

1998

1999

2000

2001

2002

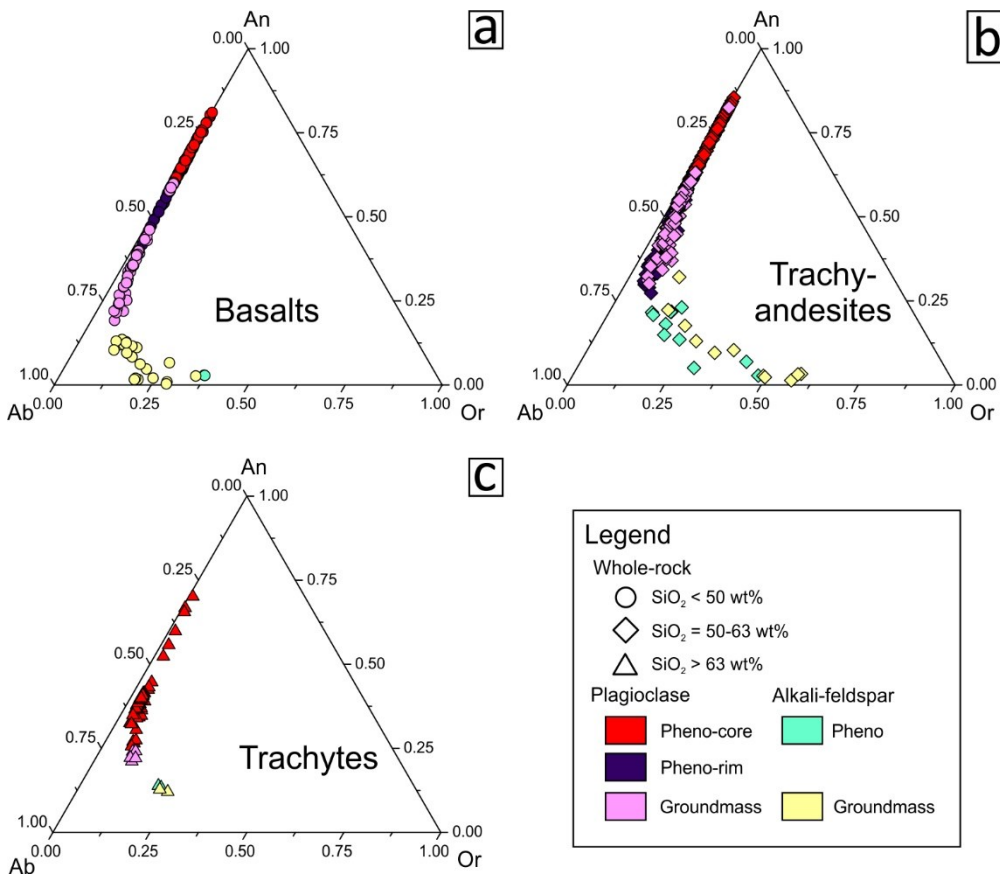
2003

2004

Figure-4. Microtextures and fabrics of the LHPCS lavas. (a) Back-scattered electrons (BSE) image of the Cpx-free Ol-basalt fabric, dominated by euhedral unzoned homogeneous Pl+Ol, with major olivine phenocryst characterized by Cr-Spl inclusions. (b) BSE image of Cpx-free Ol-basalt groundmass highlighting the spinifex to skeletal and dendritic crystallization of olivine, associated to the swallow-tailed morphology of plagioclase. (c) BSE image of Cpx-bearing Ol-basalt. Normal monotonous zoning at rim is observed for all the main mineral phases (Pl+Ol+Cpx). (d) BSE image of Cpx-bearing Ol-basalt groundmass characterized by albitic plagioclase, aegirine-pyroxene, Fe-rich olivine and ilmenite. (e-f) BSE images of trachyandesites. It is possible to observe a microcrystalline groundmass where major phenocrysts of Cpx and Pl are dispersed. (g-h) BSE images of trachytes, characterized by a microcrystalline groundmass and Pl+Cpx+Opx phenocryst. Plagioclase phenocrysts show normal monotonous to normal step zoning. Major Cpx phenocrysts present inclusion of Ol+Mt.

2005

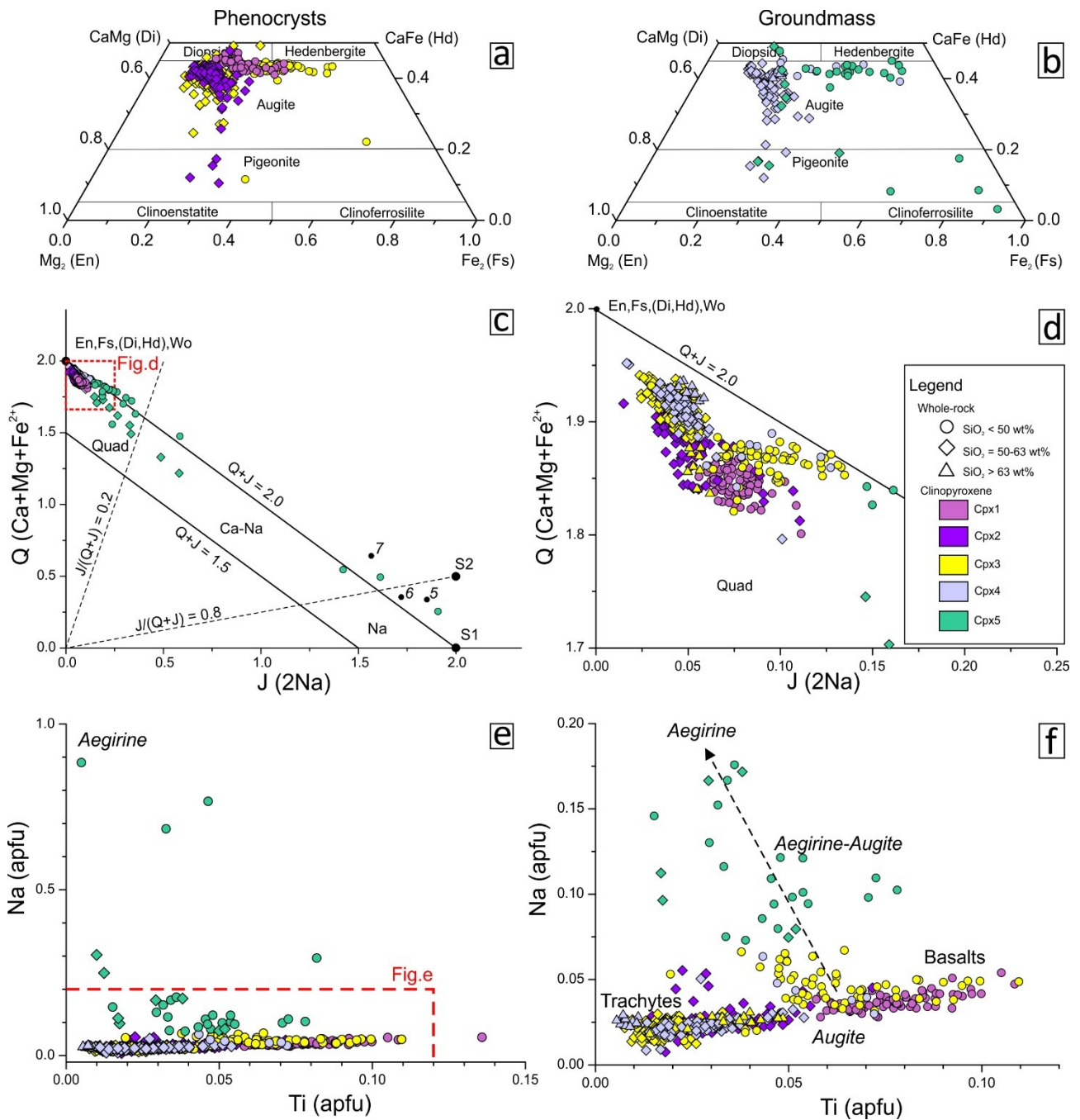
2006 **Figure 5**



2007

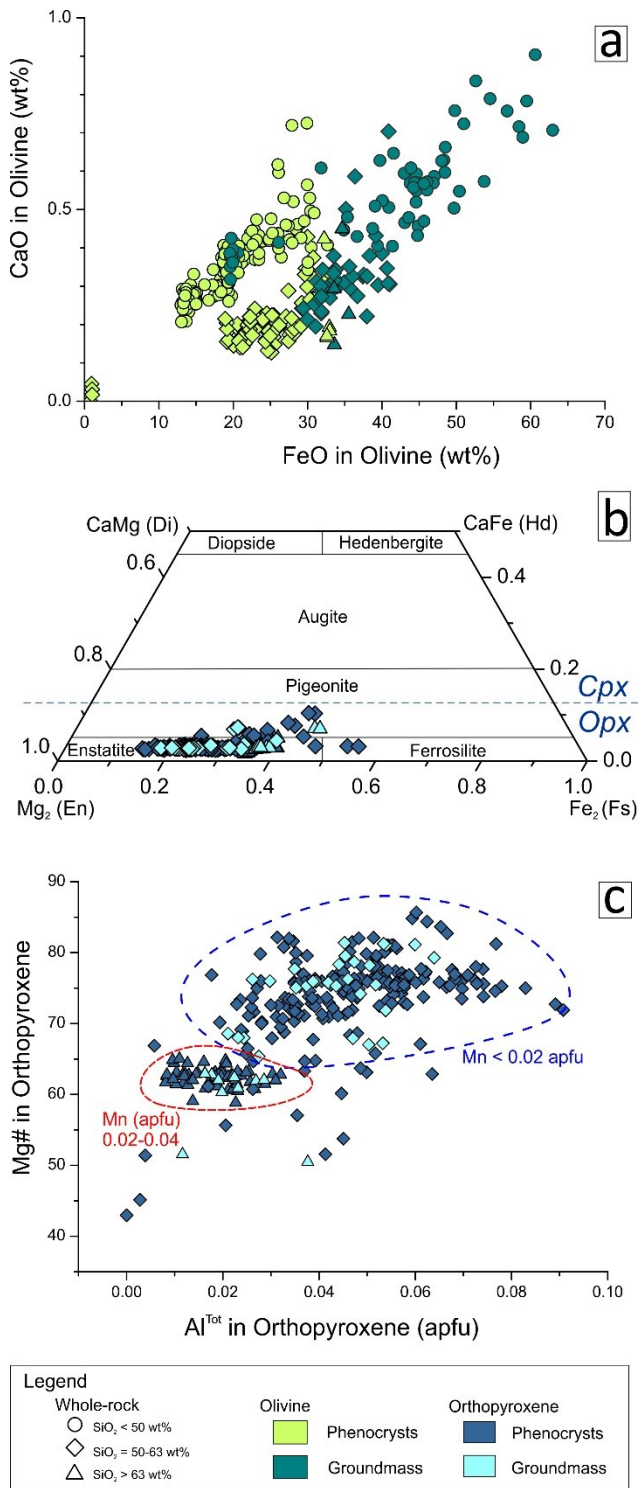
2008 **Figure-5.** An-Ab-Or diagrams showing the composition of feldspar in (a) basalts (circles), (b) trachyandesites
2009 (diamonds) and (c) trachytes (triangles) of LHPCS lavas.

2010



2012
 2013 **Figure-6.** Di-Hd-En-Fs, Q-J and Ti vs. Na diagrams showing the composition of clinopyroxenes in LHPCS
 2014 lavas. Symbol shapes follow Fig. 3. (a) Di-Hd-En-Fs diagram for clinopyroxene phenocrysts (Cpx1, Cpx2,
 2015 Cpx3). (b) Di-Hd-En-Fs diagram for clinopyroxene microlites (Cpx4) and Na-clinopyroxenes (Cpx5). (c) Q-J
 2016 diagram for pyroxenes with indication of endmembers (Morimoto, 1989). (d) Enlargement of area indicated
 2017 in (c). (e) Ti vs. Na (apfu) diagram illustrating the compositional differences between clinopyroxenes. (f)
 2018 Enlargement of area indicated in (e), showing the main Augite trend characterizing the evolution from
 2019 basalts to trachytes and the divergent trend of Aegirine-Augite and Aegirine series.

2021 **Figure 7**

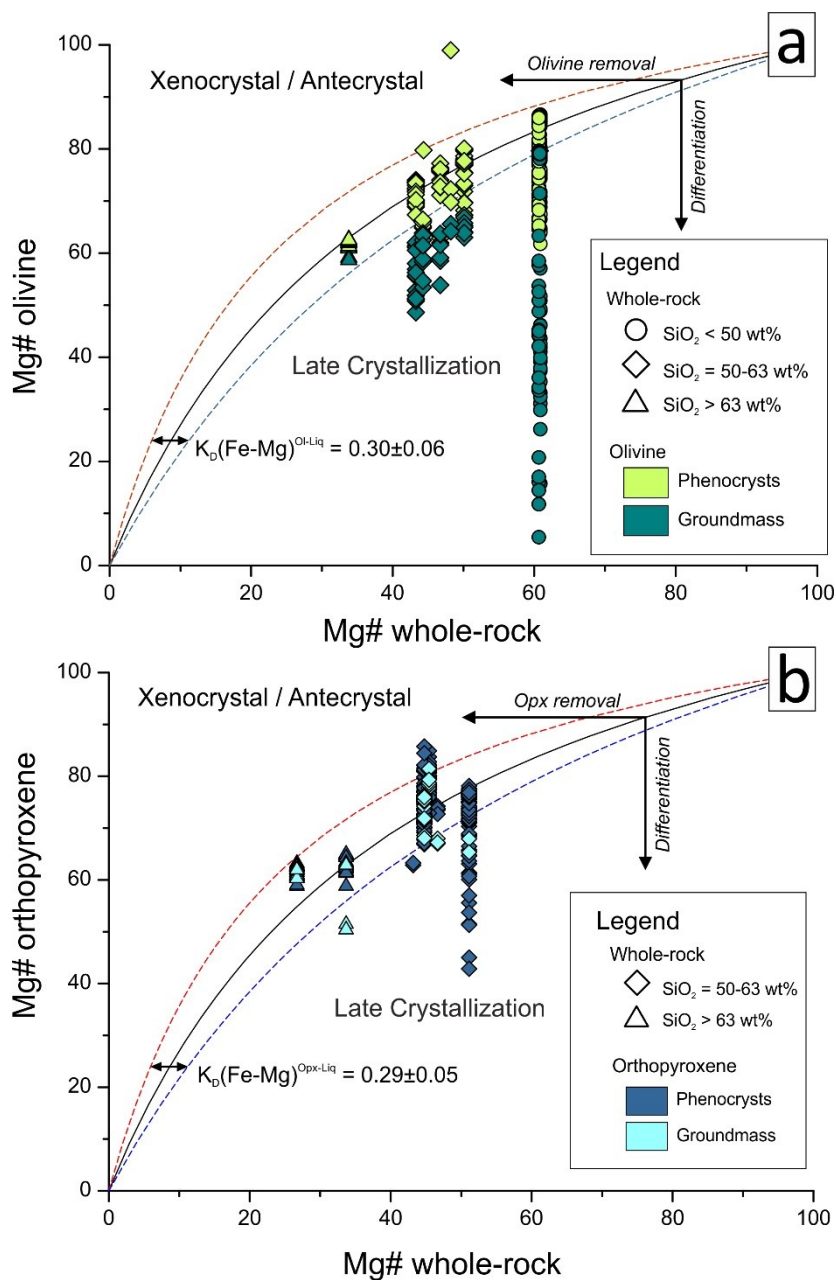


2022

2023 **Figure-7.** (a) CaO vs. FeO diagram showing the composition of olivine in LHPCS lavas. (b) Di-Hd-En-Fs
 2024 diagram showing the orthopyroxene chemistry in LHPCS studied lavas. (c) Al^{Tot} vs. Mg# diagram showing the
 2025 main compositional differences between orthopyroxene populations from trachytes and trachyandesites.
 2026 Mn (apfu) contents are also reported for the two populations.

2027

2028



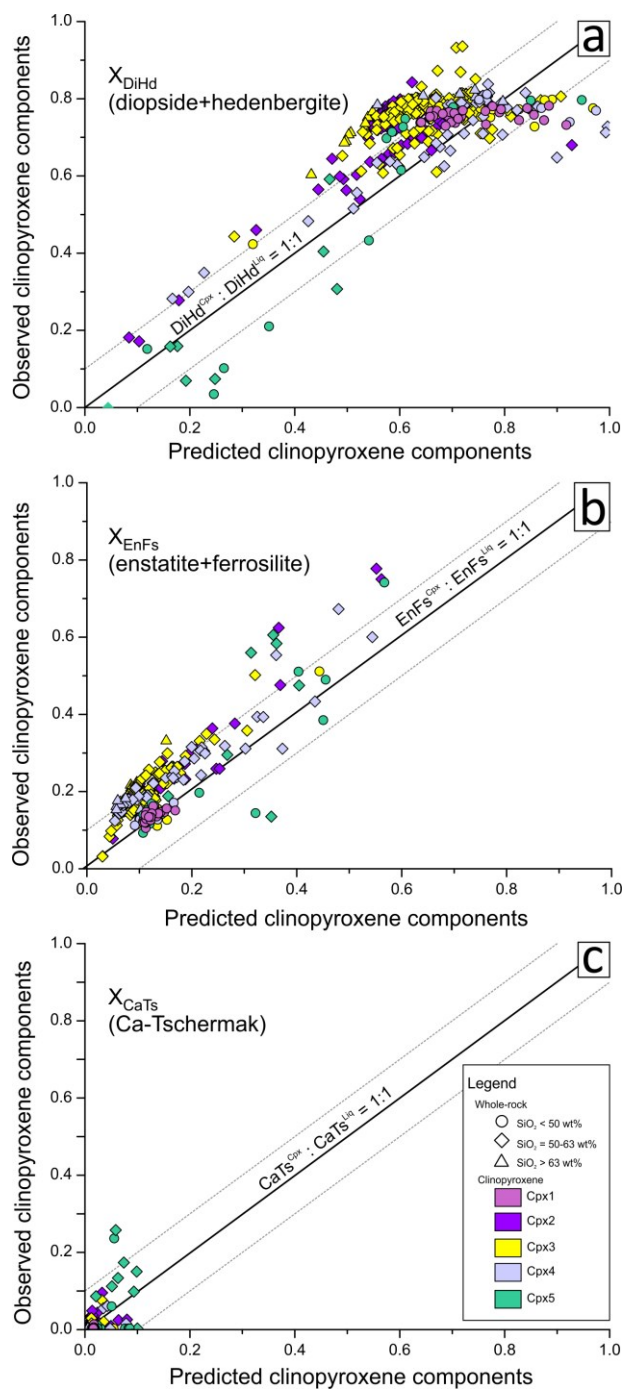
2030

2031 **Figure-8.** Rhodes diagrams showing the results of test of equilibrium liquid and olivine (a) and
 2032 orthopyroxene (b). The partitioning of Fe-Mg between mineral and liquid (Fe-Mg exchange coefficient) or
 2033 $K_D^{\text{Min-Liq}}(\text{Fe-Mg})$ is shown (black lines). The accepted range of equilibrium constant values for both figures (a)
 2034 and (b) is indicated by dashed lines. $K_D^{\text{Min-Liq}}(\text{Fe-Mg})$ values are from Putirka (2008). Nominal melt
 2035 compositions are selected from whole-rock analyses. Vectors of olivine and orthopyroxene removal from
 2036 melt and closed system differentiation are redrawn after Putirka (2008 and references therein). Fields of
 2037 “Xenocrystal/Antecrystals” and “Late Crystallization” are also indicated. Symbols and colors refer to Fig. 7.

2038

2039

2040

Figure 9

2041

2042

2043

2044

2045

2046

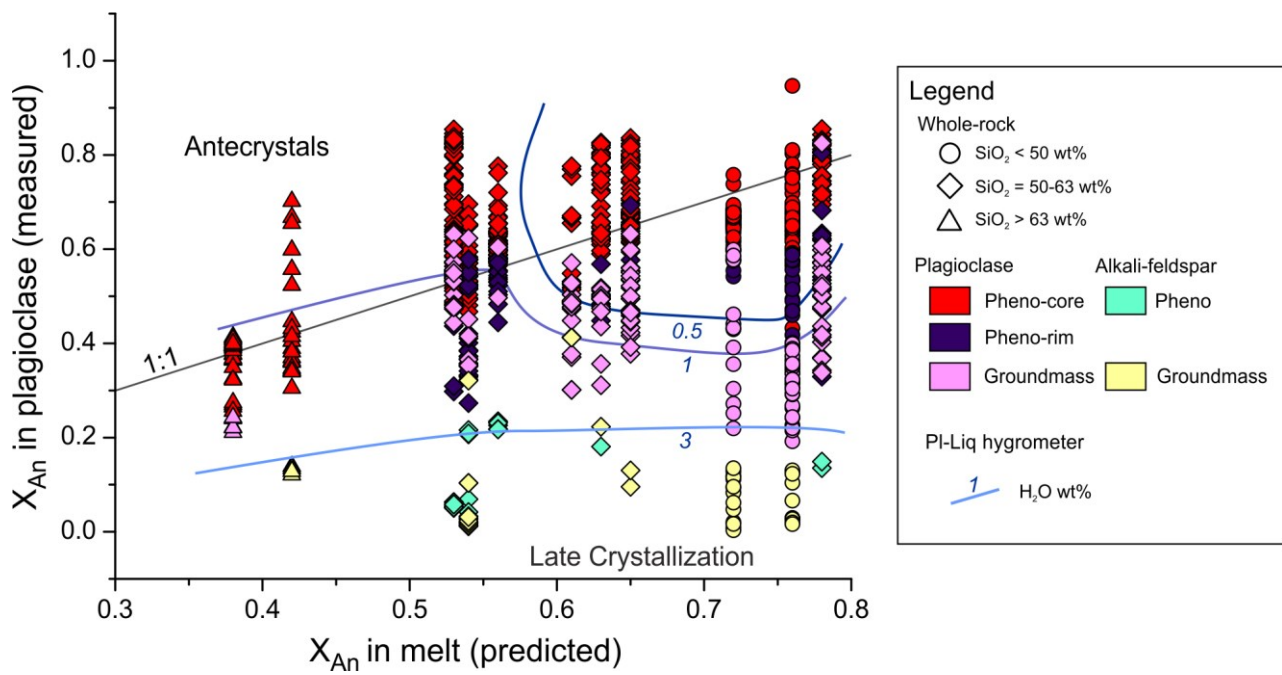
2047

2048

2049

Figures-9. Clinopyroxene-melt equilibrium tests: (a) DiHd: diopside-hedenbergite, (b) EnFs: enstatite-ferrosilite, and (c) CaTs: Ca-Tschermak components. Equilibrium associated with observed components in pyroxenes are paired with predicted components in respective hosting-melts. The accepted range of equilibrium is indicated in each figure by dashed lines. Nominal melt compositions for clinopyroxene are selected from whole-rock analyses. Symbols and colors refer to Fig. 6.

2050 **Figure 10**



2051

2052

2053 **Figure-10.** Plagioclase-melt equilibrium test. Equilibrium associated with anorthite (X_{An}) component in
2054 plagioclase are paired with predicted anorthite in melt. Nominal melt compositions for plagioclase are
2055 selected from whole-rock analyses. Calculated water concentrations using plagioclase-melt hygrometer
2056 (Putirka, 2008) are reported in diagrams with isolines (graded blue lines). Symbols and colors refer to Fig. 5.

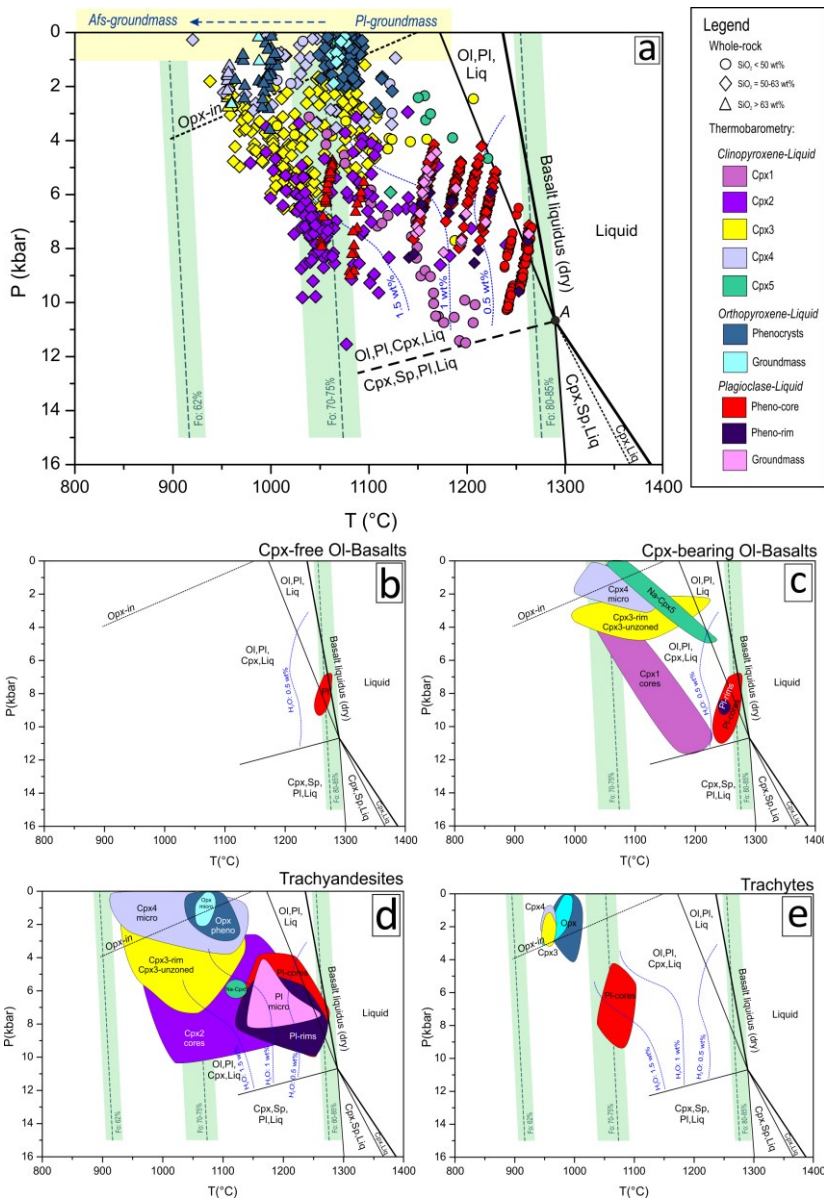
2057

2058

2059

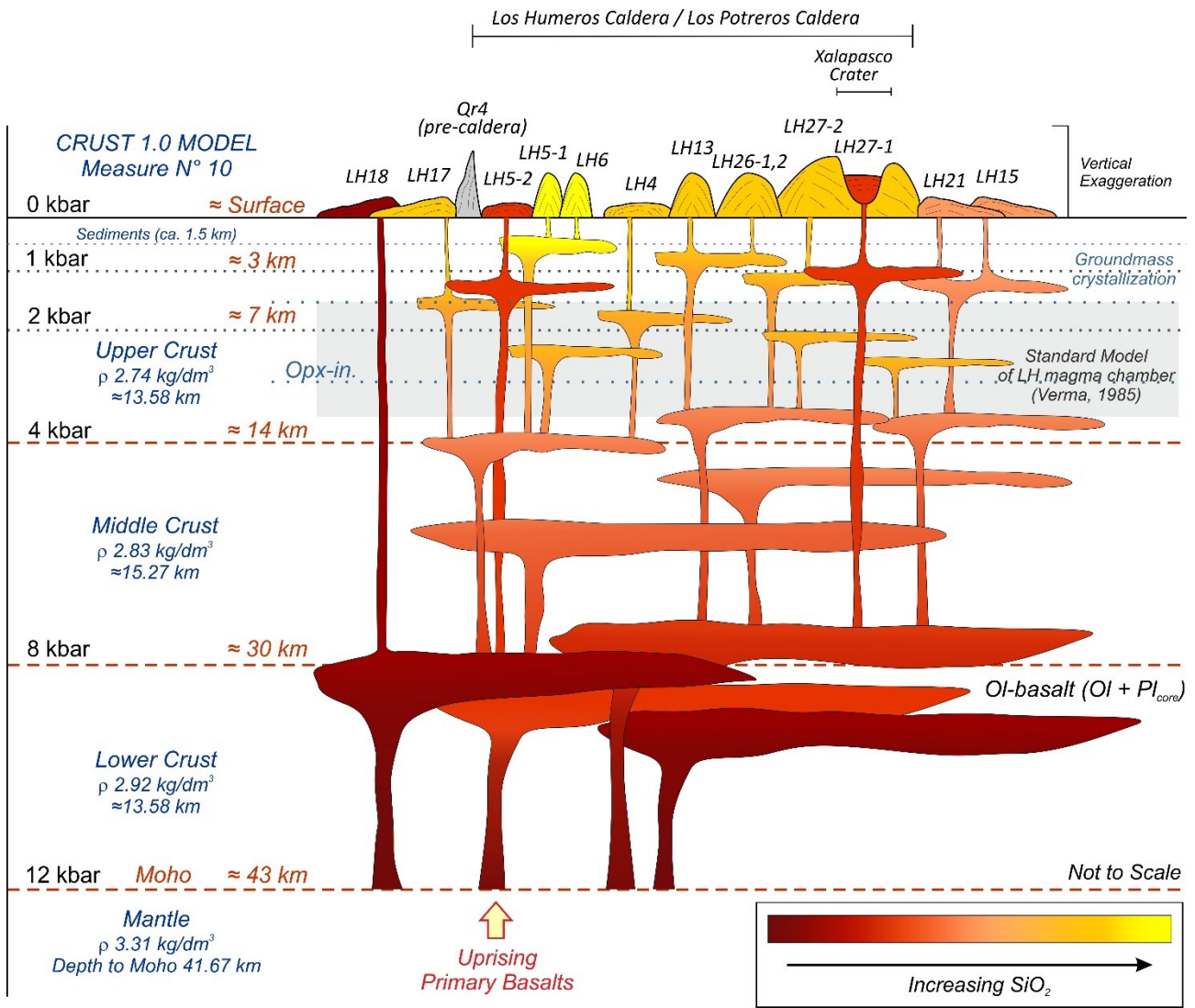
2060

2061 **Figure 11**



2062
 2063
 2064
 2065
 2066
 2067
 2068
 2069
 2070
 2071
 2072
 2073
 2074

Figure-11. Thermobarometric estimates; a) A summary of the results obtained from thermobarometry models applied to Los Humeros post-caldera stage lavas. Symbols refer to whole-rock chemistry compositions, whereas colors of different phases refer to mineral chemistry diagrams. Green-shaded field shows the results of olivine-liquid thermometry. Blue dashed isolines represent the results of plagioclase-melt hygrometer. Yellow-shaded field indicates pressure-temperature domain of crystallization of feldspars in groundmass. Basalt liquidus curve, Ol+Cpx+Pl+Sp+Liq stability fields and point “A” (basalt liquidus in equilibrium with mantle peridotite mineral assemblage of Ol+Cpx) are redrawn after Grove (2000). Opx-in stability curve is redrawn after Wallace and Anderson (2000). Schematized results are presented separately for b) Cpx-free Ol-basalt; c) Cpx-bearing Ol-basalts; d) trachyandesites; and e) trachytes.



2076

2077

2078 **Figure-12.** Schematic representation (not to scale) of the magmatic plumbing system feeding LHPCS
 2079 activity, beneath Los Humeros caldera as derived by pressure-temperature estimates obtained from
 2080 mineral-liquid thermobarometry models. The conceptual model is integrated with the crustal structure of
 2081 the study area as derived by the Measure N°10 of the Crust 1.0 global Model (Davies, 2013). Grey shaded
 2082 field indicates the depth and thickness of the existing conceptual model of a single, huge classical magma
 2083 chamber proposed by Verma (1985a, 1985b) and mainly related to the Los Humeros caldera-stage activity.

2084

2085

2086 **Table 1****Table 1 - Major element bulk-rock compositions of LHPCS studied lava samples.**

Rock type	Basalts			Trachyandesites								Trachytes	
Sample	LH5-2	LH18	LH27-1	LH17	LH15-1	LH21-2	LH4	LH27-2	LH13	LH26-1	LH26-2	LH5-1	LH6-1
SiO ₂ , wt%	46.51	48.78	49.35	54.43	54.74	55.24	56.18	59.69	61.74	61.85	62.14	64.93	67.58
TiO ₂	1.471	1.490	1.372	1.394	1.075	1.561	1.375	1.016	0.882	0.889	0.933	0.738	0.605
Al ₂ O ₃	16.23	16.17	17.11	16.33	20.68	15.99	16.57	17.39	15.68	15.70	16.82	15.47	15.83
Fe ₂ O ₃ ^{tot}	10.78	10.62	10.26	8.08	6.49	8.62	7.88	5.76	5.15	5.22	5.32	4.58	3.73
MnO	0.161	0.160	0.155	0.123	0.092	0.133	0.114	0.087	0.085	0.085	0.095	0.077	0.074
MgO	8.44	8.29	7.97	3.57	3.28	3.45	2.90	2.36	2.72	2.45	2.24	1.18	0.69
CaO	10.14	9.77	10.67	7.04	8.59	6.42	6.52	4.83	4.85	4.66	4.52	2.81	2.12
Na ₂ O	3.11	2.98	3.21	4.10	3.68	4.14	3.96	4.31	4.19	4.31	4.30	4.79	5.26
K ₂ O	0.33	0.41	0.30	1.76	1.64	1.86	1.99	2.20	2.67	2.58	2.76	3.44	3.89
P ₂ O ₅	0.19	0.21	0.17	0.32	0.26	0.34	0.34	0.27	0.25	0.23	0.22	0.18	0.13
LOI	1.90	0.81	-0.35	0.90	0.49	0.52	1.19	1.55	0.50	0.93	0.70	0.73	0.31
Total (wt%)	99.27	99.68	100.20	98.05	101.01	98.29	99.02	99.47	98.72	98.91	100.10	98.92	100.20
Mg#	61	61	61	47	50	44	43	45	51	48	45	34	27

Note: LOI - loss on ignition; Mg# - molar $[Mg \cdot 100 / (Mg + Fe^{tot})]$.

2087

2088